SPATIOTEMPORAL DYNAMICS OF GRADIENT SENSING AND POLARIZATION IN YEAST

Meng Jin

A dissertation submitted to the faculty of the University of North Carolina at Chapel Hill in partial fulfillment of the requirements for the degree of Doctorate of Philosophy in the Department of Biochemistry and Biophysics, School of Medicine.

Chapel Hill
2012

Approved by:

Timothy Elston, Ph.D.

Beverly Errede, Ph.D.

Henrik Dohlman, Ph.D.

Daniel Lew, Ph.D.

Nikolay Dokholyan, Ph.D.

Abstract

MENG JIN: Spatiotemporal dynamics of gradient sensing and polarization in yeast
(Under the direction of Dr. Timothy Elston)

Cells are able to interpret different kinds of spatial information. Characterizing the spatiotemporal dynamics in signal transduction is essential to understand how a cell process information from its environment. Here, we quantitatively studied the gradient sensing and polarization in budding yeast *Saccharomyces cerevisiae,* using mathematical modeling and time-lapse microscopy. In the gradient sensing, we found that yeast cells can dynamically remodel local pheromone gradient and achieve better gradient sensing by secreting Bar1, a protease that degrades α-factor. Altering the local environment also avoids non-productive cell-cell interactions. During the polarity establishment without spatial cues, imaging with high spatiotemporal resolution revealed oscillation in the initial clustering of polarity factors, suggesting the presence of a negative feedback loop that disperses the factors. Mathematical modeling including an additional negative feedback reproduced similar dynamics and predicted that negative feedback would confer robustness to the polarity circuit, and make the kinetics of competition between polarity clusters relatively insensitive to the concentrations of polarity factors. These predictions were confirmed experimentally. Lastly, to understand how scaffold protein processes the spatial information of pheromone, we presented preliminary results for characterizing the kinetics of pheromone induced Ste5 membrane recruitment using time-lapse fluorescent imaging and single cell tracking.

Acknowledgements

Completion of this thesis would not have been possible without the help of many people. First and foremost, I must give my gratitude to my advisor Dr. Timothy Elston. Joining his lab has been the greatest decision that I ever made. He welcomed me to join the lab regardless of my little experience in research, and showed remarkable patience to guide me. Whenever I needed to discuss with him, he always kept his office door open. He gave me the greatest freedom in my research and encouraged me for any small progress. Every time I got frustrated by my projects, his encouragement, curiosity in science and ability to approach problems from different perspectives keep me confident and my pursuing of Ph.D. a pleasant journey.

I feel especially lucky and grateful to be able to collaborate with Dr. Beverly Errede and Dr. Daniel Lew. I would not complete the work included in this thesis without their guidance and advice. They gave me valuable suggestions about how to design experiments, how to think critically and how to present results. They showed me the power and beauty of experiments, changed my understanding of doing experiments. Their great personality made the collaboration a joyful experience.

Further, I need to thank the members of my committee, Dr. Henrik Dohlman and Dr. Nikolay Dokholyan, for their informative discussions and valuable suggestions during lab meetings, committee meetings and whenever I stopped by their office.

I would like to thank everyone in the Elston lab, both past and present, for making the atmosphere so enjoyable. I am deeply indebted to Marcelo Behar. He made my first

step towards the world of computational biology much easier and inspired me to capture interesting questions. I want to thank Josh Kelley, Richard Allen, Denis Tsygankov, John Houser, Vinal Lakhani, Sai Venkatapurapu, Peiying Zuo, Wanda Strychalski, Nan Hao and Adrian Serohijos, for being great resources for scientific knowledge and lab hangouts.

Finally, I must thank greatly my parents who constantly support me with the most selfless love. I also need to thank my friends outside the lab, for making my years in graduate school an unforgettable experience.

TABLE OF CONTENTS

LIST OF TABLES ix

LIST OF FIGURES x

LIST OF ABBREVIATIONS AND SYMBOLS xii

CHAPTER 1. INTRODUCTION 1

1.1 Overview 1

1.2 Polarization and gradient sensing in budding yeast 2

1.2.1 Regulators in yeast polarization pathway 3

1.2.2 Ability to break symmetry 5

1.2.3 Polarize to the right direction 7

1.2.3.1 Polarization in response to internal cues 7

1.2.3.2 Polarization in response to pheromone 8

1.2.4 Visualizing gradient sensing in microfluidic devices 10

1.3 Theoretical modeling 11

1.3.1 Turing mechanism 11

1.3.2 Local excitation global inhibition (LEGI) model 12

1.4 Summary 15

CHAPTER 2. REGULATION OF PHEROMONE GRADIENT DURING CHEMOTROPIC GROWTH VIA PROTEASE BAR1 17

2.1 Overview 17

2.2 Same-sex avoidance 18

2.3 Improved mating efficiency by local Bar1 22

2.4 Expanding searching area 25

2.5 Amplifying pheromone gradients during elongation 28

2.6 Discussion 32

2.7 Computational Methods 34

2.7.1 Framework for chemotropic growth 34

2.7.2 Chamber simulations 36

2.7.3 Simulations with *MAT*a and *MAT*α cells 37

2.7.4 Parameter estimation 37

2.7.5 Robustness in parameter values 39

CHAPTER 3. MODELING SPATIOTEMPORAL DYNAMICS IN POLARIZATION PATHWAY DURING BUDDING 42

3.1 Overview 42

3.2 Oscillatory polarization from high-resolution imaging 44

3.3 The cause of oscillatory polarization 48

3.3.1 Cytoskeletal factors 48

3.3.2 Possible negative feedback in the pathway 51

3.4 More important properties than oscillation 53

3.4.1 Robustness 53

3.4.2 Fast competition between two polarity spots 58

3.5 Fine-tuned spatiotemporal dynamics of polarization 63

3.5.1 Possible dynamics in the parameter space 63

3.5.2 Interaction between spatial range and duration of negative feedback 66

3.6 General remarks 69

3.6.1 Negative feedback during polarity establishment 69

3.6.2 Robustness of polarity establishment..... 71

3.6.3 Competition between polarity clusters..... 73

CHAPTER 4. KINETICS OF STE5 MEMBRANE RECRUITMENT 76

4.1 Overview..... 76

4.2 Kinetics of Ste5 membrane recruitment 77

4.3 General remarks and future plans 79

CHAPTER 5. CONCLUSIONS AND FUTURE DIRECTIONS 81

APPENDIX I 86

APPENDIX II 92

REFERENCES 106

LIST OF TABLES

Table 1. Strains used in Chapter 2 86

Table 2. Mating mixtures. 90

Table 3. Parameter Values 101

LIST OF FIGURES

Figure. 1.1 The autocatalytic activation of Cdc42. 6

Figure 1.2. Polarization in response to pheromone 9

Figure 2.1. Bar1 provides a self-avoidance mechanism. 19

Figure 2.2 Measure gradient tracking in BAR1 and bar1Δ cells. 22

Figure 2.3 Relative mating efficiency for opposite and same sex mating. 24

Figure 2.4. Bar1 increases the search area of *MAT*a cells. 27

Figure 2.5. Local release of Bar1 amplifies pheromone gradients 30

Figure 2.6. Bar1 allows *MAT*a cells to find unique mating partners. 32

Figure 2.7. Robustness in parameter values 41

Figure. 3.1. Competition and merging of Bem1-GFP clusters 43

Figure. 3.2. Oscillation of Bem1p-GFP clusters before bud emergence 45

Figure. 3.3. Cdc42p and Cdc24p polarization dynamics 46

Figure. 3.4. Competition and relocation of Cdc42p and Cdc24p 47

Figure. 3.5. Actin and septin polarization are delayed relative to Bem1p 49

Figure. 3.5. Actin and septin polarization are delayed relative to Bem1p 50

Figure 3.6 Negative feedback can cause oscillatory polarization 52

Figure 3.7 Negative feedback improves robustness of the polarity model 54

Figure 3.8 Polarization is robust to overexpression of Cdc42p or Cdc24p 56

Figure 3.9 Polarization is robust to overexpression of Cdc24p-Cla4p fusion 58

Figure 3.10 Competition between clusters remains fast after overexpression 59

Figure 3.11 Negative feedback buffers the accumulation of GTP-Cdc42p 61

Figure 3.12 Negative feedback accelerates or abolishes competition 62

Figure 3.12. Spatiotemporal dynamics in different parts of model parameter space 64

Figure 3.13 Relocation is regulated by the negative feedback 67

Figure 3.14 Positive and negative feedback control the relocation of clustering. 68

Figure. 4.1 Time lapse imaging of Ste5-$(GFP)_3$ in 75 nM uniform pheromone..... 78

Figure. 4.2 Quantify the kinetics of Ste5 membrane recruitment..... 79

Figure S1. Models with and without negative feedback..... 92

Figure S2. Robustness does not depend on specific rate parameters..... 100

Figure S3. Competition and equalization between clusters in Model (3)..... 104

LIST OF ABBREVIATIONS AND SYMBOLS

CRIB	Cdc42/rac interactive binding
DIC	Differential interference contrast
FH	Formin homology
GAP	GTPase-activating protein
GDI	Guanosine nucleotide dissociation inhibitor
GDP	Guanosine diphosphate
GEF	Guanine exchange factor
GPCR	G-protein coupled receptor
GTP	Guanosine triphosphate
HU	hydroxyurea
LatA	Latrunculin A
LEGI	Local excitation global inhibition
MAPK	Mitogen-activated protein kinase
PAK	p21-activated kinases
PRE	Pheromone-responsive element
PtdIns(4,5)P2	Phosphatidylinositol 4,5-bisphosphate

CHAPTER 1.

Introduction

1.1 Overview

To survive and thrive in a changing environment, cells must respond correctly to intra- and extra-cellular stimuli. The information of stimuli transmits through multiple layers of signaling proteins, activates corresponding effectors and causes correct responses. Yet, cells are neither well-stirred test tubes nor live in well-stirred solutions. Internal and external stimuli sometimes encode spatial information, such as a specific position on membrane or the distance from nutrients. In these cases, steps in signal transduction must occur at the right place with coordinated spatiotemporal dynamics to transmit the spatial information. The knowledge of general mechanisms or network motifs that regulate a spatiotemporal behavior and the reasons for choosing a specific regulatory mechanism will deepen our understanding of the design principle of biological systems.

In single cells, one process that requires well-organized spatiotemporal dynamics is chemotaxis. During chemotaxis, cells need to interpret the spatial position of input signals and then polarize to move or grow towards the right direction. We use budding yeast *Saccharomyces cerevisiae* as the model system to understand the regulation of

spatiotemporal signaling in polarization and gradient sensing. In this chapter, we introduce the biological background of polarization and gradient sensing in yeast cells and current understanding of design principles of chemotaxis pathways through theoretical modeling.

1.2 Polarization and gradient sensing in budding yeast

Yeast cells exist in diploid and haploid forms. Both diploid and haploid yeast can proliferate through budding. Haploid yeast has two mating types, **a-** and α-. Both mating types secrete a mating-type specific pheromone to attract cells of the opposite mating type. When haploid **a-** and α- cells are mixed, the diffusive pheromone from α -cells would generate a gradient attracting **a**-cells to change their morphology and grow towards the α mating partners. This process is referred as chemotropic growth. When two haploids of opposite mating type are close, they change their morphology to mate and form an **a/**α diploid cell.

Polarization and gradient sensing are key processes in the life of yeast cells. No matter what specific growth yeast cells choose, budding, chemotropic or mating, polarization regulates the morphological change. Cells need to polarize to transport proteins to daughter cells during budding, determine the growth direction during chemotropic growth and prepare cell fusion during mating. Since yeast cells are immobile and their growth is slow, a good sense of the direction of pheromone gradient is important for finding possible mating partners.

1.2.1 Regulators in yeast polarization pathway

The master regulator in yeast polarization is a Rho-family GTPase Cdc42, which regulates the polarization of actin cytoskeleton (Adams et al., 1990; Sloat et al., 1981; Zheng et al., 1994). Cdc42 is active in guanosine triphosphate (GTP) bound state and inactive in guanosine diphosphate GDP bound state. During polarization, GTP bound Cdc42 accumulates in the "front" of a cell and interacts with effectors, leading the actin polymerization. Inactive GDP-Cdc42 forms a complex with guanosine nucleotide dissociation inhibitors (GDI) in the cytoplasm. GDI prevents the GDP dissociation and keeps Cdc42 in its inactive state (Koch et al., 1997; Park and Bi, 2007). When Cdc42 binds to cell membrane, the hydrophobic geranyl-geranyl group at C-terminal is released from hydrophobic pocket in GDI, thereby dissociating from GDI at the same time (Masuda et al., 1994). In the same way, GDI can extract GDP-bound Cdc42 from membrane to cytoplasm (Masuda et al., 1994). Cdc24, a guanine exchange factor (GEF) for Cdc42, activates Cdc42 by replacing GDP with GTP (Sloat et al., 1981; Zheng et al., 1994). In polarized cells, Cdc24 binds to cell membrane by forming complex with a scaffold protein Bem1 (Ito et al., 2001; Park and Bi, 2007). Before polarization, Cdc24 stays in nucleus and cytoplasm (Shimada et al., 2000). GTP-Cdc42 is deactivated when the GTPase-activating proteins (GAPs), Bem2, Bem3, Rga1, Rga2 and Rgd2 hydrolyze GTP back to GDP (Park and Bi, 2007).

Polarity establishment requires multiple effectors of GTP-Cdc42. Two p21-activated kinases (PAKs), Ste20 and Cla4, are involved in organizing actin and septin skeletons (Park and Bi, 2007). PAKs specifically bind with GTP-Cdc42 via Cdc42/Rac Interactive Binding (CRIB) domain and localize at the leading edge with GTP-Cdc42.

Scaffold protein Bem1 is required for polarity establishment, as bem1 cells are deficient in polarization, with large, round shapes (Bender and Pringle, 1991). It brings GTP-Cdc42, Cdc24 and PAKs close in space, enhance the local activation of Cdc42 (Ito et al., 2001; Kozubowski et al., 2008; Winters and Pryciak, 2005). Polarized GTP-Cdc42 triggers the polymerization of actin filaments by its interaction with formin Bni1 (Park and Bi, 2007; Pruyne and Bretscher, 2000a). Bni1 has both CRIB domain that binds with GTP-Cdc42 and a formin homology 2 (FH2) domain, which helps to nucleate actin polymerization (Evangelista et al., 2002). Yet, how GTP-Cdc42 binding regulates Bni1 activity is still unclear. A group of polarity determining proteins named as polarisome, Spa2, Pea2 and Bud6 are found to help Bni1 function (Moseley and Goode, 2006).

Two cytoskeletons, actin and septin, are regulated by Cdc42 (Park and Bi, 2007; Pruyne and Bretscher, 2000b). Polarized Cdc42 and its effectors serve as nucleation and anchor sites for actin and septin cytoskeletons. Two actin structures, patches and cables, are involved in bud growth and morphological change in pheromone. Actin patches are made of short and branched actin filaments, mainly involved in endocytosis (Kaksonen et al., 2003). Actin cables are formed by bundles of actin filaments, providing tracks to transport material for cell wall reconstruction and bud growth. Cargos trafficking along actin cables include secretory vesicles, protein-mRNA complexs and vacuolar membranes (Park and Bi, 2007; Pruyne and Bretscher, 2000b). Two type V myosins, Myo2p and Myo4p deliver these cargos towards polarized Cdc42 (Irazoqui and Lew, 2004; Segal and Bloom, 2001). Septins are a family of GTP-binding, filament-forming protein (Park and Bi, 2007), recruited at the sites of polarized Cdc42 and then transformed into a ring structure (Kim et al., 1991). Septins tether and restrict cytokinetic

components at the mother-bud neck, strength the cell way at the division site and probably stop lateral diffusion on membrane between mother and daughter cells (Gladfelter et al., 2001). Without polarized Cdc42, cytoskeleton is randomly organized in the cytoplasm, and cells become large and round due to isotropical growth (Ayscough et al., 1997).

1.2.2 Ability to break symmetry

In most cases, cell polarity is initiated by specific spatial cues, such as active receptors or budding markers. However, yeast cells can spontaneously polarize in a random direction without any spatial cues from either budding signaling (Bender, 1993; Bender and Pringle, 1989a; Chant and Herskowitz, 1991a; Park et al., 1993) or pheromone gradient (Madden and Snyder, 1992). This spontaneous "Symmetry-break" requires an autocatalytic activation of Cdc42 triggered by random fluctuation. Scaffold protein Bem1 has been identified as a crucial factor in the autocatalytic activation by connecting GEF and p21-activated kinases (PAK) together (Kozubowski et al., 2008). Kozubowski et. al. proposed a mechanism to explain how this autocatalytic loop leads to the polarization of active Cdc42 (Kozubowski et al., 2008). In that mechanism, Bem1 provides a link between GEF and PAKs so that randomly activated GTP-Cdc42 molecules can contact closely with GEF by forming a complex with PAK-Bem1-GEF through the PAK binding domain. GEF in the complex then activates of more nearby GDP-Cdc42 molecules, which recruit more Bem1-GEF molecules and thus lead to the accumulation of GTP-Cdc42 in a constrained area close to the initial seeding GTP-Cdc42 molecule (Kozubowski et al., 2008) (Fig. 1.1). Although actin cables can transport

polarity proteins that reinforce polarization, it is less critical for symmetry breaking, since cells establish polarity normally even without actin cables (Ayscough et al., 1997; Irazoqui et al., 2003).

Besides the autocatalytic loop, there are two important properties in the pathway that ensure the local activation of GDP-Cdc42. One is that the diffusion on the cell membrane is much slower than that in mammalian cells (Valdez-Taubas and Pelham, 2003), limiting the diffusion of localized GTP-Cdc42 and Bem1-GEF complex. The other is that fewer freely diffusing Bem1-GEF molecules left in cytoplasm or membrane as the polarity patch recruits more Bem1-GEF and GTP-Cdc42 (Goryachev and Pokhilko, 2008). The depletion of non-complexed Bem1-GEF prevents the accumulation of GTP-Cdc42 everywhere.

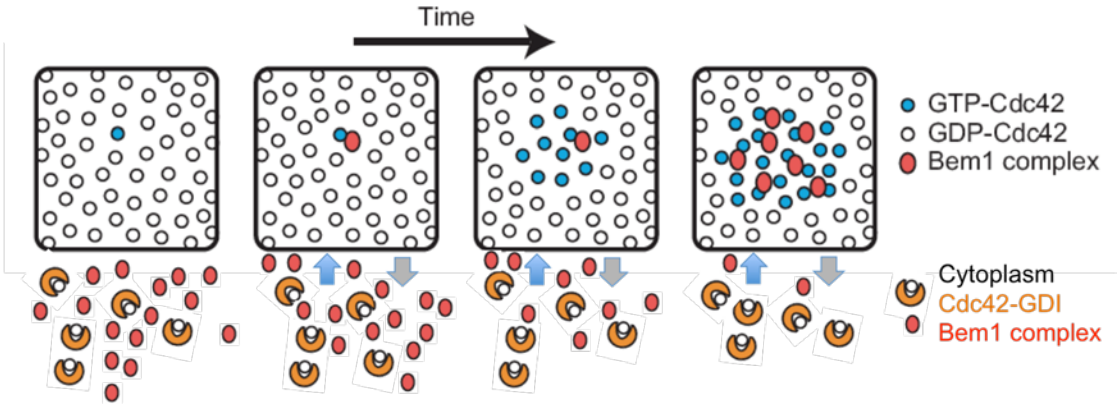

Figure. 1.1 The autocatalytic activation of Cdc42. Figure adapted from (Johnson et al., 2011)

1.2.3 Polarize to the right direction

1.2.3.1 Polarization in response to internal cues

When there is no external stimulus, yeast cells follow cell cycle and polarize at pre-determined positions to produce buds. Haploid cells bud following an axial pattern that both mother and daughter cells bud close to their previous budding site (Chant and Pringle, 1995; Park and Bi, 2007). However, diploid cells bud in a different way. Mother diploid cells bud either close or opposite to their daughter cells, but daughter cells always bud away from their mother (Chant and Pringle, 1995; Park and Bi, 2007).

The specific position for budding is marked by landmark proteins. In haploid cells, the central landmark protein is Axl2, which localizes at the mother-bud neck and remains at the division site after cytokinesis (Roemer et al., 1996). Diploid cells use several landmark proteins, Bud8, Bud9, Rax1 and Rax2, to select budding site. Bud8p and Bud9 localizes at the distal pole and the proximal pole of daughter cells, respectively (Harkins et al., 2001; Kang et al., 2004). Rax1p and Rax2p localize to both poles of both mother and daughter cell, and they are persistent markers through multiple cell divisions (Kang et al., 2004).

How is polarization biased to these landmark proteins during budding? The Ras-like GTPase Rsr1 tells the polarity machinery the position of budding markers (Bender and Pringle, 1989a; Chant and Herskowitz, 1991a). Rsr1 is activated by its GEF, Bud5 (Bender, 1993; Chant and Herskowitz, 1991a) and inactivated by its GAP, Bud2 (Bender, 1993; Park et al., 1993). The GEF of Rsr1 localizes to budding sites through interactions with the landmark proteins, resulting in a local accumulation of GTP-Rsr1 (Kang et al., 2001). GTP-Rsr1 then specifically interacts with Cdc24 and recruits more Cdc24

molecules locally(Park et al., 1997). Finally clusters of Cdc24 trigger the positive feedback of Cdc42 activation, polarized cytoskeleton and bud emergence at the site marked by the landmarks.

1.2.3.2 Polarization in response to pheromone

When there are enough pheromone molecules from cells of the opposite mating type, haploid yeast cells redirect their polarization and grow towards the source of pheromone (Segall, 1993). Polarized cytoskeletons lead to change in morphology. At intermediate pheromone levels, cells elongate forming tube-like shapes; at high pheromone concentrations, cells form a pear-shaped mating projection named shmoo (Fig 1.2A).

The spatial information of pheromone is transmitted to the polarity machinery through G-protein coupled receptors (GPCRs) and heterotrimer G proteins (Gαβγ). Upon pheromone binding, the receptors (α factor receptor Ste2 in **a**-cells and **a** factor receptor Ste3 in α cells) catalyze the GDP to GTP exchange of the Gα subunit (Gpa1), releasing Gβγ (Ste4/Ste18) subunits from GTP-Gα (Dohlman and Thorner, 2001). When GTP bound Gα is hydrolyzed to GDP bound form, GDP-Gα rebinds to Gβγ and switches the pheromone signal off (Dohlman and Thorner, 2001).

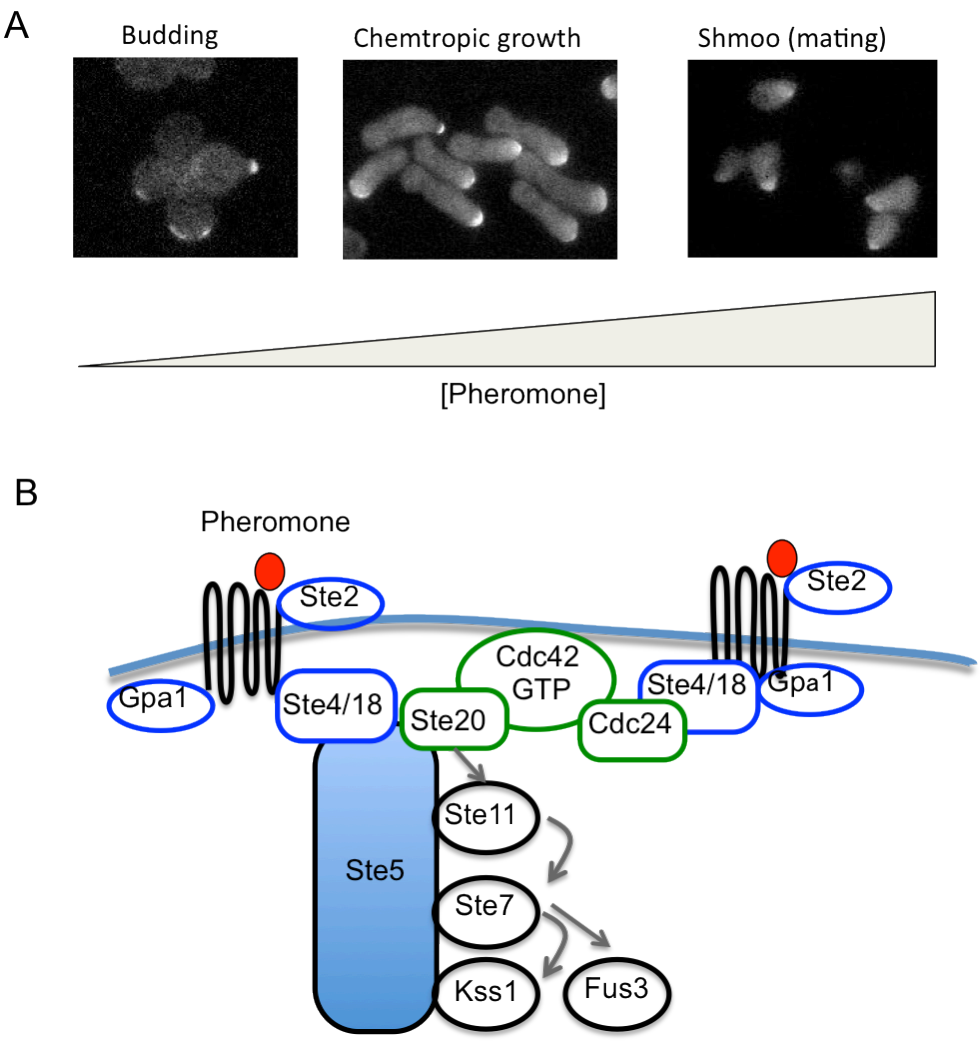

Figure 1.2. Polarization in response to pheromone.
A) Yeast cells show distinct responses to different doses of pheromone. B). A simplified schematic representation of signal transduction from pheromone to downstream effectors. See text and (Dohlman and Thorner, 2001; Park and Bi, 2007) for details.

Free Gβγ activates two branches of signaling in response to pheromone (Fig. 1.2B). The first branch is polarization. Free Gβγ recruits Cdc24, the GEF of Cdc42, to its vicinity through binding to the adaptor protein Far1 (Butty et al., 1998; Nern and Arkowitz, 1999). Cdc24 then activates Cdc42 and initiates polarization at the site with high concentration of free Gβγ, or liganded receptors.

The other branch activated by Gβγ in response to pheromone is the mitogen-activated protein kinase (MAPK) pathway. The MAPK kinase kinase Ste11 is activated by Ste20, the PAK in polarization pathway (Drogen et al., 2000). The active Ste11 phosphorylates MAPK Ste7, which further phosphorylates and activates MAPK Fus3 and Kss1 (Errede et al., 1993; Gartner et al., 1992; Neiman and Herskowitz, 1994). The Scaffold Ste5 is recruited to cell membrane by Gβγ (Pryciak and Huntress, 1998). It brings Ste11, Ste7 and Fus3/Kss1 together, improving the signaling efficiency and fine-tuning the dynamics of the activity of kinases (Good et al., 2009; Hao et al., 2008). Active Fus3 releases the inhibition of the transcriptional factor Ste12 so that Ste12 can activate a specific set of genes under the promoters containing the pheromone-responsive element (PRE) (Cook et al., 1996; Elion et al., 1993; Kronstad et al., 1987). MAPK signaling stops cell cycle and releases Far1 and Cdc24 from nucleus as a complex so that they can bind to Gβγ and anchor the polarization.

1.2.4 Visualizing gradient sensing in microfluidic devices

Advances in microfluidic devices and live cell microscopy facilitate the way we study the polarization and gradient sensing, by providing well-controlled microenvironments around cells and visualizing individual proteins at high spatial and temporal resolution. Before the advent of microfluidic devices, chemotaxis assays usually immersing a chemattractant-filled pipet in a cell suspension and allowing cells to sense and respond to the radical chemical gradient from the pipet tip (Segall, 1993). However, these techniques could not provide accurate measurement of chemoattractant gradients and thus quantitative and rigorous characterization of spatial dynamics of polarity proteins. Carefully designed microfluidic chips overcome these limits. Microfluidic chips

can repeatedly mix separate inputs through a network of channel to create spatial gradients of extracellular chemical concentrations (Dertinger et al., 2001; Jeon et al., 2000). For non-adhesive cells, spatial gradients are established by passive diffusion, preventing perturbation from active flow. These microfluidic chips can also create temporally changing environment, such as switching the direction of spatial gradients.

1.3 Theoretical modeling

How do current protein-protein interactions enable cells to polarize and track gradients? Why do polarization and gradient pathways form their current network structure? Theoretical modeling has been applied in the field to answer these questions.

1.3.1 Turing mechanism

Alan Turing proposed the first model to explain pattern formation out of homogenous protein distribution (Turing, 1952). In his model, cells produce two freely diffusing “morphogens” that control their own production and degradation. One morphogen diffuses slowly and enhances the production of both morphogens, and the second diffuses more quickly and is inhibitory (Turing, 1952). The trick of spontaneous symmetry breaking is inhomogeneous diffusion, which makes the system unstable to small spatial perturbations.

Gierer and Meinhardt generalized the original Turing model to a network motif that combines short-range positive feedback with long-range negative feedback (Gierer and Meinhardt, 1972; Meinhardt and Gierer, 1974). The local positive feedback is sufficient to amplify spatial fluctuations or shallow gradients of chemoattractants to a steep gradient of activated polarity factors inside the cell. Global inhibition blocks the

activation of polarity factors in the other area in the cell. There are two basic principles for global inhibition: depleting the substrate of the positive feedback or inducing an inhibitor of the positive feedback.

In yeast polarization pathway, autocatalytic activation of membrane GTP-Cdc42, slow-diffusing membrane proteins and depletion of Bem1-GEF build a basic activator-substrate-depletion model for polarity establishment (Goryachev and Pokhilko, 2008). Different from this Turing mechanism, Altschuler et al. demonstrated that the positive feedback alone and molecular fluctuations without global inhibition are sufficient to generate spontaneous cell polarization (Altschuler et al., 2008). However, this mechanism is sensitive to the abundance of polarity proteins and inactivation rate of GTP-Cdc42. Overexpressing Cdc42 or reducing the GTP-Cdc42 hydrolysis rate would make the model deficient in polarization.

1.3.2 Local excitation global inhibition (LEGI) model

Similar to yeast cells, social amoeba *Dictyostelium discoideum* can polarize either randomly in uniform stimulus or in the direction of shallow gradients of chemoattractant (1-2% difference in concentration between the front and rear of the cell) (Iglesias and Devreotes, 2008). Moreover, they show both sensitivity to changing gradients and adaptation in spatially unchanged stimuli: the steady-state response depends on the ratio between the local and global receptor signals (Janetopoulos et al., 2004). Studies of *Dictyostelium* chemotaxis revealed several network structures that account for the polarization and gradient tracking.

A series models with “local excitation global inhibition” (LEGI) module have been applied to explain the adaptive gradient sensing in *Dictyostelium* cells (Jilkine and Edelstein-Keshet, 2011; Kutscher et al., 2004; Levchenko and Iglesias, 2002). The central structure of LEGI model is an incoherent feedforward loop, which can achieve perfect adaptation (Behar et al., 2007; Ma et al., 2009; Takeda et al., 2012). The signal from receptor directly activates two counteracting processes: a fast-acting local activator and a slow global inhibitor. Both of them regulate the downstream effectors. Since the response of effectors depends on the ratio of activator to inhibitor but not their absolute levels, this network structure is capable of perfect adaptation to uniform stimulation, high sensitivity to gradient change and is robust to changes in parameters (Levchenko and Iglesias, 2002).

However, the LEGI mechanism itself cannot provide strong amplification. During gradient sensing, cells should also be able to amplify the shallow external gradient or stochastic noise to a much steeper spatial distribution of intracellular molecules. To achieve this function, three different network topologies have been proposed to combine with the LEGI module. One topology downstream of the LEGI module is a positive feedback that can generate switch-like response (Iglesias and Devreotes, 2008; Levchenko and Iglesias, 2002). Another way to overcome the limit of amplification is the “balanced inactivation model” with a cytosolic inhibitor (Levine et al., 2006). The cytosolic inhibitor is able to bind to membrane, inactivate the slow activator and deplete both itself and the activator from the membrane (Levine et al., 2006). A third topology to amplify the input is an excitable network motif. Gradients of chemoattractants are sensed by a LEGI module, which serves as an input for a noise-driven excitable system (Hecht et

al., 2010; Xiong et al., 2010). The LEGI model offers small amplification of the noisy input, increasing the probability to trigger the excitable network. The spatially excitable model is capable of spontaneous polarization, adaptation and gradient tracking (Xiong et al., 2010).

1.3.3 Competition and relocation

In living cells, multiple polarity spots emerge in responding to noisy input or multiple sources and compete until one wins. When the direction of stimuli changes, the polarity spot would move to or re-establish at the new position. However, the simple Turing mechanism can only explain the polarity establishment. Since the pattern is built by strong positive feedback in a simple Turing mechanism, once established, there is hardly any force to destroy the pattern. Therefore, the Turing patterns are usually independent of the strength of external stimuli and tend to lock at one site, unresponsive to future changes. For example, if the direction of pheromone gradients around yeast cells is reversed, it would take a long time to redirect the polarized GTP-Cdc42 only with the redistributed shallow free Gβγ gradient and the low concentration of remaining cytosolic Bem1-GEF complex that could rebuild positive feedback. The previous modeling based on simple Turing mechanism has already shown that the time taken to resolve competition between clusters would depend on the amount of polarized protein in each cluster (Howell et al., 2009).

To account for the formation and competition between multiple polarity spots, Meinhardt modified the basic Turing mechanism with two inhibitors: a global one to generate patterns and a delayed local one to deactivate local polarity later (Meinhardt,

1999). The additional local inhibitor enables the model to polarize spontaneously, dismantle and rebuilt local polarities and adapt rapidly to a changed external gradient (Meinhardt, 1999). A group of mass-conserved activator-substrate-depletion models also enable transient formation of multi-peak states, which then converge to a single peak solution (Otsuji et al., 2007; Otsuji et al., 2010).

1.4 Summary

Although we know the detailed biochemical interactions to transmit the spatial information of pheromone gradient to downstream effectors by free Gβγ, the precise mechanism for tracking the direction of gradient is still unclear. Knowing where to grow is a complicate task for yeast cells. First, cells need to give up the internal spatial cue from budding markers and switch to external cue of pheromone gradients. Since the bud site is still used for polarization in uniform pheromone fields and mutants of Cdc24 or Far1 (Dorer et al., 1995), cells probably first polarize at budding site, and then the free Gβγ proteins compete with position signal from Rsr1 to control the position of polarity cluster.

Another difficulty is to detect a small concentration difference across the length of a yeast cell. The size of a yeast cell is about 5 micron in diameter. If a yeast cell is in a linear gradient from 0 to 150 nM crossing 100 micron, there is only 7.5 nM difference in pheromone concentration across the cell. The fluctuation in the number of pheromone molecules due to diffusion makes the gradient detection even harder. Additionally, as discussed above, the budding signal further confuses the polarity machinery.

The third challenge is that *MAT***a**-cells secrete a protease Bar1 that degrades pheromone from *MATa* cells while sensing the pheromone gradient. Why do yeast cells degrade the signal they need? How do cells tell the small difference? How does this shallow gradient compete with the budding signals? These questions are the initial motivation of work in Chapter 2. We presented our current understanding for the first question in Chapter 2. We showed that yeast cells achieve better gradient sensing by using protease to actively modify the spatial profile of external stimulus.

Competition probably does not only occur in gradient sensing, but also controls the singularity in budding, because with or without budding markers, yeast cells produce one and only one daughter cell. Although the positive feedback in the Turing mechanism is capable of amplifying small spatial perturbations to produce multiple clusters, mathematical modeling has shown that initial clusters compete for the substrate of positive feedback until one wins, or several clusters merge into a single cluster (Goryachev and Pokhilko, 2008; Howell et al., 2009). Do yeast cells use competition to guarantee singularity in budding? If not, how do cells ensure only one polarity spot? To answer these questions, Howell et. al. developed a protocol for high temporal resolution imaging. In Chapter 3, we presented unexpected spatiotemporal dynamics of polarity establishment from the high-resolution imaging and provided possible mechanisms to explain the observed dynamics.

In chapter 4, we showed preliminary results of the spatiotemporal dynamics of Ste5, the scaffold protein that couples the information of stimulus to both polarization pathway and the activity of MAPK cascade. Chapter 5 summarized these results and discussed about some future directions.

CHAPTER 2.

Regulation of pheromone gradient during chemotropic growth via protease bar1

2.1 Overview

In the yeast *Saccharomyces cerevisiae* haploid *MAT***a** and *MATa* cells secrete cell-type-specific pheromones (**a**-factor and *a*-factor, respectively) that promote cell fusion and the formation of a *MAT***a**/*MATa* diploid. Pheromone stimulation leads to a well-defined series of events required for mating, including readily-assayed responses such as MAPK phosphorylation, new gene transcription and morphological changes. At high doses of pheromone cells arrest in G1 and form the characteristic "shmoo" morphology. However at intermediate levels of *a*-factor, *MAT***a**-cells undergo chemotropic growth in which they elongate in the direction of increasing *a*-factor concentrations (Dorer et al., 1995; Erdman and Snyder, 2001; Hao et al., 2008; Paliwal et al., 2007; Segall, 1993).

A property that distinguishes *MAT***a** from *MATa* cells is that the former secrete the protease Bar1 that degrades *a*-factor secreted by *MATa* cells (Ciejek and Thorner, 1979; Hicks and Herskowitz, 1976). *MATa* cells lack an **a**-factor specific protease. It is widely thought that Bar1 serves to "desensitize" the pheromone pathway and restore normal cell division if mating is unsuccessful (Chan and Otte, 1982). However, Jackson and Hartwell

showed that *bar1* mutant cells are poorly able to find a mating partner when presented with a mixture of pheromone-producing and non-producing *MATa* cells (Jackson and Hartwell, 1990). This finding suggests that Bar1 has an important positive role in mating, despite attenuating the initial stimulus. Using an analogy to electrostatics, Barkai *et al*. postulated that a homogenous concentration of Bar1 limits the diffusion range of *a*-factor, thereby creating local pheromone gradients that are better aligned with the direction of the nearest *MATa* cell (Barkai et al., 1998). Alby *et al*. observed that a secreted protease helps to prevent rare same-sex mating in *C. albicans* (Alby et al., 2009). Here, we combine experimental and computational approaches to explore how Bar1 promotes accurate gradient detection and proper mating behavior. In particular, we showed that Bar1 allowed cells of the same mating type to avoid one another, thereby minimizing unproductive encounters, while dynamically magnifying pheromone gradients in the direction of the opposite mating type.

2.2 Same-sex avoidance

Experiments performed in a microfluidic gradient chamber showed that *MAT***a** cells tended to avoid each other as they elongated (Fig. 2.1A, left panel). We reasoned that self-avoidance could contribute to increased mating efficiency by reducing non-productive encounters with cells of the same mating type. We reasoned further that self-avoidance behavior might be dependent on Bar1, which has been shown to have a positive role with respect to mating partner selection.

To investigate if Bar1 is sufficient to explain the self-avoidance behavior, we developed a computational platform for simulating chemotropic growth (Fig. 2.1B and

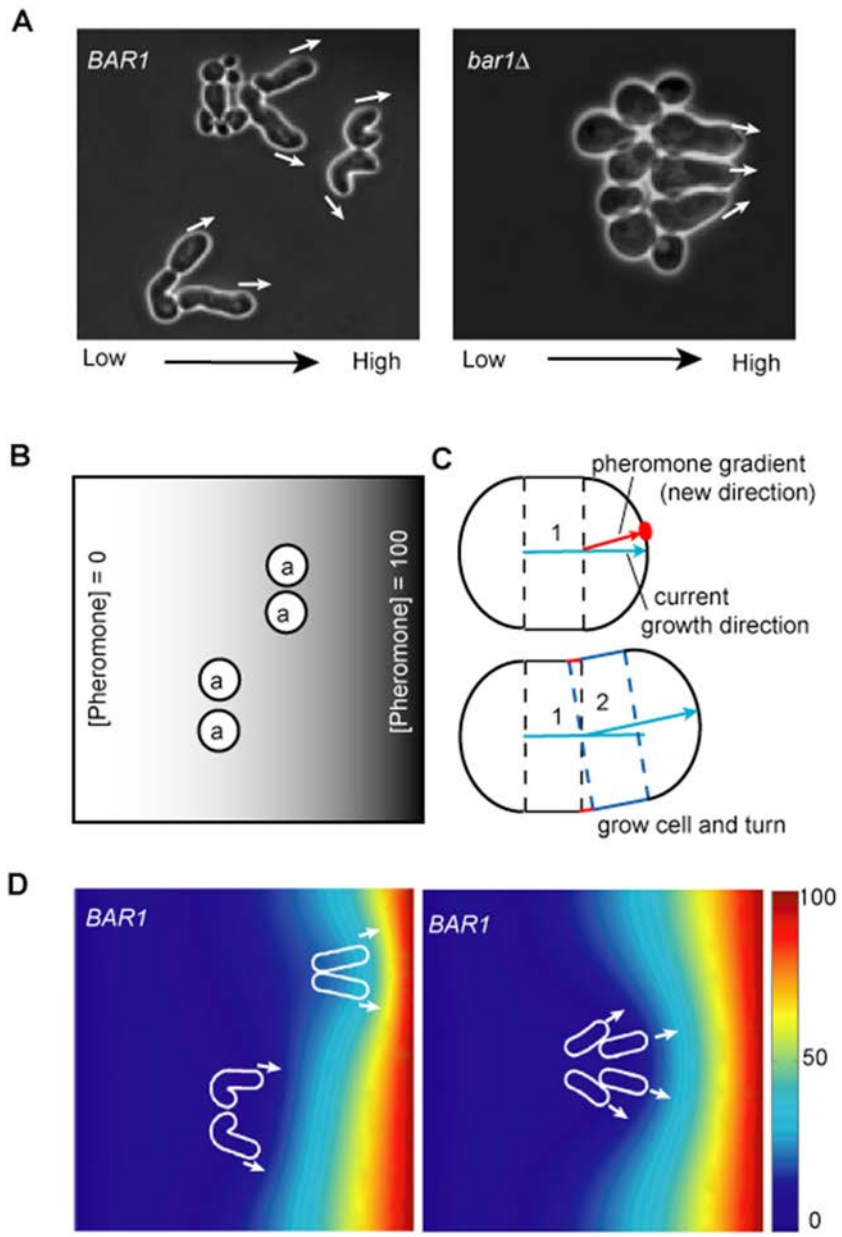

Figure 2.1. Bar1 provides a self-avoidance mechanism.
A) Experiments performed in a microfluidic gradient chamber. *BAR1* cells show self-avoidance (left panel), whereas *bar1Δ* cells tend to grow parallel to one another (right panel). Arrows indicate the direction of growth. B) Schematic diagram of the initial configuration for simulations of the gradient chamber. C) Schematic diagram of cell growth simulation. D) Simulated cell growth demonstrated that *MAT***a** cells avoid one another during chemotropic growth in a gradient chamber. Arrows indicate the direction of growth. The color bar at the right shows the color scale for pheromone concentrations (nM) within the computational domains.

C). Full details of the computational platform and justification of parameter values are

given in the Materials and Methods. The microfluidic chamber is taken to be a square domain, and *MAT***a** cells within the chamber are initially represented as circles (Fig. 2.1B). Bar1 is released from *MAT***a** cells and degrades α-factor in the surrounding fluid. To simulate the pheromone gradient inside the microfluidic chamber the pheromone concentration at the right edge of the computational domain was held at 100 nM, while the pheromone concentration at the left boundary was set at zero. The concentrations of Bar1 and pheromone are governed by Eqs. (1) and (2), respectively, in the Material and Methods. These equations are run to steady state to determine the initial concentration profiles.

The K_d for the pheromone receptor Ste2 has been reported to be approximately 5 nM (Jenness et al., 1986). Therefore, we assumed a local pheromone concentration of at least 1 nM is required to initiate a response. We also assumed gradient detection is possible for local pheromone concentrations ranging from 1-50 nM. Cell elongation is modeled by inserting successive growth segments into the cell (Fig. 2.1C). After each elongation step, the concentration profiles of Bar1 and pheromone are recalculated. To determine the initial direction of growth, the relative α-factor gradient was computed (Materials and Methods). The relative gradient is the difference in α-factor concentration across the cell divided by the average concentration over the same region and is therefore a dimensionless quantity. Based on measurements made in our microfluidics chamber, we set a relative gradient of 0.025 as the threshold for detectable pheromone gradients (Hao et al., 2008). For steeper gradients, cells elongate in the direction of the pheromone gradient. For gradients below the threshold, elongation occurs in a random direction. Once a cell has begun to elongate (hereafter “grow”), Bar1 release occurs in a polarized

fashion from the leading edge and the relative gradient is measured across the leading growth segment (Material and Methods). To model pheromone-induced synthesis of Bar1, we assumed that the synthesis rate increases proportionally to the size of the growing cell. If the gradient becomes sub-threshold during elongation, then the cell continues to grow in the same direction; otherwise the cell reorients in the direction of the gradient (Fig. 2.1C).

Our simulations indicated that Bar1 released locally from *MAT***a** cells was sufficient to allow these cells to avoid one another within the gradient chamber (Fig. 2.1D). Indeed, the results of our simulations were similar to the behavior observed experimentally (Fig. 2.1A, left panel). In particular, our simulation reproduced the situation in which two neighboring *MAT***a** cells having initiated growth opposite the α-factor gradient turned away from each other as they reoriented toward the gradient (Fig. 2.1D, left panel). In this scenario, cells lacking Bar1 would be equally likely to turn towards each other as apart from one another.

To confirm a role for Bar1 in self-avoidance, we repeated the gradient experiments with cells that lack *BAR1*. In contrast to wildtype, *bar1Δ* cells elongated parallel to one another and frequently collided (Fig. 2.1A, right panel). To quantify the effects of Bar1, we measured the angle between *MAT***a** cells that were initially adjacent in the gradient chamber (Fig. 2.2 top panel). For cells expressing Bar1, the average angle between two neighbor cells (93.9° ±2.3, n=22) was larger than that observed for the *bar1*Δ cells (43.4° ±4.0, n=15). We then measured the angle between elongating cells and the direction of the gradient (taken to be 0°). After sufficiently long times (350 min),

essentially the same number of *BAR1* and *bar1*Δ cells aligned their growth with the gradient (Fig. 2.2 bottom panel).

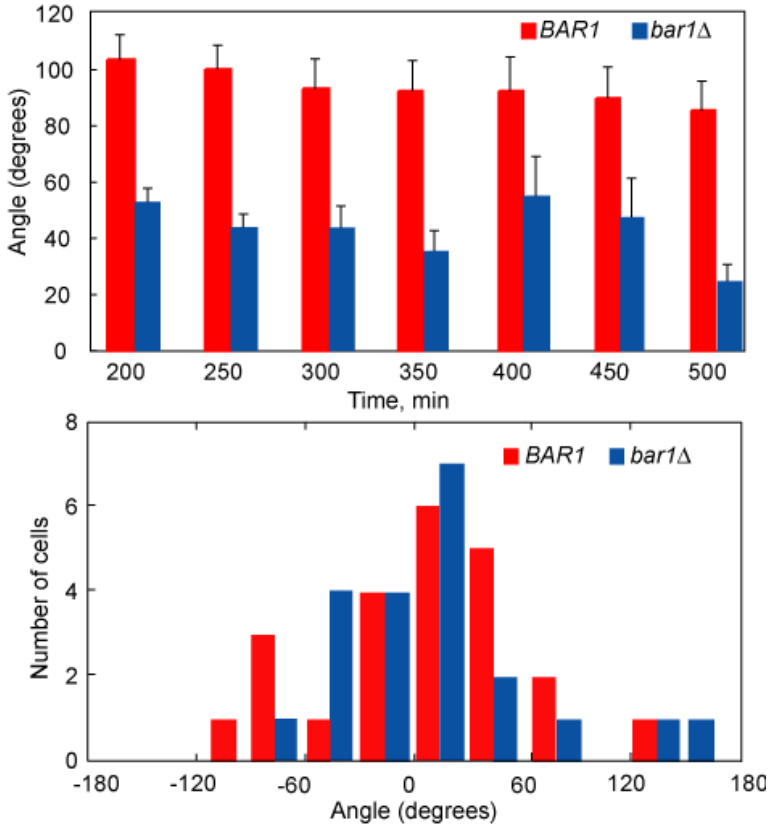

Figure 2.2 Measure gradient tracking in BAR1 and bar1Δ cells.
Top: Times series for the average angle between adjacent cells in the microfluidic chambers. The average angle is 93.9° ±2.3 (n=22) for BAR1 MATa cells (red bars), and 43.4° ±4.0 (n=15) for bar1Δ MATa cells (blue bars). Error bars correspond to 95% confidence intervals. **Bottom:** Histograms for the angle between the direction of the pheromone gradient in the microfluidic chamber and the direction of cell growth at 350 min.

2.3 Improved mating efficiency by local Bar1

Initially, to quantify the contribution of Bar1 to mating preference, we performed mating assays with *MAT***a** cells either expressing or lacking Bar1. In both cases, we mixed a population of *MAT***a** cells with an equal number of *MAT***a** or *MAT*α cells either in the absence or presence of exogenously added α-factor (Materials and Methods) (Fig.

2.3 A&B). The mating partners had complementary selectable markers, allowing quantitation of mating frequencies. Bar1 promoted mating between *MAT***a** and *MAT*α cells (Fig. 2.3A). Opposite sex mating efficiency decreased in the presence of exogenously added pheromone and decreased further in the absence of Bar1. In contrast, same sex matings increased in the presence of added pheromone and also when Bar1 was absent (Fig. 2.3B). Same sex mating between *MAT***a** cells is attributed to autocrine signaling promoted by low levels of α-factor expressed by this cell-type (Bender and Sprague, 1989; Whiteway et al., 1988). This phenomenon could account for the ability of Bar1 to limit same-sex mating and is consistent with the positive effects of exogenous pheromone (Fig. 2.3B). Diploid cells from the same-sex mating assay successfully mated with a *MAT*α-tester strain and did not sporulate, verifying these cells did not result from a rare mating-type switch in the population and subsequent opposite sex mating events (see Materials and Methods for details).

The data presented in Figs. 2.3A and B demonstrate Bar1 affects the efficiency of both *MAT***a** x *MAT*α and *MAT***a** x *MAT***a** mating. However, these experiments do not distinguish local versus global effects of the protease. For the case of *MAT***a** x *MAT*α mating, a uniform background of Bar1 could sharpen α-factor gradients (Barkai et al., 1998) and reduce saturating concentrations of α-factor to levels where gradient sensing is possible. Additionally, a global reduction of α-factor is expected to diminish the frequency of same-sex mating. Our simulations suggest that by causing *MAT***a** cells to avoid one another, local gradients of Bar1 also may play a role in reducing same-sex mating. Therefore, we devised experiments to test if the local release of Bar1 contributed to the efficiency of either *MAT***a** x *MAT*α or *MAT***a** x *MAT***a** mating.

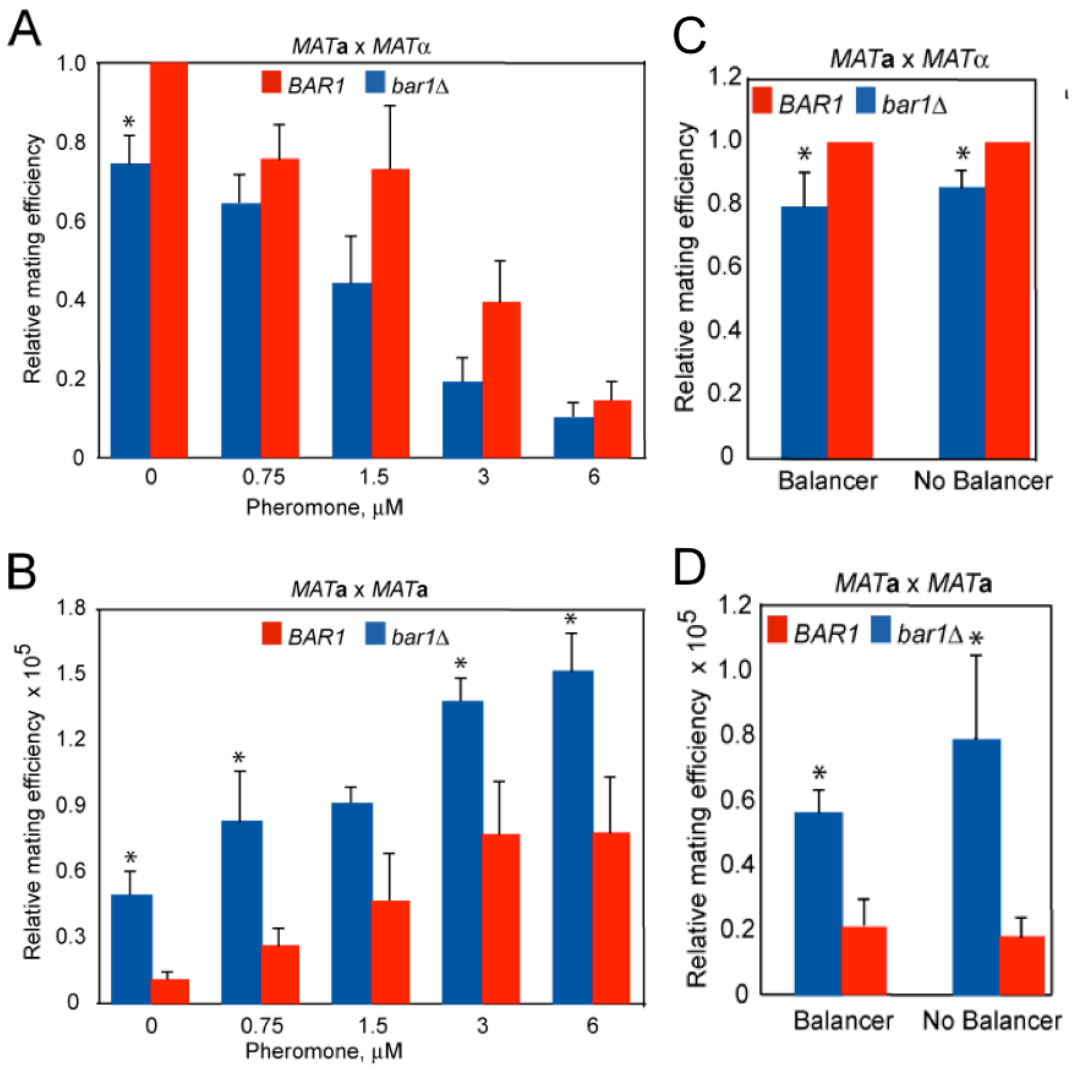

Figure 2.3 Relative mating efficiency for opposite and same sex mating.
A) *MAT***a** x *MAT*α mating (**Table 1**, crosses 2 and 4) at different concentrations of exogenous *α*-factor. B) *MAT***a** x *MAT***a** mating (**Table 1**, crosses 1 and 3) using the same concentrations of exogenous *α*-factor as in A. Mating efficiencies in A and B are relative to that for the *MAT***a** x *MATα BAR1* mixture (**Table 1**, cross 2) with no exogenous pheromone. C) *MAT***a** x *MATα* mating without (**Table 1**, crosses 2 and 4) or with (**Table 1**, crosses 10 and 12) *MAT***a** decoy cells to equalize the amount of Bar1 protease in the mating mixtures. D) *MAT***a** x *MAT***a** mating in the absence (**Table 1**, crosses 1 and 3) or presence (**Table 1**, crosses 9 and 11) of *MAT***a** decoy cells to equalize the amount of Bar1 protease in mating mixtures. Mating efficiencies without or with decoy cells in C and D are relative to the efficiency of *MAT***a** x *MATα* mixtures without (**Table 1,** cross 2) or with decoy cells (**Table 1**, cross 10), respectively. For A – D**,** the red bars correspond to *BAR1* mating partners and the blue bars correspond to *bar1Δ* mating partners. Error bars correspond to 95% confidence intervals.

These experiments involved mixtures of “mating partners” with complementing alleles to allow for the selection of diploid fusion products and “decoys” with alleles that fail to complement either partner. To keep the total amount of Bar1 and the fraction of potential mating partners comparable between mating mixtures, *BAR1* decoys were included in experiments involving *bar1Δ* mating partners and *bar1Δ* decoys were included in experiments with *BAR1* mating partners. This experimental design ensures that any observed difference in the mating efficiency (opposite or same sex) could be attributed to local effects of Bar1.

For opposite sex mating, *MAT***a** cells that expressed Bar1 mated more efficiently than *bar1Δ MAT***a** cells when decoy cells were included in the mixtures (Fig. 2.3C). In contrast, for same-sex mating in the presence of decoys *bar1Δ* cells mated more efficiently than *BAR1* cells (Fig. 2.3D). These results demonstrated that the local release of Bar1 favors opposite-sex mating while disfavoring same sex encounters. As demonstrated above, Bar1 provides a mechanism for self-avoidance. Self-avoidance would not only diminish opportunities of same sex mating, but also improve opposite sex mating by reducing the occurrence of two *MAT***a** cells competing for the same *MATα* partner.

2.4 Expanding searching area

We next performed simulations to investigate potential mechanisms for how the local release of Bar1 improves *MAT***a** x *MATα* mating. In the mating assays a large number of *MAT***a** and *MATα* cells were mixed together. In this situation, the initial *α*-factor concentration experienced by the *MAT***a** cells is expected to be fairly

homogeneous, although fluctuations in cell density will generate local regions containing clusters of *MAT***a** or *MAT*α cells. This scenario is similar to situations in the wild when a cluster of *MAT***a** cells encounters a cluster *MAT*α cells. To investigate the role of Bar1 in such a scenario, we performed simulations in which multiple *MAT***a** cells are exposed to a homogenous background of α-factor. To establish a spatially uniform α-factor concentration in the absence of *MAT***a** cells, the pheromone concentration at the boundaries of the computational domain is held fixed at 50 nM. These simulations revealed *MAT***a** cells tended to avoid one another as they elongated, so that they grew radially outward away from the center of the colony. This behavior allowed them to explore a large area in search of a mating partner (Fig. 2.4A). In contrast, when cells lacking Bar1 were started in the same initial geometry, they grew in random directions and frequently collided with each other. Consequently these cells searched a reduced area (Fig. 2.4C) and would therefore encounter fewer potential mating partners.

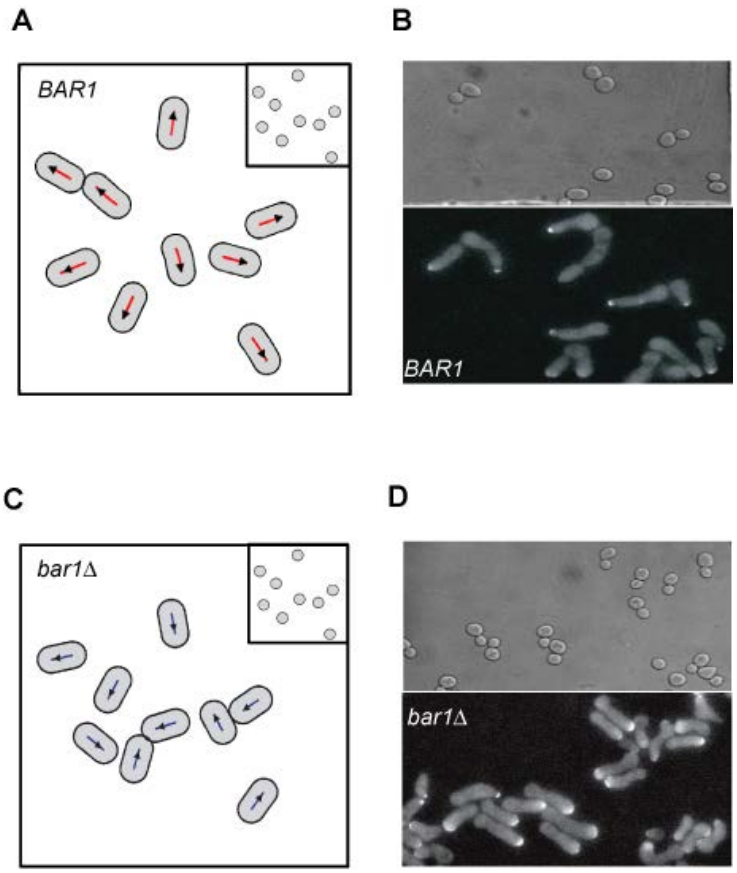

Figure 2.4. Bar1 increases the search area of *MAT*a cells.
A) Simulated growth of *BAR1* cells occurs radially outward from the center of the colony. Arrows indicate the direction of growth. **Inset**: The initial distribution. B) Growth of *BAR1* cells (BY4741-15) exposed to a constant pheromone background of 100 nM in microfluidic chamber. The upper panel corresponds t = 0 and lower panel to t = 315 min. C) Simulated growth of *bar1Δ* cells. The cells grow in random directions. **Inset**: The initial distribution. D) Growth of *bar1Δ* cells (BY4741-30) exposed to a constant pheromone background of 10 nM in microfluidic chamber. The upper panel corresponds t = 0 and lower panel to t = 415 min. Large number of pairs of cells exhibiting parallel growth. In both B and D, the upper panel is a DIC image showing the initial distribution of cells and the lower panel shows leading edge of polarization via Bem1-GFP.

To test the results of these simulations, we used the microfluidic chamber to expose both *BAR1* and *bar1Δ MAT***a** cells to homogeneous pheromone concentrations. We tracked the direction of cell growth by following green fluorescent protein fused to Bem1 (Bem1-GFP), a protein that marks the leading edge of polarized growth (Irazoqui et al., 2003). We found clear qualitative agreement between the simulations and the

behavior of both the *BAR1* (Fig. 2.4A and B) and *bar1Δ* strains (Figs. 2.4C and D). We next investigated the range of pheromone concentrations over which *MAT***a** cells avoid each other during elongated growth. The upper limit for the α-factor concentration is roughly 150 nM, above which cells do not elongate but form well-defined mating projections (data not shown). The lower limit is roughly 50 nM, below which the cells do not respond to pheromone. Between these limits (75, 100, and 120 nM), Bar1 expressing cells exhibit self avoidance (Supplemental Movies). At doses compatible with elongated growth in *bar1Δ* cells (5-30 nM) the self avoidance behavior is absent (data not shown).

One striking feature seen for the case of *bar1Δ* cells is the high frequency of pairs of cells that elongated parallel to one another. These pairs represent mother and daughter cells that initially polarized toward each other at the former bud site. The direction of polarization of both cells then rotated until growth was no longer occluded. Because these cells lack Bar1, the pairs continue to grow parallel as predicted. Of the 55 mother/daughter pairs counted, 45 exhibited parallel growth (31 grew in the same direction, 14 grew in opposite directions). By contrast, in the *BAR1* strain, none of 62 mother/daughter pairs exhibited parallel growth. This ability of Bar1 to prevent mother/daughter pairs from growing parallel to each other may be important in preventing competition for the same mating partner.

2.5 Amplifying pheromone gradients during elongation

Our results indicated that spatial heterogeneities in Bar1 concentration played an important role in shaping the local α-factor concentration. To determine how Bar1 improved the efficiency with which opposite mating types located each other, we used our computational platform to investigate several scenarios involving *MAT***a** and *MAT*α

cells. In the first case, a single *MAT***a** cell was presented with two potential mating partners (Fig. 2.5A inset) but was placed closer to the *MAT*α cell on the left. In this geometry, both *BAR1* and *bar1*Δ cells can detect the initial pheromone gradient and follow the same trajectory as they elongate. However, the initial gradient experienced by the *BAR1* cell was larger than that of the *bar1*Δ cell and sharpened greatly as the *MAT***a** cell elongated (Fig. 2.5A, red curve). In contrast, without Bar1 the gradient remained shallow (Fig. 2.5A, blue line).

Next we considered a geometry in which *BAR1* and *bar1*Δ cells were able to detect α-factor, but initially unable to detect a gradient. This initial condition is accomplished by placing the *MAT***a** cell slightly to the left of the mid-point between the two *MAT*α cells. In this case, both cell types were expected to polarize in a random direction. We tested three representative initial growth directions (Fig. 2.5B, inset). In all cases, a super-threshold gradient quickly developed as the cell expressing Bar1 grew (Fig. 2.5B, red lines), enabling this cell to reorient its direction of growth and find the nearest mating partner (Fig 2.5B, inset - red arrows). In contrast, the pheromone gradient across the *bar1*Δ cell remained below the detectable limit (Fig. 2.5B, blue lines), and cell growth proceeded in the original direction of polarization (Fig. 2.5B, inset blue arrows).

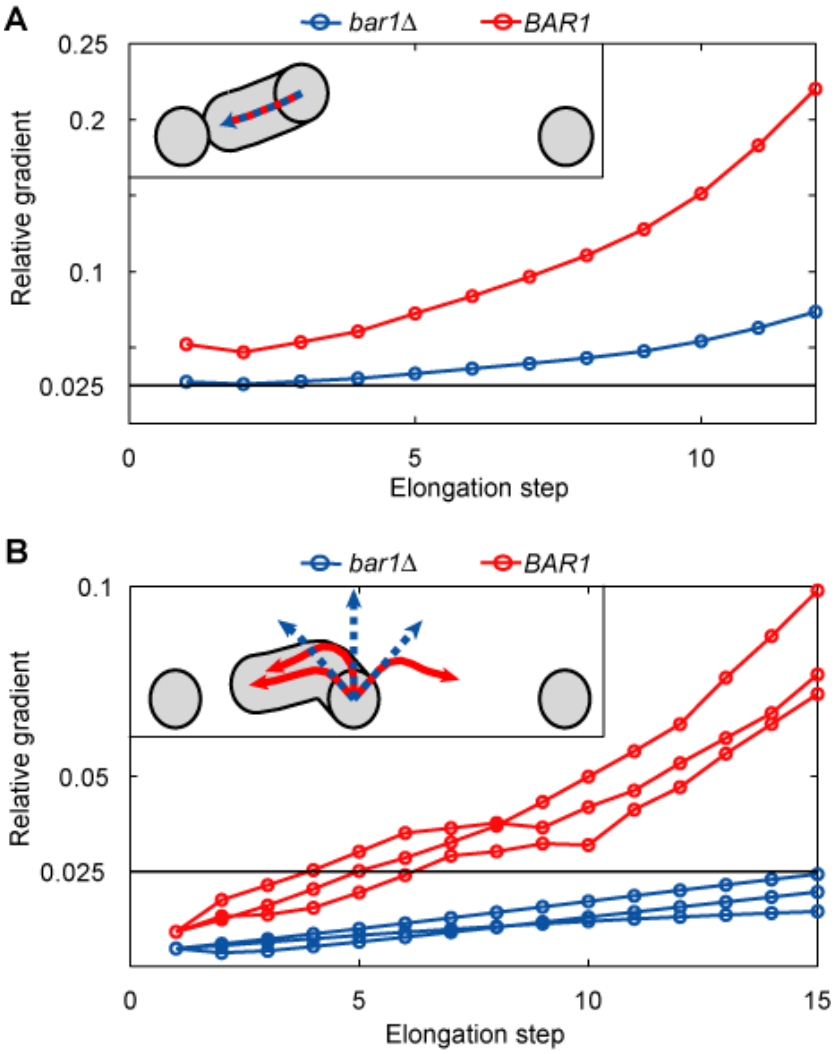

Figure 2.5. Local release of Bar1 amplifies pheromone gradients during chemotropic growth.
A) The relative pheromone gradient (maximum difference in pheromone concentration across the leading growth segment divided by the average concentration over that segment) measured by a *MAT***a** cell expressing Bar1 (red curve) or lacking Bar1 (blue curve) as a function of the elongation step. Inset: the *MAT***a** cell is placed close enough to the left *MAT*α cell so that both the *BAR1* (red line) and *bar1Δ* (blue line) cells can detect a gradient. Arrows indicate the direction of growth. B) The same as in **A** except the *MAT***a** cell is placed near the midpoint of the two *MAT*α cells, but slightly closer to the left cell (**Inset**). In this scenario, the local release of Bar1 allows *MAT***a** cells to reorient when the initial relative gradients of α-factor are sub-threshold and polarization occurs in a random direction.

Our results suggest that Bar1 improves mating efficiency by progressively amplifying the relative pheromone gradient across *MAT***a** cells, because the *MAT***a** cell acts like a pheromone sink where pheromone is continuously degraded by Bar1. If we

make the simplifying assumptions that *MAT***a** cells are perfect sinks (that is they absorb all α-factor near them) and *MAT*α cells are a constant source of pheromone, then the relative α-factor gradient between the two cells increases as the inverse of the distance between them. This prediction is in qualitative agreement with the results of our simulations (Fig. 2.5 A and B). Thus, our investigations suggest that the release of Bar1 by *MAT***a** cells reshapes pheromone concentrations to amplify gradients toward appropriate mating partners. An added advantage of Bar1 remaining highly localized around *MAT***a**-cells is that gradient amplification is achieved without a drastic reduction in the overall level of α-factor.

Finally, we investigated a more complex geometry in which a pair of *MAT***a** cells are presented with two potential *MAT*α mating partners (Fig. 2.6). Both *MAT***a** cells were positioned closer to the *MAT*α cell on the left. In the absence of Bar1, the pheromone gradients were sub-threshold (data not shown). If the Bar1 concentration was assumed constant and equal to the concentration near the surface of a *MAT***a** cell (1.6 nM), then both *MAT***a** cells detected a gradient and approached the *MAT*α cell on the left (Fig. 2.6B). However, when the *MAT***a** cells released Bar1, the top *MAT***a** cell grew away from the bottom *MAT***a** cell and toward the *MAT*α cell to the right (Fig. 2.6C). This result held for a range of initial geometries (Fig. 2.6A). These simulations showed how self avoidance through the local release of Bar1 can prevent competition for the same mating partner and thereby improve mating efficiency.

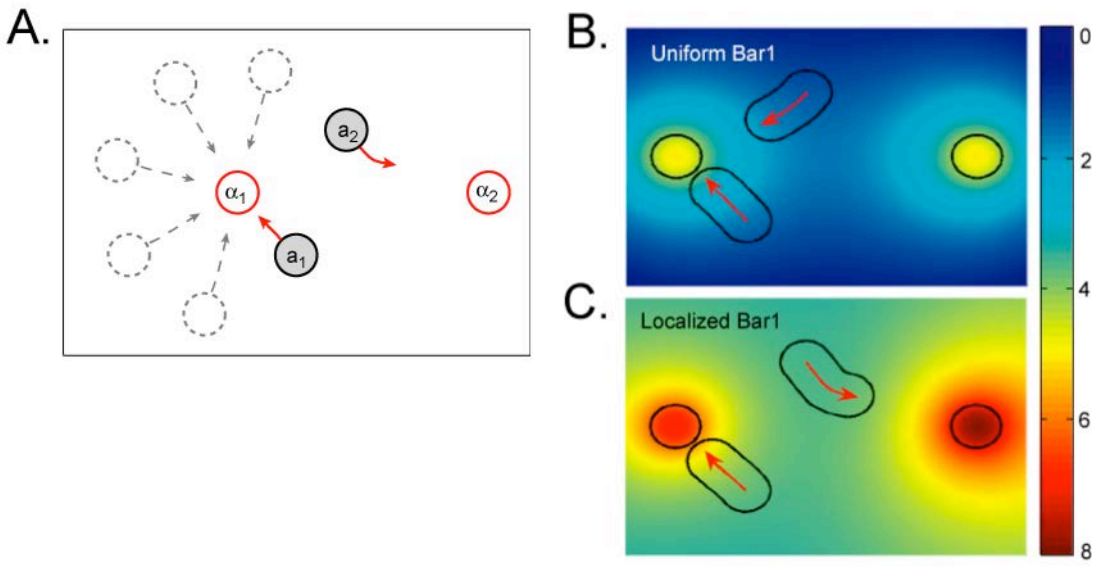

Figure 2.6. Bar1 allows *MAT*a cells to find unique mating partners.
A) Two *MAT***a** cells (a_1 and a_2) are presented with two potential *MAT*α mating partners (α_1 and α_2). The dashed gray circles represent other initial position for a_1 that were tested and in each case produced similar results. The lines with red arrow heads represent the direction of growth. B) In the presence of a uniform background of Bar1, a_1 and a_2 compete for α_1. C) When a_1 and a_2 locally release Bar1, a_2 grows away from a_1 and toward α_2 enabling both cells to find a unique mating partner. The color bar at the right shows the color scale for pheromone concentrations (nM) within the computational domains.

2.6 Discussion

Bar1 promotes mating efficiency despite its ability to degrade the mating stimulus (Chan and Otte, 1982; Ciejek and Thorner, 1979; Jackson and Hartwell, 1990). Previous computational studies have investigated the role of Bar1 in mating. Barkai *et. al*. (Barkai et al., 1998) proposed that Bar1 improves the alignment of the pheromone gradient with the direction of the nearest *MAT*α-cell. Andrews *et. al*. (Andrews et al., 2010) extended this work to show that the local release of Bar1 increases the gradient of liganded receptor across a *MAT***a** cell. Here, we considered how the α-factor gradient is dynamically modified as yeast undergo chemotropic growth and navigate toward mating partners. Our results indicate that Bar1 dramatically sharpens the relative pheromone

gradient as *MAT***a** cells elongate. An important consequence is that *MAT***a** cells can efficiently adjust their direction of elongation, if initial growth is not toward a mating partner.

Our investigations also revealed that local accumulation of Bar1 causes a depletion of α-factor between adjacent *MAT***a** cells, which in turn produces local pheromone gradients that promote self avoidance. Thus, the continuous reshaping of local pheromone gradients enables *MAT***a** cells to efficiently locate a suitable partner while avoiding interactions unlikely to produce a successful mating event. The insights from our simulations are supported by our experimental findings showing that *bar1Δ* cells do not exhibit avoidance and instead collide and grow in parallel with each other. Consequently *bar1Δ* cells have increased frequency of *MAT***a**-*MAT***a** mating. Although the effects of Bar1 on same-sex matings are significant, they are substantially less than those reported for the distantly-related yeast *Candida albicans* (Alby et al., 2009). Under physiological conditions *C. albicans* exist primarily as **a**/α diploids and rarely mate. This physiology contrasts with that of *S. cerevisiae*, where opposite sex mating is an important part of its life cycle. Thus Bar1 alone may provide a sufficient impediment to same sex mating in *C. albicans* but multiple mechanisms are in place to prevent the detrimental consequences of same sex mating in *S. cerevisiae.*

Analogous events have been reported in other systems. For instance the mechanisms that promote directed migration of neutrophils and *Dictyostelium discoideum* have been extensively studied (Van Haastert and Devreotes, 2004). In these examples secreted enzymes serve to degrade the initiating signal. In *D. discoideum*, secreted cAMP serves to induce cell migration, aggregation and differentiation. cAMP is

in turn degraded by the secreted phosphodiesterase PdsA. In the absence of PdsA, gradient detection and cellular migration is compromised (Garcia et al., 2009). Thus just as pheromone gradients in yeast are shaped by the secretion of Bar1, cAMP gradients in *D. discoidium* may likewise be shaped by a secreted cyclic nucleotide phosphodiesterase.

In summary, our findings indicate that hormone proteases can serve dual functions, to reduce the signal, as well as shape concentration gradients for optimal signal detection and responsiveness. More generally, our findings reveal that cells can dynamically remodel their environment to avoid non-productive cell-cell interactions.

2.7 Computational Methods

2.7.1 Framework for chemotropic growth

We developed a computational platform for studying yeast chemotropic growth. This platform is built on COMSOL with MATLAB (Comsol Inc., Burlington, MA). Schematic diagrams of the simulation platform are given in Figs. 2.1B and C. The process for simulating chemotropic growth is as follows:

1. The computational domain that contains the cells is taken to be a square. Initially, cells are assumed to have a circular geometry (Fig. 2.1B). Biochemical species, reactions, boundary conditions and initial conditions are defined in the relevant domains (see below).
2. We assume that cell growth occurs on a longer timescale than the chemical reactions and thermal diffusion. Therefore, all chemical species reach their steady state before cell growth occurs. This simplification allows us to separate solving the reaction-diffusion equations from growing the cells.

Solving the reaction-diffusion equations produces the spatial profiles for the extracellular pheromone and Bar1 concentrations.

3. The location of the maximum (Pmax) and minimum (Pmin) pheromone concentration around each cell is found. The relative gradient is then computed as: 2 (Pmax-Pmin)/(Pmax+Pmin). If the absolute level of pheromone and the relative gradient are above threshold, a narrow rectangular segment is inserted between the half circle defined with Pmax as its midpoint and the half circle defined with Pback as its midpoint (Fig. 2.1C). Otherwise the cell is elongated in a random or pre-specified direction. The half circle, which contains Pmax and is moved to accommodate S1, is defined as the leading edge. The other half circle is taken to be the back of cell and remains fixed throughout the simulation.
4. Following cell elongation, the program recomputes the steady-state profiles of the reaction-diffusion equations.
5. In later growth steps, only the pheromone concentration across the leading segment is considered, because this is where growth occurs. For this case the relative gradient is computed as 2(Pmax-Pmin)/(Pmax+Pmin), where Pmax and Pmin are the maximum and minimum pheromone concentration, respectively, over the leading segment. If the relative gradient is above threshold, a new segment is inserted between the leading edge and the previous segment and rotated by angle formed by the previous direction of growth and Pmax (Fig. 2.1C). Otherwise the new segment is inserted in the

same direction as the previous one. Steps 4 and 5 are repeated until all cells grow to the desired length or two cells collide with each other.

2.7.2 Chamber simulations

For the gradient simulations (Fig. 2.1B), the concentration of pheromone on the left and right edges of the chamber domain is fixed at 0 and 100 nM, respectively, which creates a linear gradient across the chamber domain. In this case, no flux boundary conditions are used along the top and bottom edges of the chamber. For the chamber simulations with a constant pheromone background (Fig. 2.4), the pheromone concentration is fixed at all boundaries of the computational domain. The boundary conditions for Bar1 are absorbing at the four edges (i.e., the concentration is taken to be zero at these boundaries). The pheromone and Bar1 concentrations are computed from the following equations:

$$\frac{\partial[Bar1]}{\partial t} = D_{bar1}\Delta[Bar1] + s_b(x,y) - d_b[Bar1] \quad (1)$$

$$\frac{\partial[Ph]}{\partial t} = D_{ph}\Delta[Ph] - k_b[Bar1][Ph] - d_{ph}[Ph] \quad (2)$$

where D_{bar1} and D_{ph} are the diffusion coefficients for Bar1 and pheromone, respectively; $s_b(x,y)$ is the flux of Bar1 from **a**-cells; d_b and d_{ph} are the rate constants for degradation of Bar1 and pheromone, respectively, and k_b is the rate constant for Bar1 mediated degradation of pheromone. Initially, *MAT***a** cells are assumed to emit Bar1 at constant rate uniformly across the entire cell. Once the cells begin to elongate, Bar1 is released in a polarized fashion exclusively from the leading growth segment. The assumption of polarized release of Bar1 during chemotropic growth is not necessary to reproduce the

qualitative features of the model. To simulate pheromone induced Bar1 expression, the flux out of the leading segment is increased in proportion to the size of the cell.

2.7.3 Simulations with *MAT***a** and *MAT*α cells

For simulations involving *MAT***a**- and *MAT*α- cells (Figs. 2.5 and 2.6), *MAT*α cells are assumed to emit α-factor uniformly across the cell surface. Again Bar1 is released from *MAT***a** cells. The equations for the pheromone and Bar1 concentrations are the same as Eqs. (1) and (2) with the addition of a source term in Eq. (2), $s_{Ph}(x,y)= 75$ nM/s, for the release of α-factor from *MAT*α cells. The growth direction is determined using the relative gradient as described above. The boundary conditions for α-factor and Bar1 are no flux.

2.7.4 Parameter estimation

There are 7 model parameters: the synthesis and degradation rates of Bar1 and pheromone (s_{Bar1}, d_{Bar1}, s_{ph}, d_{ph}), degradation of pheromone by Bar1 (k_{Bar1}), and diffusion of pheromone and Bar1 (D_{ph}, D_{Bar1}). We estimated the synthesis, degradation and diffusion rates of pheromone based on the molecules size and the generation of a reasonable concentration profile around a *MAT*α-cell.

We assume that spatial gradients of pheromone and Bar1 only exist in two dimensions (x and y). This assumption is valid for the microfluidic chamber, which has a height of h = 5 microns and for the mating assays, which take place on an agar surface. The pheromone concentration C_p is measured in units of nanomolar (nM). In the absence

of other cells, the steady-state profile for C_p around a *MAT*α cell is described by the following equation:

$$\begin{cases} D_P \nabla^2 C_P(r) - d_P C_P(r) = 0 \\ D_P \left. \dfrac{\partial C_P(r)}{\partial r} \right|_{r=r_0} = -j_P \\ C_P(\infty) = 0 \end{cases} \quad (3)$$

where $\nabla^2 C_P(r) = \dfrac{\partial^2 C_P(r)}{\partial r^2} + \dfrac{1}{r}\dfrac{\partial C_P(r)}{\partial r}$ is the Laplace operator in polar coordinates, d_P is the pheromone degradation rate, D_p is the diffusion coefficient, and j_P is the pheromone flux density (molecules/(area-sec)) at the cell boundary located at r_0. The flux density j_P is computed as follows. Assume pheromone molecules are synthesized inside the cell at a rate of of S_X (nM/s) and released uniformly over the surface of the cell. Then the flux per unit area is the product of synthesis rate and the ratio of the cell volume to surface area $j_p = S_X r_0/3$.

The steady-state solution of Eq. (3) is

$$C_P(r) = \frac{j_P K_0(\sqrt{\frac{d_P}{D_P}} r)}{\sqrt{d_P D_P} K_1(\sqrt{\frac{d_P}{D_P}} r_0)} \quad (4)$$

where K_0 and K_1 are modified Bessel function of the second kind. The diffusion coefficient of pheromone is estimated from its molecular weight to be 125 $\mu m^2/s$. Based on Eq. (4), we chose the synthesis rate of pheromone to be 75 nM/s and the degradation rate to be $0.005 sec^{-1}$. With these values the pheromone concentration of 5nM at the surface of a *MAT*α cell and drops to 20% of this value 100 μm away from the source.

This synthesis rate requires a *MAT*α-cell with 5 μm diameter to produce 3000 pheromone molecules per second.

Bar1 emitted from a *MAT***a** cell satisfies an equation analogous to Eq. (3). Because Bar1 is substantially larger than pheromone, we chose its synthesis rate to be 1.5 nM/s, 50 times slower than that of pheromone. Once a *MAT***a** cell begins to elongate, we assumed Bar1 is released exclusively from the leading edge. We assumed Bar1 degrades at a rate of 0.05 sec^{-1}, which is 10 fold faster compared with pheromone. We take the diffusion coefficient of Bar1 to be 6.25 $\mu m^2/s$, which is 20 times slower than pheromone diffusion coefficient. With these values the concentration of Bar1 in unit volume at the surface of the cell is 0.85nM and drops to 20% of its value at distance of 13 μm. The rationale for these choices is given next.

2.7.5 Robustness in parameter values

Among the 7 free parameters, we systematically varied s_{Bar1}, d_{Bar1}, s_{ph} and k_{Bar1} and quantified their effects on self-avoidance and sharpening of the pheromone gradient.

Self-avoidance of adjacent *MAT*a cells. For *MAT***a** cells to show self-avoidance (an angle of >20° between adjacent cells) the model parameters should satisfy two conditions:

1) Bar1 dependent degradation of pheromone (k_{Bar1}[Bar1]) needs to be around 2 orders of magnitude larger than spontaneous pheromone degradation (d_{ph}) (Fig. 2.7A). This ratio can be increased by increasing the Bar1 related parameters s_{Bar1} and k_{Bar1}. Decreasing the Bar1 degradation rate d_{Bar1} also affects this ratio.

However, this parameter increases the width of Bar1's distribution around a *MAT***a** cell, which is in opposition to the second condition.

2) The distribution of Bar1 is required to be localized around *MAT***a**-cells (Fig. 2.7B). If the Bar1 distribution is too broad, then because of condition 1, the pheromone concentration around multiple *MAT***a** cells is reduced to low levels, making the establishment of sharp pheromone gradients difficult and the angle between two neighboring *MAT***a** cells is small. There are two ways to restrict the Bar1 distribution, rapid degradation or slow diffusion. One alternative effect that would effectively limit the distribution of Bar1 around *MAT***a** cells is if a portion of the protease remained trapped in the periplasmic space between the cell wall and the plasma membrane.

Sharpening pheromone gradients. We investigated how the ability of Bar1 to sharpen pheromone gradients depends on the model parameters s_{Ph}, d_{Bar1}, and k_{Bar1} using the same geometry of *MAT***a** and *MAT*α-cells as in Fig. 2.5B. The synthesis rate of pheromone, s_{Ph}, changes the amount of pheromone around a *MAT*α cell, but did not affect the relative gradient. Similar to improving self-avoidance, increasing the ratio of $k_{Bar1}[Bar1]/ d_{ph}$ sharpens pheromone gradients (Fig. 2.7B). One way to increase this ratio is to decrease the Bar1 degradation rate d_{Bar1}, which broadens the Bar1 distribution and increases the amount of Bar1 in the medium. A uniform background of Bar1 is sufficient to generate large pheromone gradients, because under this condition the α-factor distribution is proportional to $K_0(\sqrt{\frac{k_{Bar1}[Bar1]}{Dp}}r)$ which asymptotically decreases as $\exp(-(k_{Bar1}\,[Bar1]/D_p)^{1/2}\, r)$ for large r (Barkai et al., 1998). However, this sharpening

of the gradient comes at the cost of a significant reduction in the pheromone concentration, making it easy for the absolute amount of pheromone to drop below a detectable level. Keeping the Bar1 concentration localized around *MAT***a** cells allows α-factor concentrations to remain relatively high, while at the same time providing a mechanism for amplifying the pheromone gradient as *MAT***a** cells elongate.

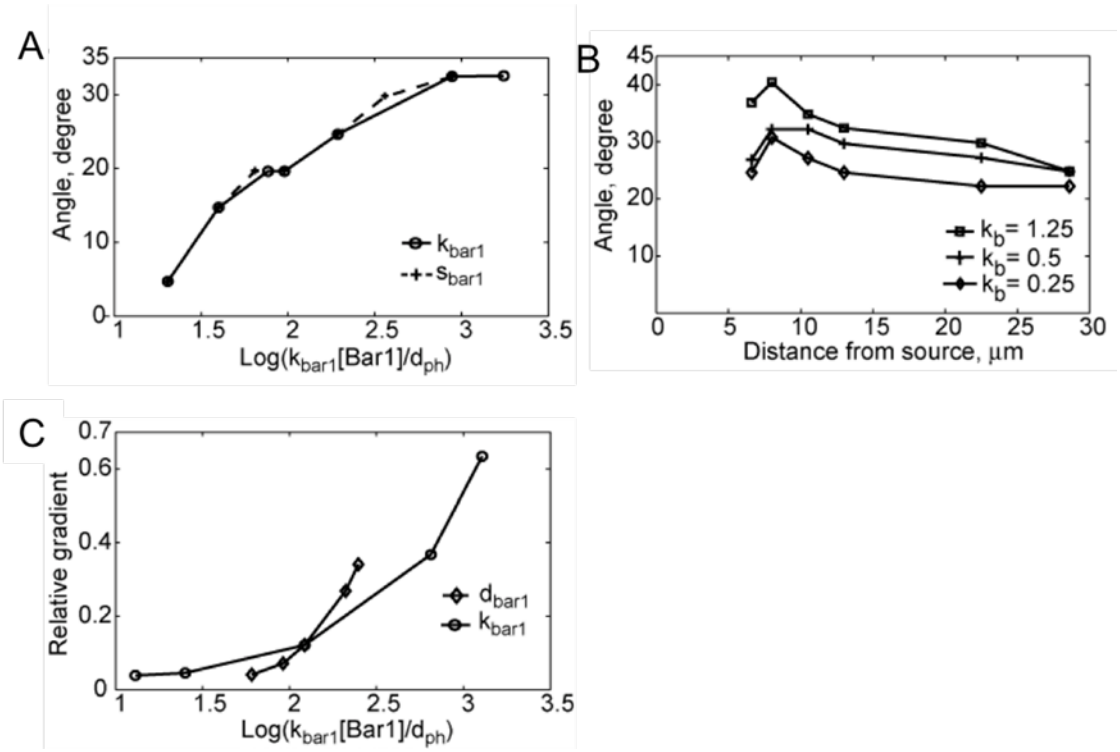

Figure 2.7. Robustness in parameter values.
A) The angle between two adjacent *MAT***a** cells as function of Log(k_{Bar1} [Bar1]/d_{ph}). The solid line: increasing k_{Bar1}; dashed line: varying the Bar1 synthesis rate, s_{Bar1}. Both parameters are varied over two orders of magnitude. B) The angle between two adjacent *MAT***a** cells as a function of the distance from a *MAT***a** cell at which the Bar1 concentration drops to 20% of its value. This distance is increased by decreasing d_{Bar1} (0.5, 0.25, 0.1, 0.05, 0.01 and 0.005 sec^{-1}). The three different curves represent different values of k_{Bar1}. C) The relative gradient as a function of Log(k_{Bar1} [Bar1]/d_{ph}). The circles: changing k_{Bar1} ; the diamonds: changing d_{Bar1}.

CHAPTER 3.

Modeling spatiotemporal dynamics in polarization pathway during budding

3.1 Overview

Polarity establishment employs an evolutionarily ancient machinery centered around the conserved Rho-family GTPase Cdc42p (Park and Bi, 2007). During polarization, GTP-Cdc42p becomes concentrated at the cortical site destined to be the "front" of the cell. In response to cell-cycle cues, *Saccharomyces cerevisiae* cells concentrate polarity regulators at one of several predictable sites defined by landmark proteins (Park and Bi, 2007). In the absence of interpretable landmarks (e.g. in *rsr1*Δ mutants), however, yeast cells nevertheless polarize and bud at a single, random site (Bender and Pringle, 1989b; Chant and Herskowitz, 1991b). Such "symmetry breaking" polarization requires the scaffold protein Bem1p, which associates with the Cdc42p-directed guanine-nucleotide-exchange factor (GEF), Cdc24p, and a p21-activated kinase (PAK) (Bose et al., 2001; Gulli et al., 2000; Irazoqui et al., 2003; Kozubowski et al., 2008). This complex is thought to mediate a positive feedback loop that enables small stochastic clusters of GTP-Cdc42p to become amplified (Kozubowski et al., 2008). Mathematical modeling suggested that although more than one stochastic cluster could be amplified in this

manner, Bem1p complexes would soon become depleted from the cytoplasm, after which the clusters would compete with each other and the largest one would win (Goryachev and Pokhilko, 2008; Howell et al., 2009). Thus, Bem1p-mediated positive feedback combined with competition for limiting Bem1p complexes could explain why *rsr1*Δ yeast cells polarize to one and only one position (Howell et al., 2009).

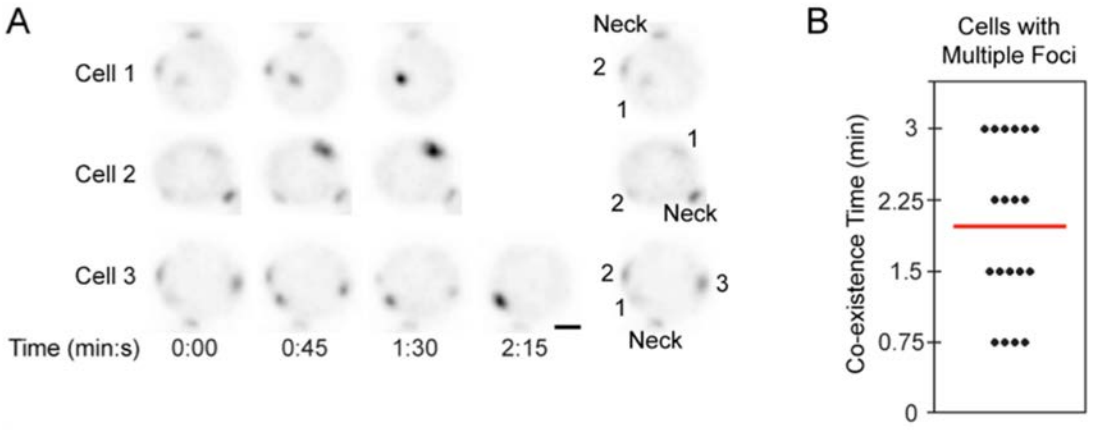

Figure. 3.1. Competition and merging of Bem1-GFP clusters during polarity establishment

Inverted images (so dark spots represent concentrations of Bem1-GFP) of *rsr1*Δ/*rsr1*Δ *BEM1-GFP*/*BEM1-GFP* cells breaking symmetry. Neck: the "old" neck signal in the attached daughter cell is often still visible. Time in min:sec. Scale bar 2 μm. A) Growth of multiple clusters and resolution to a single cluster. Bem1 clusters (numbered in the key at right) in 3 representative cells: t=0 indicates the first detection of polarized signal. B) The co-existence time between the first detection of 2-3 faint clusters and the first frame showing a single cluster is plotted (n=19). **The experiments were designed and conducted by Audrey Howell, Chi-Fang Wu and Dr. Daniel Lew.**

The competition hypothesis predicts that polarity establishment should frequently proceed via a transient intermediate stage with more than one polarity cluster, but there is limited experimental evidence for such intermediates as only rare, fleeting two-cluster instances were identified in *rsr1*Δ cells (Howell et al., 2009). Thus, either competition occurs very rapidly, or some other mechanism ensures that only a single cluster develops. To distinguish between these possibilities, we developed higher-resolution filming

conditions that circumvented the phototoxicity of previous protocols. We now document the frequent formation of more than one polarity cluster, and rapid competition between clusters, during symmetry-breaking polarization in *rsr1*Δ cells. Rapid filming of initial polarity establishment also revealed unexpected oscillatory clustering of polarity factors, indicative of negative feedback. Mathematical modeling suggested that negative feedback could confer advantageous features, including robustness and rapid competition between clusters even in the face of increasing polarity factor concentrations. Experimental tests confirmed these predictions, suggesting that negative feedback improves the robustness of the yeast polarity circuit.

3.2 Oscillatory polarization from high-resolution imaging

To reveal the dynamics in the early stage of polarity establishment, Howell et. al. developed a new protocol for high-resolution imaging without phototoxicity (Howell et al., 2012). By synchronizing cells in hydroxyurea (HU), cells function normally under increased light exposure and are much less photosensitive compared with unsynchronized cells. This protocol enabled the high-frequency imaging that could capture fine spatiotemporal dynamics. In diploid cells breaking symmetry (*rsr1*Δ/*rsr1*Δ), 28% of cells (n = 67) with two or three initial clusters of polarized scaffold Bem1p-GFP kept only a single cluster at bud emergence, through either competition between multiple clusters or merging nearby clusters (Fig. 3.1A). The duration to determine to a single cluster was within 2 min on average (Fig. 3.1B). These data indicate that the singularity of polarization cluster is achieved by rapid competition and merging between multiple initial polarization clusters.

Frequent imaging at early stage of polarization revealed unexpected oscillations of the polarity spot. Bem1p-GFP dissipated rapidly after concentrated at a polarity site, and then repeated this accumulation-dispersal cycle one or two times until it finally stabilized at the budding site (Fig. 3.2A and B). The intensity of Bem1p-GFP polarity spot in the second and third cycles is dimmer than that during the first cycle in the

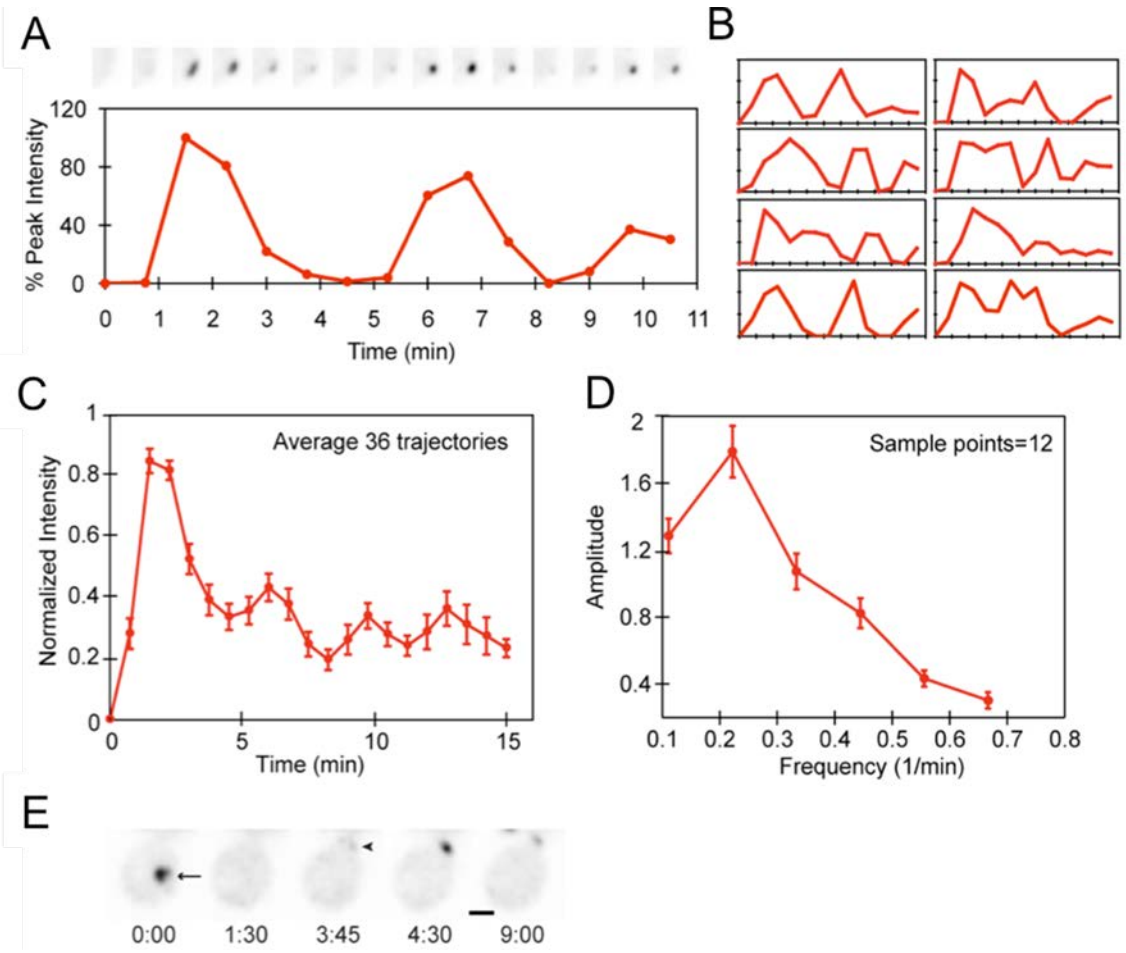

Figure. 3.2. Oscillation of Bem1p-GFP clusters before bud emergence
A) Representative cell displaying oscillatory clustering of Bem1. Top: Cropped images of the polarization site at 45 s intervals: t=0 is 45 s before the first detection of polarized signal, and trace ends at bud emergence. Bottom: Amount of Bem1-GFP in the cluster. B) Bem1 accumulation in 8 other cells. C) Averaged plot from 36 cells aligned by the first peak. D) Power spectrum analysis of 12 cells with longest traces. E) Representative cell displaying relocating cluster of Bem1. An initial cluster (arrow) dispersed, and a new cluster appeared (arrowhead) at what became the bud site. **The experiments were designed and conducted by Audrey Howell, Chi-Fang Wu and Dr. Daniel Lew.**

averaged behavior of multiple cells (Fig. 3.2C). In 15% of cells with a single initial cluster, the polarized Bem1p-GFP spot is dispersed completely and re-polarized at a different position (Figure 3.2E).

Oscillatory behavior was not unique for Bem1p; other polarity factors displayed similar dynamics. Cdc24p, and Cdc24-GFP and Bem1p-tdTomato signals oscillated in

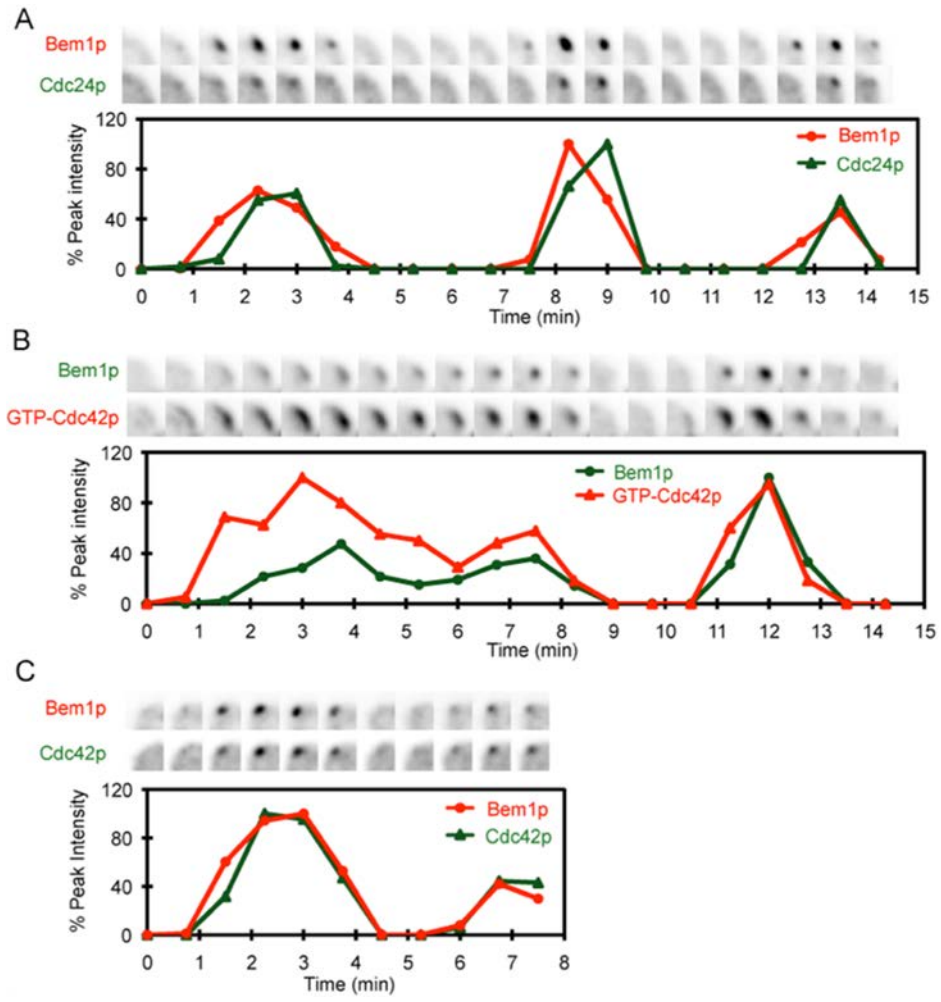

Figure. 3.3. Cdc42p and Cdc24p polarization dynamics are coincident with Bem1p

A) Bem1p-tdTomato and Cdc24p-GFP oscillate in parallel. Top: Cropped images of the polarization site at 45 s intervals. Bottom: Quantification. B) Bem1p-GFP and GTP-Cdc42p (visualized using the PBD-tdTomato probe) oscillate in parallel. C) Bem1p-tdTomato and GFP-Cdc42p oscillate in parallel. **The experiments were designed and conducted by Audrey Howell, Chi-Fang Wu and Dr. Daniel Lew.**

parallel (Fig. 3.3A). Fluorescent probes to detect GTP-Cdc42p (Tong et al., 2007) and total Cdc42p (Bi et al., 2000) also revealed oscillatory signals that paralleled Bem1p

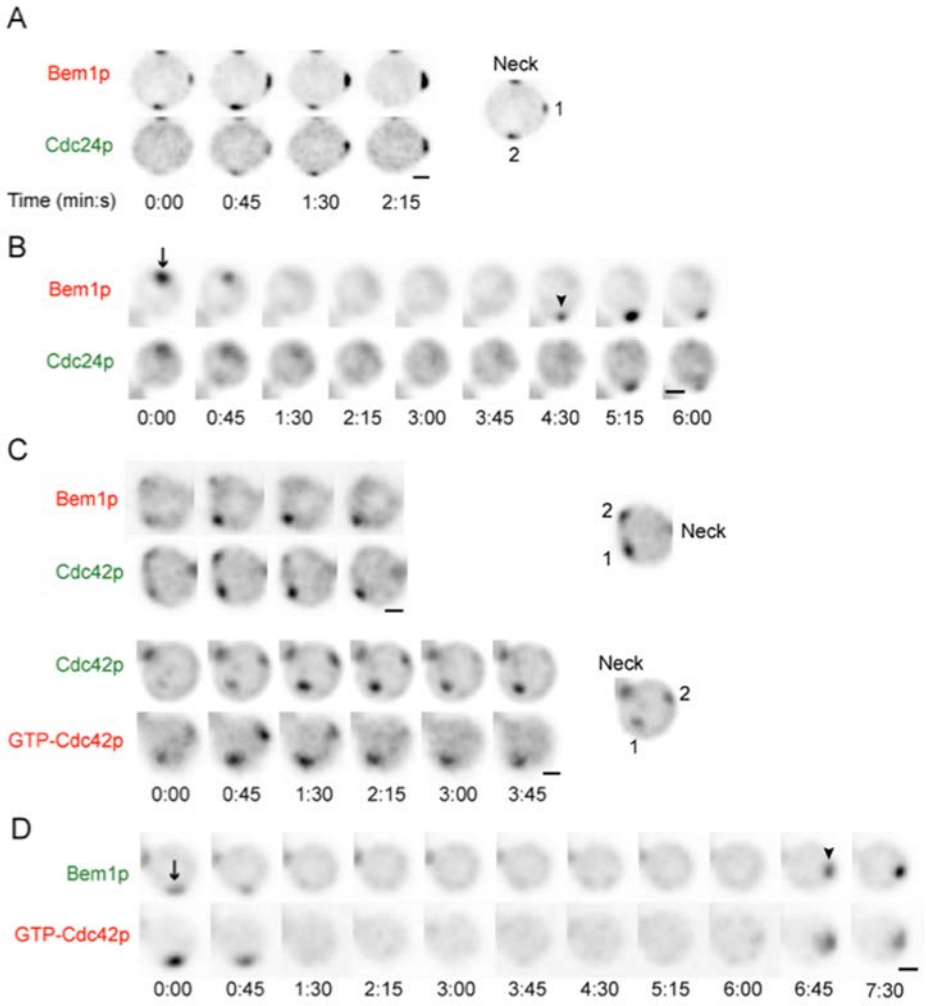

Figure. 3.4. Competition and relocation of Cdc42p and Cdc24p
A) Bem1p-tdTomato and Cdc24p-GFP co-cluster and compete (clusters are numbered in the key at right). B) Bem1p-tdTomato and Cdc24p-GFP clusters relocate in parallel. C) Bem1p-tdTomato and GFP-Cdc42p (upper panels), and GFP-Cdc42p and PBD-tdTomato (lower panels) co-cluster and compete. D) Bem1p-GFP and GTP-Cdc42p clusters relocate in parallel. **The experiments were designed and conducted by Audrey Howell, Chi-Fang Wu and Dr. Daniel Lew.**

behavior (Fig. 3.3B, C). However, these probes were somewhat toxic, and the incidence of cells displaying high-amplitude oscillations was reduced when these probes were expressed. Cells displaying multiple competing clusters, as well as relocation, were also

observed (Fig. 3.4), indicating that the core polarity regulators all concentrate, disperse, and reappear in concert.

3.3 The cause of oscillatory polarization

What causes the oscillation? In the original model of yeast polarity establishment (Goryachev and Pokhilko, 2008), the only inhibition for a polarity spot to grow comes from the depletion of free Bem1-GEF molecules. This inhibition is sufficient to keep the polarity spot in a local area, but could not dismantle the already accumulated proteins. The damped intensity of a polarity spot suggests that an additional negative regulation become strong enough to inhibit the polarity machinery after the polarity spot growing to a certain size.

3.3.1 Cytoskeletal factors

One candidate for this negative inhibition is the cytoskeleton. Polarization of GTP-Cdc42p induces the actin polymerization. F-actin cables mediate exocytosis, which could transport vesicles either diluting GTP-Cdc42p concentrations at polarity spot (Layton et al., 2011) or containing GAPs to inactivate polarized GTP-Cdc42p (Knaus et al., 2007; Ozbudak et al., 2005). Endocytosis of Cdc42p or other factors could also disrupt polarity (Irazoqui et al., 2005; Yamamoto et al., 2010). These negative inhibitory mechanisms would disappear if no polarity spots exist and thus not affect re-establishing the polarity. Moreover, actin patches (labeled with Abp1-mCherry) clustered at the polarization site about 90s following initial clustering of Bem1p (Howell et al., 2009), which coincided with Bem1p-GFP dispersal (Fig 3.5A and B). Thus actin polarization is temporally correlated with dispersal of polarity factors. However, disrupting actin

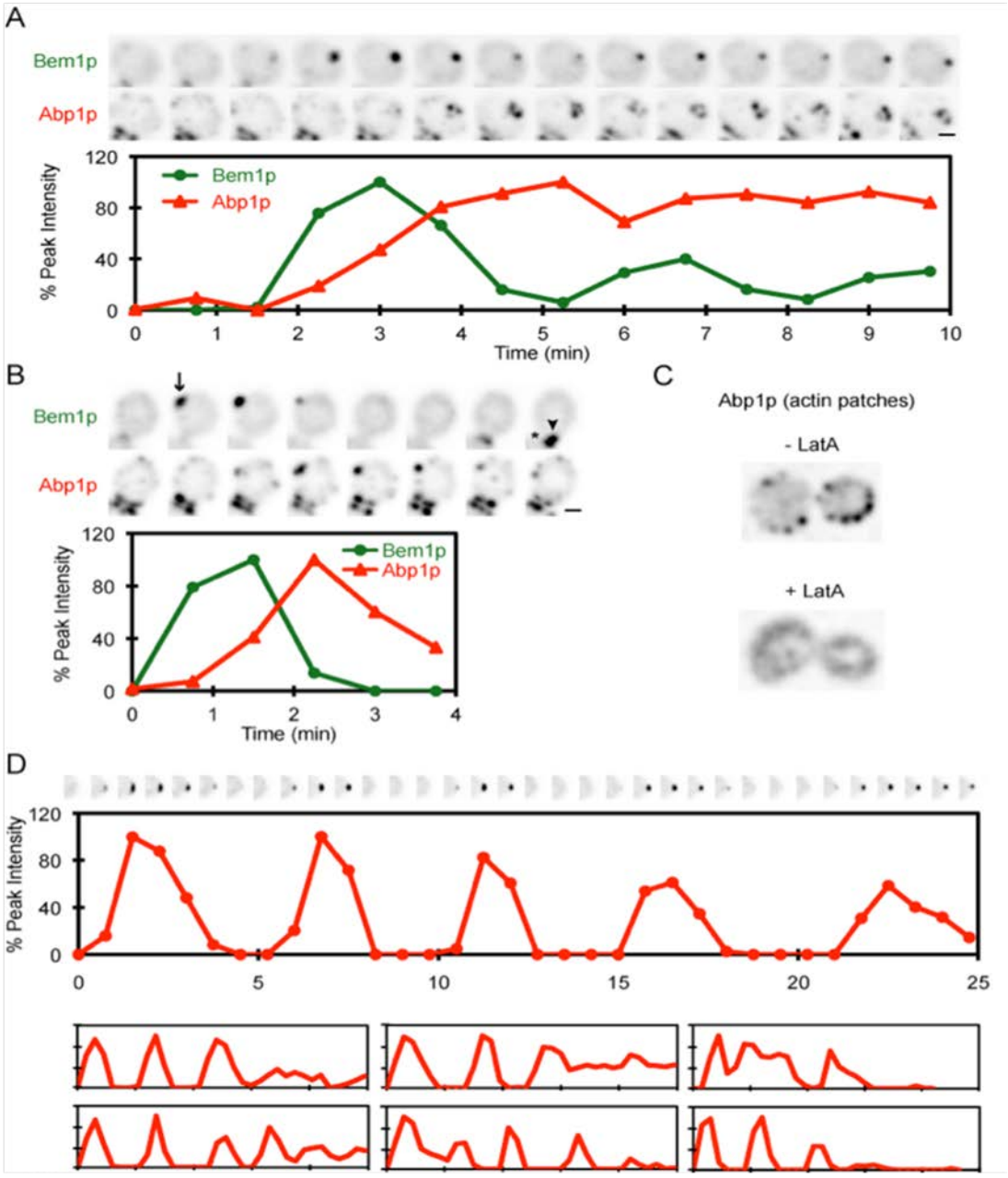

Figure. 3.5. Actin and septin polarization are delayed relative to Bem1p
A) Abp1p-mCherry (marker for actin patches) clusters as Bem1p-GFP begins to disperse. B) Abp1p-mCherry clustering follows Bem1p-GFP clustering and remains at the old site as Bem1p relocates (arrowhead). Asterisk: old mother-bud neck. C) Actin patches are dispersed upon Lat A treatment. D) Bem1p-GFP oscillation persists in Lat A. Top: Cropped images of the polarization site at 45 s intervals. Middle: Quantification of Bem1p-GFP. Bottom: Six other examples of oscillation in Lat A. **The experiments were designed and conducted by Audrey Howell, Chi-Fang Wu and Dr. Daniel Lew.**

polymerization by Latrunculin A (LatA) did not stop the polarity spot oscillating or

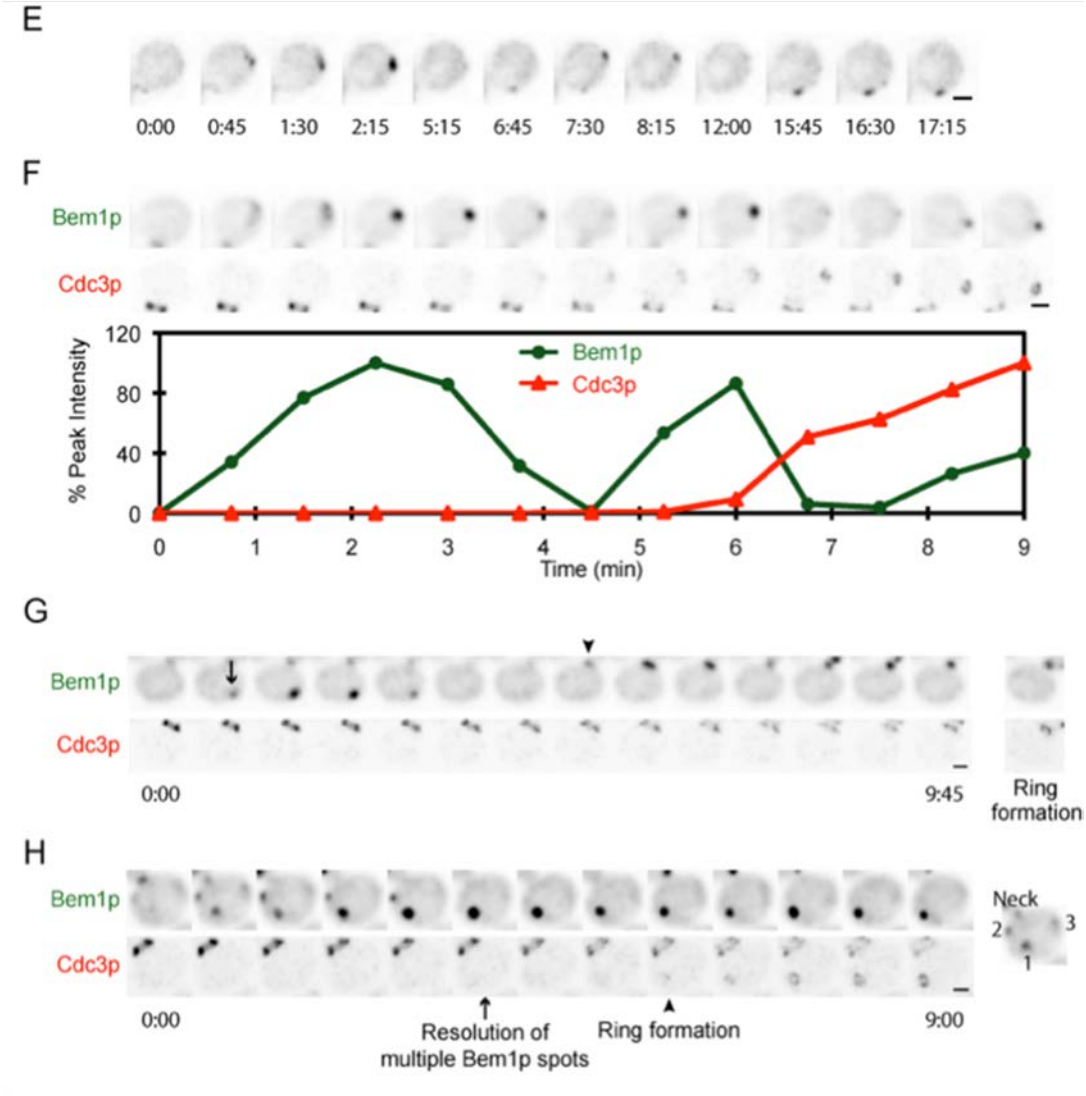

Figure. 3.5. Actin and septin polarization are delayed relative to Bem1p

E) Relocation of Bem1p-GFP in Lat A-treated cell. F) Septin (Cdc3p-mCherry) recruitment begins after initial oscillation of Bem1p-GFP. G) Septin recruitment begins after relocation of Bem1p. No septin signal appears at the position of the first Bem1p-GFP cluster (arrow). Bem1p-GFP then relocates to the site of the old mother-bud neck (arrowhead) where remaining septins from cytokinesis obscure the new ring. G) Septin recruitment (arrowhead) begins after resolution of multi-cluster Bem1p intermediate (arrow). **The experiments were designed and conducted by Audrey Howell, Chi-Fang Wu and Dr. Daniel Lew.**

relocation (Fig 3.5C, D and E). In particular, the number of oscillations before budding was increased in LatA treated cells (Fig 3.5D). These data indicated that the oscillatory dynamics was damped but not caused by F-actin.

The septin Cdc3p-mCherry accumulated ~4 min after the initial clustering of Bem1p-GFP (Fig. 3.5F), after relocation or competition had occurred (Fig 3.5G and H). Therefore, the septin ring is too late to disperse the polarized cluster of Bem1p-GFP.

3.3.2 Possible negative feedback in the pathway

Oscillatory dynamics in most biological processes is related with negative feedback (Novak and Tyson, 2008). Since the cytoskeleton has been ruled out, the cause of observed oscillation is more likely to be negative feedback from the biochemical reactions in the pathway.

As mentioned before, only substrate depletion is not enough to dismantle an established polarity spot. We proposed two mechanisms to account for the negative feedback that builds up slower than the clustering and that fades away when polarization disappears (Fig. 3.6A). One mechanism is increasing the negative regulation, e.g. GTP hydrolysis, through active GTP-Cdc42p; the other is disrupting the positive feedback of clustering. Both mechanisms are based on the original model described by Goryachev and Pokhilko (Goryachev and Pokhilko, 2008) (Fig. 3.6A, model 1).

In the first mechanism, we assumed that polarized GTP-Cdc42p could activate nearby GAPs via PAK mediated phosphorylation (Fig. 3.6A, model 2). The phosphorylated GAPs are more efficient at hydrolyzing GTP-Cdc42p, and then destroy the polarization. The clustering starts again when activated GAPs return to the normal state. We also assumed that the dephosphorylation of GAPs is slow, which sets a time delay between the dispersal and rebuild of a polarity spot.

The second mechanism assumed that the GTP-Cdc42p could modify the Bem1p-Cdc24p complex, probably by phosphorylation, reducing the binding affinity of the modified Bem1p-GEF with GTP-Cdc42p (Fig. 3.6A, model 3). The positive feedback is disrupted because that the GTP-Cdc42p-Bem1p-Cdc24p complex breaks down after modification and that modified Bem1p complex accumulates in the cytoplasm, unable

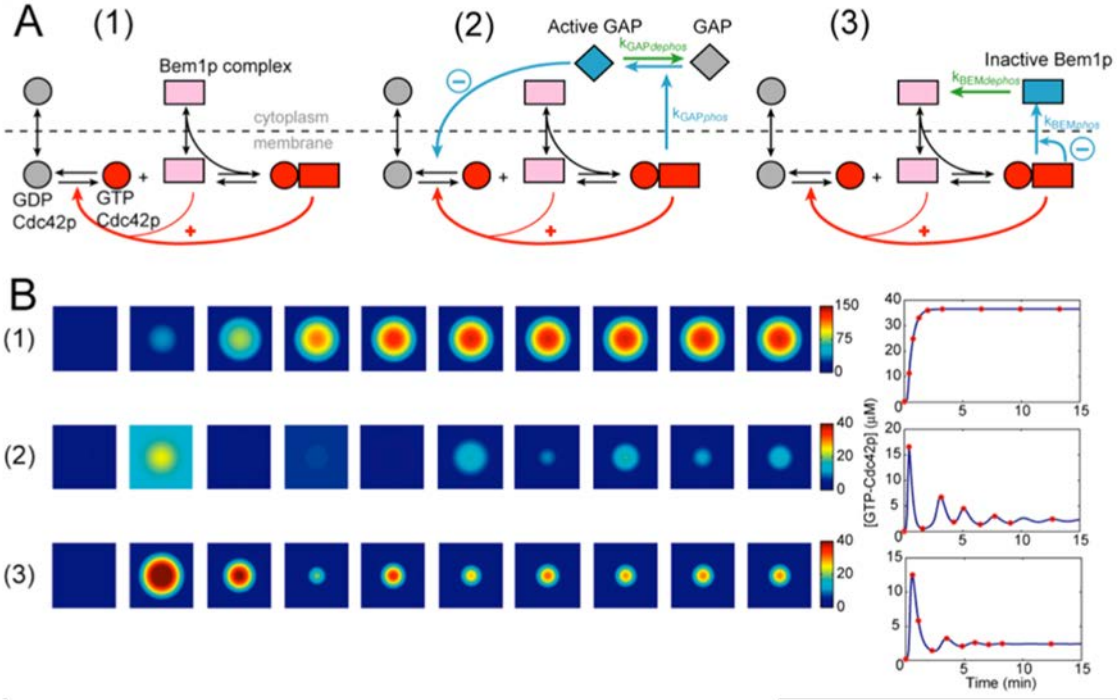

Figure 3.6 Negative feedback can cause oscillatory polarization

A) Diagram of the starting model (1) and two variants incorporating negative feedback via a Cdc42p-directed GAP (2) or the Bem1p complex (3). Positive feedback is indicated by red arrows, and negative feedback by blue arrows. We assume that GTP-Cdc42p/PAK activates the GAP (blue GAP, model 2) or inactivates Bem1p complex components (blue complex, model 3). Phosphorylated proteins are then dephosphorylated in the cytoplasm (green arrows). B) Snapshots from simulations. The square represents a 2D plasma membrane and color indicates GTP-Cdc42p concentration. Snapshots are indicated by red dots in the tracings to the right, plotting GTP-Cdc42p concentration with time.

to rebind with GTP-Cdc42p. The accumulation starts again when most modified Bem1p-GEF molecules are reset to the unmodified state. Similar to the first mechanism, the removal of this modification, probably dephosphorylation, is a slow process so as to

setup a time delay. The detailed assumptions and model equations are listed in the Appendix II.

Both mechanisms were able to reproduce the damped oscillatory polarization observed in experiments with proper parameters (Fig. 3.6B). The spatiotemporal dynamics was fine-tuned by the timing between the dissipating and the next round clustering. Generally, the positive feedback took off before the negative feedback settled at its minimal strength, resulting in a damped second peak (Fig. 3.12, point 8 and 9). Strong oscillations only occurred in a very narrow parameter space. When the clustering initiated immediately after the dissipation reaching its minimal strength, both models predicted approximately sustained oscillation on the entire membrane (Fig. 3.12, point 6 and 7). In this regime, addition of noise to the models converted the spatially uniform oscillation into sustained oscillatory clustering, and clusters were able to compete and relocate (Fig. 3.12, point 6 and 7). Thus, addition of negative feedback and noise can in principle reproduce all of the polarity dynamics observed in cells.

3.4 More important properties than oscillation

The dynamics predicted by two negative feedback mechanisms are comparable in periodicity, polarization kinetics and cluster relocating. So what are unique properties due to negative feedback? Knowing this, we could understand why the yeast polarization pathway has built-in negative feedback.

3.4.1 Robustness

One distinct property we proposed for the polarization pathway with negative feedback is robustness to changes in the key polarity proteins abundance. If the amount

of critical players, such as Cdc42p and Bem1p complex, increases several folds, then the stronger positive feedback would tend to activate more GTP-Cdc42p; meanwhile, the negative feedback would increase correspondingly and restrict the growth of polarity clusters. In contrast, if there is no negative feedback, the substrate-depletion could hardly keep the polarization local, causing activation over the entire membrane.

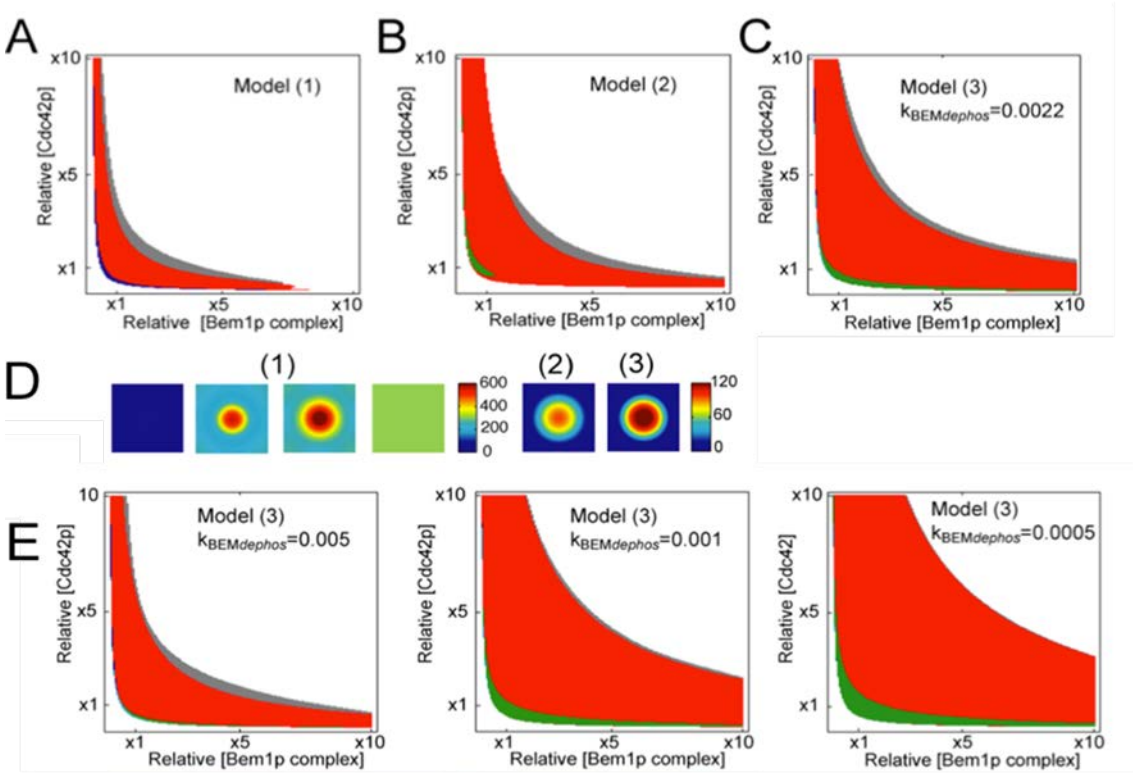

Figure 3.7 Negative feedback improves robustness of the polarity model

A) Behavior of model 1 at varying polarity protein concentration. Red, Turing-unstable region: polarization occurs in response to small perturbation. Blue/grey, regions where both uniform and polarized states are stable: polarization occurs in response to large perturbation. White: no polarized steady state. B) Behavior of model 2. Green, sustained oscillations. C) Behavior of model 3. D) Snapshots of simulations with 6.5-fold higher starting concentration of Cdc42p: model 1 spreads GTP-Cdc42p uniformly (left), whereas models 2 and 3 yield a polarized steady state (right). E) Robustness, indicated by the area of red regions, varies with changing negative-feedback parameters. Model 3 was analyzed at the indicated values of $k_{BEMdephos}$.

By varying the total amount of Cdc42p and Bem1p complex, we compared the robustness in three models (model 1, with the positive feedback only and model 2 and 3.3, two with different negative feedback mechanisms). We tested whether the model could polarize, and if so, how many active GTP-Cdc42p molecules stay in the polarity site. For model 1, polarization only occurred in a small region in the parameter space of Cdc42 and Bem1-GEF complex concentration (Fig 3.7A). Outside this area, the active Cdc42 distributed all over the membrane as the concentration of Cdc42 or Bem1 complex increased (Fig 3.7D). Consistent with our prediction, the parameter space for polarization in model 2 and 3 were expanded with the additional negative feedback, and cells were still be able to polarize with 6.5-fold increase in total Cdc42p (Fig 3.7 B, C and D). Therefore, the negative feedback makes the polarization pathway more robust to changes in component concentrations.

The degree of increased robustness depends on the negative feedback parameters. For example, decreasing the Bem1p complex dephosphorylation rate in model 3 progressively broadened the polarization region (Fig 3.7E, red region). Similar predictions were obtained for model 2, which has a different molecular mechanism for negative feedback. Therefore, it is likely that negative feedback would improve robustness regardless of the precise feedback mechanism.

Is polarity establishment indeed robust to increases in Cdc42p or Bem1p-complex concentration? To test this, we used a galactose-regulated promoter to overexpress either Cdc42p or its GEF, Cdc24p. Because cells are more photosensitive when grown in galactose, we used an artificial Gal4p transcription factor fused to the estrogen receptor ligand-binding domain to allow induction by β-estradiol in glucose-containing media

(Takahashi and Pryciak, 2008). Filming of Bem1p-GFP revealed robust polarization even following ~7-fold overexpression of Cdc42p or Cdc24p (Fig 3.8A-C). A previous

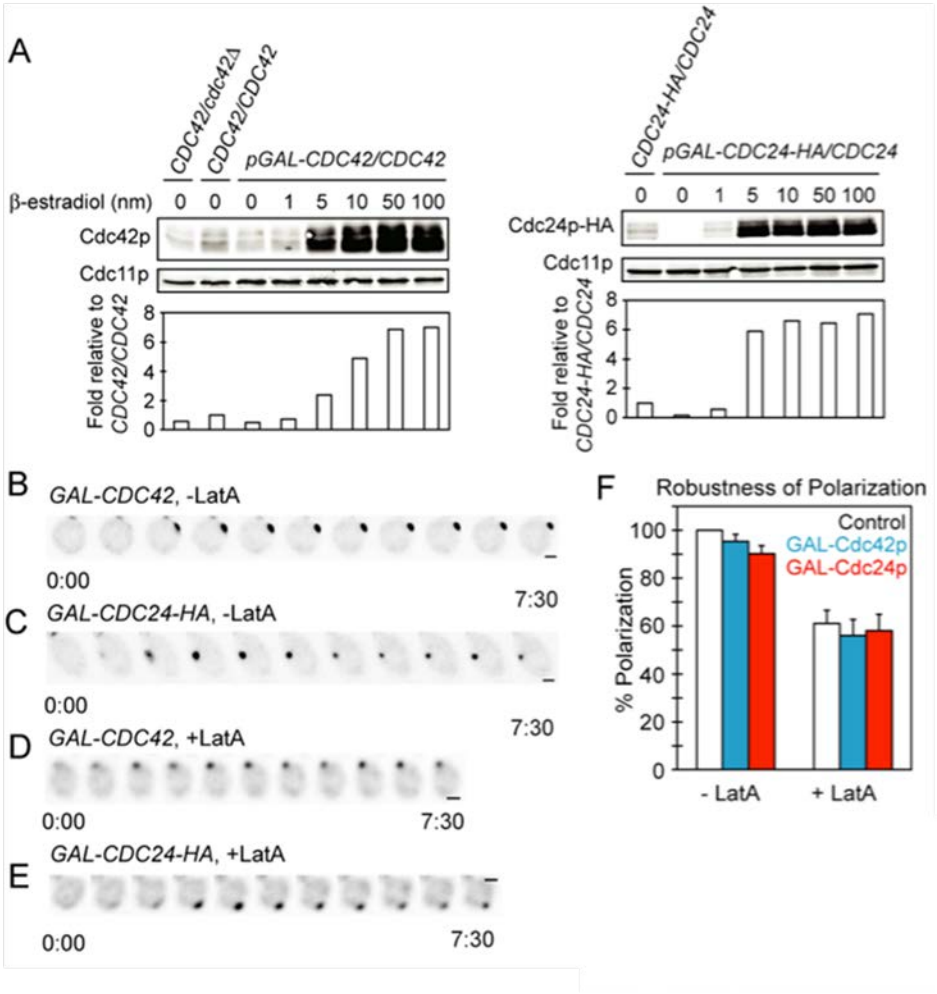

Figure 3.8 Polarization is robust to overexpression of Cdc42p or Cdc24p

A) Western blot and quantification of Cdc42p (left) and Cdc24p-HA (right) in response to β-estradiol (subsequent panels used 100 nM). B-E) Bem1p-GFP polarization in representative cells overexpressing Cdc42p (B, D) or Cdc24p-HA (C, E), in the absence (B, C) or presence (D, E) of Lat A. F) Quantification of the % of cells that polarized in control (white), Cdc42p-overexpressing (blue), or Cdc24p-HA-overexpressing (red) strains in the absence or presence of Lat A (mean +/- SEM). **The experiments were designed and conducted by Audrey Howell, Chi-Fang Wu and Dr. Daniel Lew.**

study reported that Cdc42p overexpression blocked polarity establishment in cells lacking F-actin (Altschuler et al., 2008), but we found that polarization occurred with comparable efficiency whether or not cells overexpressed Cdc42p or Cdc24p, even in cells treated

with Lat A (Fig 3.8D-F). Thus, polarity establishment in yeast is robust to increases in Cdc42p or Cdc24p concentration, beyond the capacity of a positive-feedback-only mechanism.

How much Bem1p-Cdc24p complex has been raised due to the overexpression of Cdc24p? If Cdc24p is not the limiting factor in the Bem1p-Cdc24p complex, its overexpression cannot represent the increase in the Bem1p-Cdc24p complex, and thus cannot prove that the polarity circuit is robust to increases in Bem1p complex. To circumvent potential controls on complex assembly, we expressed a Cdc24p-Cla4p (PAK) fusion protein that mimics the full complex (Kozubowski et al., 2008) (Fig 3.9A). As previously reported, this fusion protein cause hyperpolarized growth in budded cells (Kozubowski et al., 2008), but here we focus on its effects on initial polarity establishment. Time-lapse analysis indicated that a majority of cells expressing the fusion could polarize, but some cells were delayed in polarization and a few cells underwent a full cell cycle without establishing polarity (Fig 3.9B). Overexpression of Cdc42p together with the Cdc24p-Cla4p fusion blocked polarity establishment in a large majority of cells, leading to the accumulation of large, unbudded, multinucleate cells (Fig 3.9C and D). The simplest interpretation of these findings is that combined expression of Cdc42p and a fusion protein that mimics the full Bem1p complex drives the system into the “white” regime of parameter space, where GTP-Cdc42p spreads throughout the cortex.

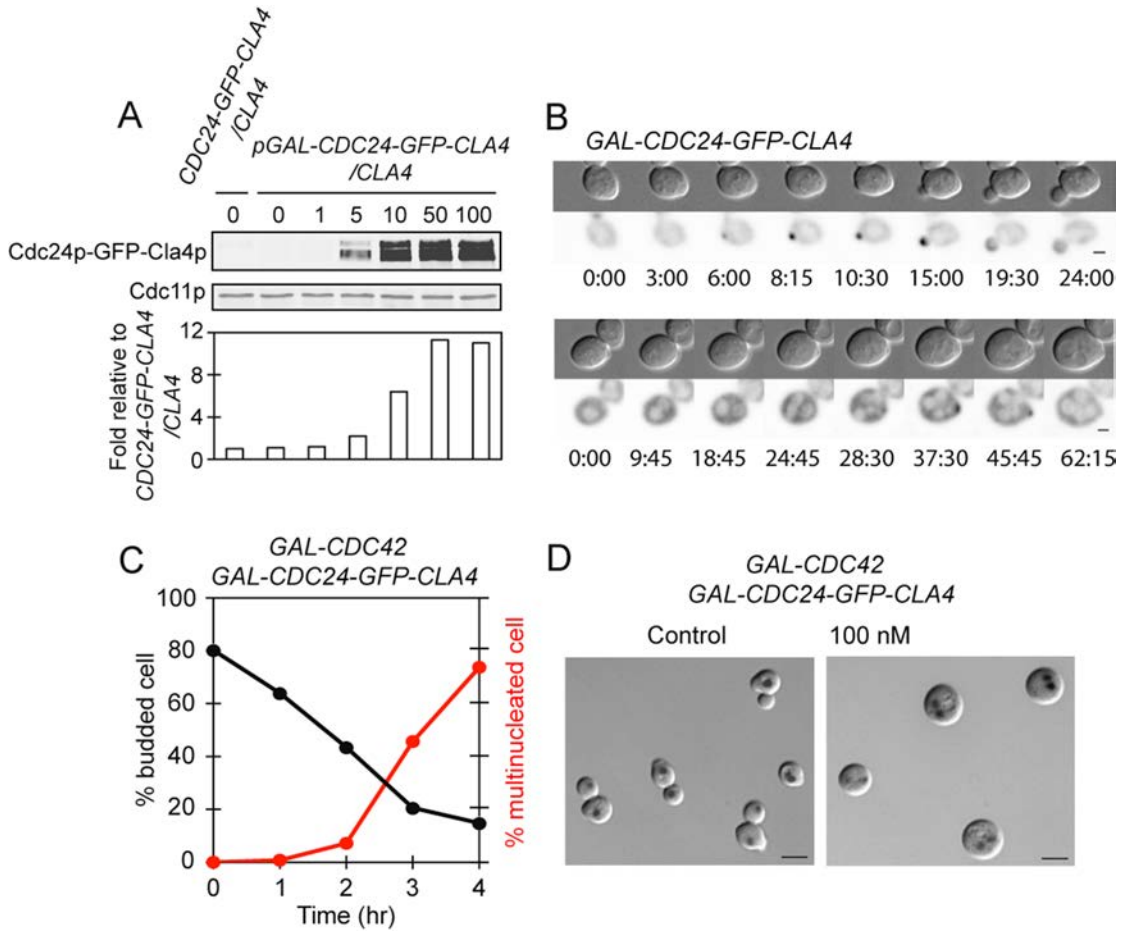

Figure 3.9 Polarization is robust to overexpression of Cdc24p-Cla4p fusion
A) Western blot and quantification of Cdc24p-GFP-Cla4p fusion. 1x indicates expression level from the *CDC24* promoter. B) Cdc24p-GFP-Cla4p distribution in cells that do (top) or do not (bottom) polarize. Nuclei and vacuoles exclude the protein and appear light. C) Plot of budding index and frequency of multinucleate cells following induction of both Cdc24p-GFP-Cla4p and Cdc42p. D) Representative cells from (C) after 0 h (left) or 4 h (right) of induction. Overlay of inverted DAPI staining and DIC images. Bar, 5 μm. **The experiments were designed and conducted by Audrey Howell, Chi-Fang Wu and Dr. Daniel Lew.**

3.4.2 Fast competition between two polarity spots

Since competition between multiple clusters is a common phenomenon before budding, how does negative feedback affect competition between clusters? As mentioned in 1.3.3, one issue with a model based on typical Turing mechanism is slow resolution for

competing polarity spots. One would expect that if the concentrations of polarity components were increased, it would take longer time to determine the winner spot (Howell et al., 2009). In contrast, for a polarization pathway with negative feedback, the dispersal increases in concert with the positive feedback, which could accelerate the competition between unequal clusters or keep the competition unaffected by changes in the protein abundance.

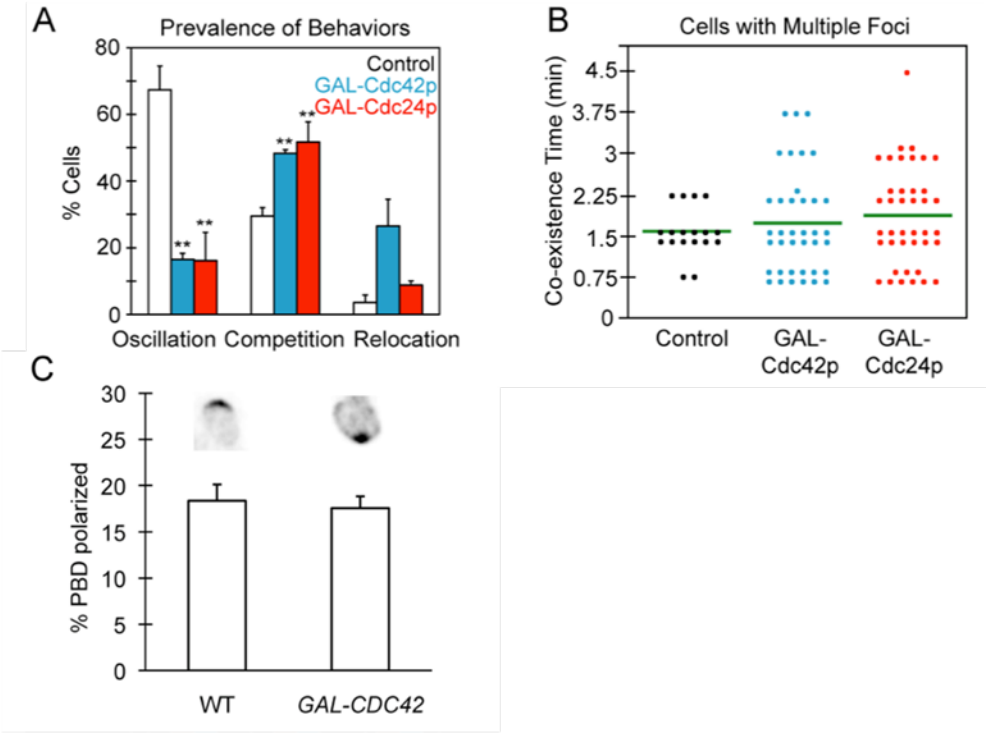

Figure 3.10 Competition between clusters remains fast after overexpressing Cdc42p and Cdc24p

A) Prevalence of high-amplitude oscillation (left), multi-cluster intermediates (middle), and relocating clusters (right) in control (white), Cdc42p-overexpressing (blue), or Cdc24p-HA-overexpressing (red) strains (mean +/- SEM). ** significant difference between overexpressors and controls ($p<0.01$ by two-tailed t-test). B) Quantification of the time taken to resolve multi-cluster intermediates. C) The fraction of the GTP-Cdc42p-binding probe (mean +/- SEM) that is polarized in late G1 cells is similar with (right) or without (left) Cdc42p overexpression. Representative images shown at top. **The experiments were designed and conducted by Audrey Howell, Chi-Fang Wu and Dr. Daniel Lew.**

So how fast is competition between multiple polarity clusters after overexpressing Cdc42p and Cdc24p? The kinetics of polarization and damping oscillation were altered by overexpression of Cdc42p and Cdc24p, and the frequency of cluster relocation was increased in cells overexpressing Cdc42p (Fig 3.10A). However, the resolution to a single cluster still occurred rapidly (Fig 3.10B), consistent with the prediction of negative feedback model.

How did cells maintain fast competition after overexpressing Cdc42p or Cdc24p? We measured the amount of GTP-Cdc42p in the polarized clusters using the fluorescent GTP-Cdc42p-binding reporter (Tong et al., 2007). Despite considerable cell-to-cell variation in the total amount of reporter in the cell, a relatively consistent ~19% of the probe was polarized in late-G1 wild-type cells (Fig 3.10C). Strikingly, a similar fraction of the probe was polarized in cells overexpressing Cdc42p (Fig 3.10C), suggesting that cells are able to buffer the polarized cluster against Cdc42p overexpression, explaining why competition remained rapid.

To assess how models with and without negative feedback would impact competition times, we simulated the competition duration between two clusters with an initial 55:45 ratio of GTP-Cdc42 content for model 1 (no negative feedback) and model 3 (with negative feedback). The profile of two unequal clusters was obtained in two steps. First, we evolved a symmetric two-peak solution to steady state; then we adjusted the profile of GTP-Cdc42p from a 50:50 ratio to 55:45 (total Cdc42p was unchanged) and used this profile as the initial condition for competition simulation. Without negative feedback, the steady state level of GTP-Cdc42 increased as the concentrations of Cdc42 or Bem1 complex rose, which caused competition duration extended proportionally (Fig

3.11A and B). Whereas, the negative feedback buffered the steady state level of GTP-Cdc42 for high levels of Cdc42 or Bem1 complex, and thus the competition between two

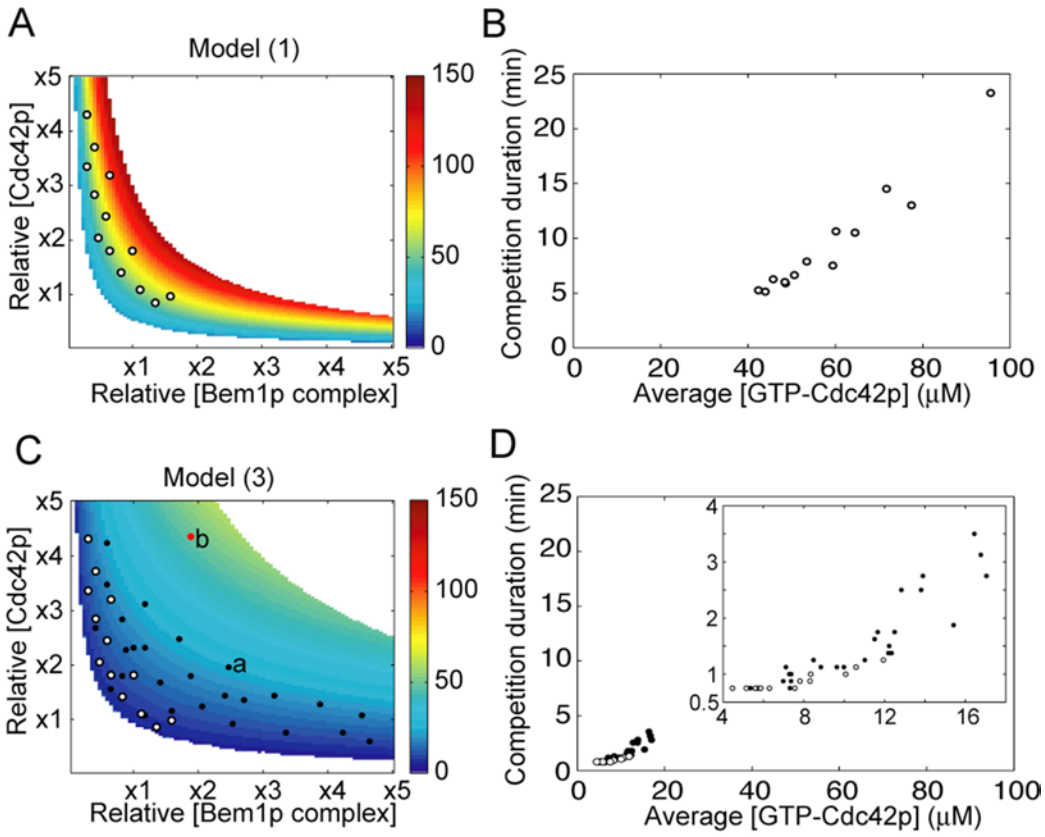

Figure 3.11 Negative feedback buffers the accumulation of GTP-Cdc42p and can accelerate or abolish competition between clusters

A) Steady-state GTP-Cdc42p levels in model 1 change rapidly as component concentrations are increased. Color indicates steady-state GTP-Cdc42p concentration (calculated from the spatially uniform situation) in the parameter space displaying Turing instability. Circles indicate points used for simulations in B. B) Correlation between GTP-Cdc42p concentration and the time taken to resolve competition. Each symbol represents a simulation, at parameter values from the circles in A, of the competition between two unequal clusters (ratio 55:45), plotting the time taken to resolve competition (Y axis) and the average GTP-Cdc42p concentration of the 2-cluster starting state (X axis). C) Steady-state GTP-Cdc42p levels in model 3 are buffered against increases in component concentrations. Symbols indicate points used for simulations in D. White circles are as in A, whereas black symbols are in the expanded polarity region. Symbols labeled "a" and "b" indicate parameters used in E. D) Negative feedback maintains rapid competition in a broad range of parameter space. Kinetics of competition between clusters (as in B), at parameter values indicated in C. Inset: expanded view of lower-left quadrant.

clusters remained rapid (Fig 3.11C and D), as observed experimentally (Fig 3.10B and

C). Therefore, another advantage of having negative feedback in the polarization pathway is to maintain fast competition time even though the amount of proteins involved in positive feedback is increased.

The buffering effect of negative feedback significantly reduces competition times in the majority of the simulations, producing coexistence times consistent with the experimental observations (Fig 3.11D). However, this is not universally true in all parts of the parameter space. Whereas in model 1 a larger cluster always (eventually) out-

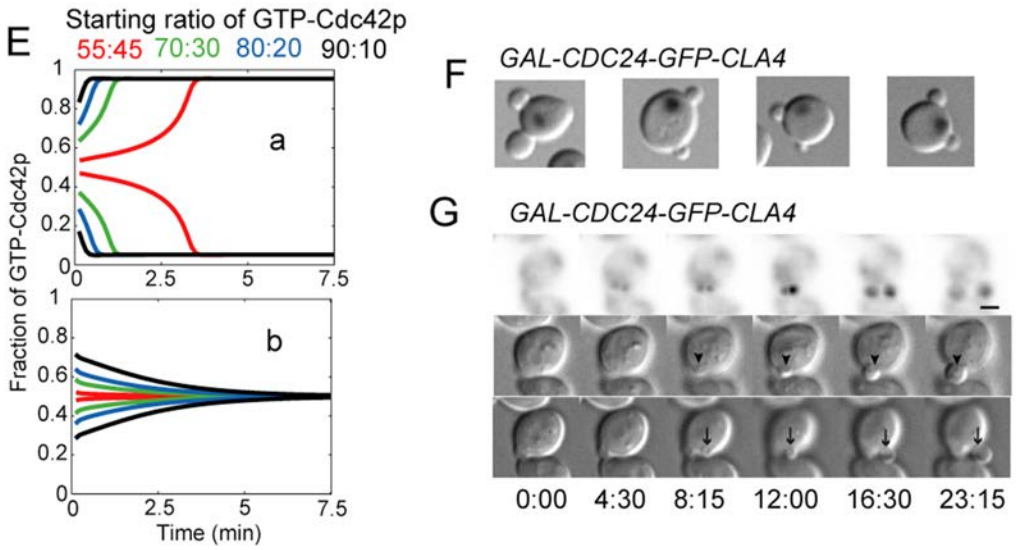

Figure 3.12 Negative feedback buffers the accumulation of GTP-Cdc42p and can accelerate or abolish competition between clusters
E) Negative feedback can lead to equalization of clusters instead of competition between clusters, at high levels of polarity proteins. Simulations as described in B, with the indicated starting ratios between unequal clusters, using the parameter values from the symbols labeled "a" and "b" in C. F) Examples of 2-budded cells from a culture induced to express Cdc24p-Cla4p fusion for 4 h. Overlay of inverted DAPI staining and DIC images. G) Simultaneous growth of two buds (arrow and arrowhead in different DIC z-planes) and polarization of Cdc24p-Cla4p fusion to both buds. **The experiments were designed and conducted by Audrey Howell, Chi-Fang Wu and Dr. Daniel Lew.**

competed and eliminated a smaller cluster, in model 3, competition failed at sufficiently high Cdc42p and Bem1p complex concentrations. With these parameters, the clusters equalized rather than competing (Fig 3.11E), and simulations evolved to a stable steady

state containing two equal clusters (Fig S3). In cells, this would presumably lead to formation of two buds. Interestingly, occasional cells (~1%) expressing the Cdc24p-Cla4p fusion did make two buds (Fig 3.11F). Two-budded cells polarized stably to two sites (Fig 3.11G), though sometimes one site disappeared, leading to the development of unequal-sized buds.

3.5 Fine-tuned spatiotemporal dynamics of polarization

3.5.1 Possible dynamics in the parameter space of total Cdc42p and total Bem1p

We examined the dynamical behavior of models (1), (2) and (3) in the plane of total Cdc42p and Bem1p complex concentration. The range of concentration is chosen from 0 to 10-fold of the concentrations from previous studies (Table 3).

There are 8 types of spatiotemporal behavior based on the number of fixed points and their stability with respect to spatial perturbations (Fig. 3.12):

(i) Monostable: The spatially homogeneous steady state has only one fixed point and it is stable to all perturbations (white regions in all bifurcation diagrams: point 4, Fig. 3.12A).

(ii) Bistable 1: Three spatially homogeneous fixed points exist, two of which are stable (blue regions in Fig. 3.7A and B, Fig 3.12). The fixed point with low GTP-Cdc42p is stable to all local perturbations, whereas the fixed point with high GTP-Cdc42p is stable to spatially homogenous perturbations but Turing unstable to spatial perturbations (point 1, Fig. 3.12A).

(iii) Turing unstable: Only one fixed point exists, which is stable with regard to spatially uniform perturbations, but unstable given any small spatial perturbation (red regions in all bifurcation diagrams: points 2, 8, and 9, Fig. 3.12). In this region away

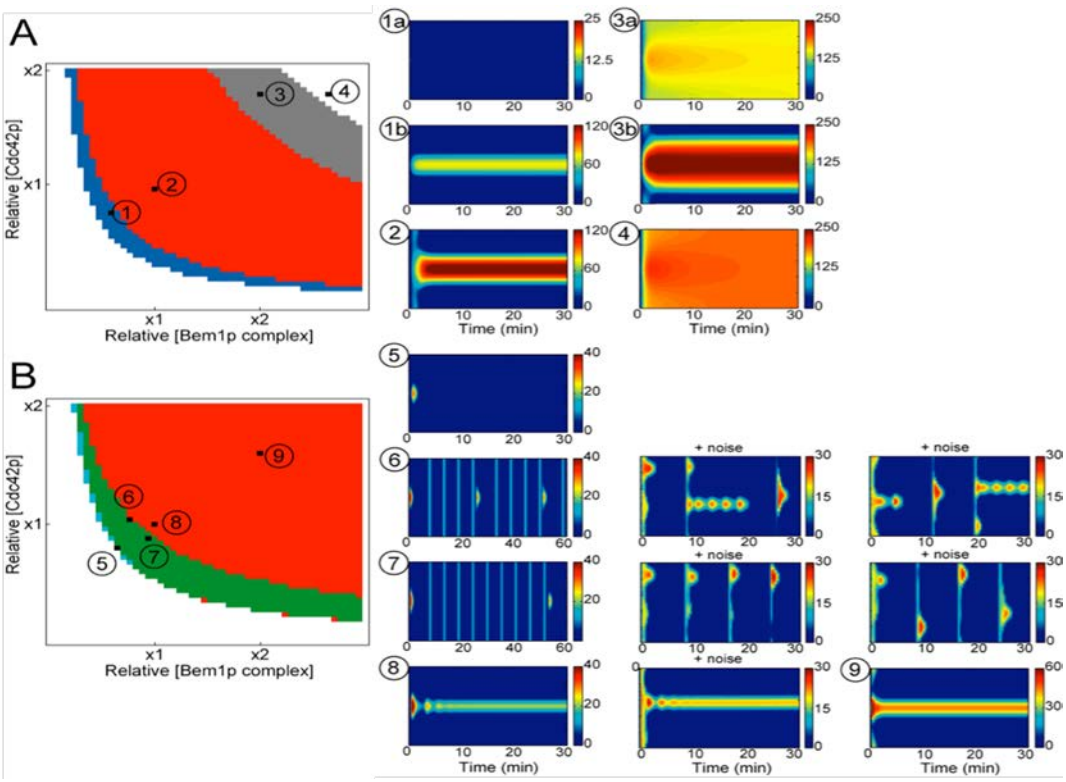

Figure 3.12. Spatiotemporal dynamics in different parts of model parameter space
A) Behaviors of Model (1). Left: expanded view of the lower-left quadrant of the [Cdc42]-[Bem1-complex] bifurcation diagram: numbered symbols indicate positions simulated at right. (#1) Bistable 1: depending on the strength of the perturbation, an initial perturbation decays back to the uniform steady state (1a) or grows to reach a polarized steady state (1b). [Cdc42] = 4 μM, [Bem1-complex]= 0.01 μM. (#2) Turing Unstable: a small perturbation always polarizes. [Cdc42] = 5 μM, [Bem1-complex]= 0.017 μM. (#3) Subcritical Turing Unstable: depending on the strength of the perturbation, an initial perturbation decays to a uniform steady state (3a) or grows to reach a polarized steady state (3b). [Cdc42] = 9 μM, [Bem1-complex]= 0.034 μM. (#4) Monostable: any initial perturbation leads to a uniform steady state. [Cdc42] = 9 μM, [Bem1-complex]= 0.045 μM. B) Behaviors of Model (3). Left: expanded view of the lower-left quadrant of the [Cdc42]-[Bem1 complex] bifurcation diagram: numbered symbols indicate positions simulated at right. (#5) Excitable: a perturbation initially grows but then decays back to the uniform steady state. [Cdc42]= 4 μM, [Bem1-complex]= 0.011 μM. (#6) Mixed Turing and Hopf Unstable: sustained oscillations, switching between uniform and localized patterns. [Cdc42]= 5.2 μM, [Bem1-complex]= 0.0135 μM. (#7) Mixed Turing and Hopf Unstable (closer to the center of the region): similar to (#6), but less frequent localized patterns are interspersed with more frequent spatially uniform oscillations. [Cdc42] = 4.4 μM, [Bem1-complex]= 0.016 μM. (#8) Turing Unstable (close to Hopf-Turing unstable region): damped oscillation on the way to a polarized steady state. [Cdc42]= 5 μM, [Bem1-complex]= 0.01775 μM. (#9) Turing Unstable (far from Hopf-Turing unstable region): a polarized state with little oscillation. [Cdc42] = 8 μM, [Bem1-complex]= 0.034 μM. Although not depicted, simulations in the Subcritical Turing Unstable (grey) and Monostable (white) regions of Model (3) behave similarly to the corresponding regions of Model (1).

from the lower boundary, all models produce stable polarity site(s), which do not oscillate. The majority of polarization occurs in this region.

At the lower boundary of this region, close to the region with mixed Turing and Hopf instability (see below), models (2) and (3) show damped oscillatory polarization (point 8, Fig. 3.12B). This type of behavior does not occur in model (1), and occurs in a relatively narrow region of parameter space for models (2) and (3).

(iv) Subcritical Turing unstable: For this case, only one uniform stable fixed point exists. However, it becomes unstable under sufficiently large spatial perturbations (the gray regions in all bifurcation diagrams: point 3, Fig. 3.12A) (Cross and Hohenberg, 1993; Rovinsky and Menzinger, 1992).

(v) Excitable: Three spatially homogeneous fixed points exist, but only one is stable. The stable fixed point is an unstable spiral: large enough homogenous perturbations can excite transient homogeneous increases in the level of active Cdc42p (cyan regions in Fig. 3.7B, C, E and Fig 3.12B). Spatially localized perturbations can induce transient polarization (point 5, Fig. 3.12B) (Hecht et al., 2010; Xiong et al., 2010). Excitable behavior does not occur in model (1).

(vi) Turing and Hopf unstable: Only one fixed point exists, which is Hopf unstable and Turing unstable (green regions in Fig. 3.7B, C, E and Fig 3.12B) (De Wit et al., 1996). This type of behavior does not occur in model (1).

Using appropriate parameter values, there are two other types of behavior:

(vii) Bistable 0: Three fixed points exist for spatially homogeneous concentrations, two of which are stable with different levels of active Cdc42p. Both fixed points are stable to spatial perturbations.

(viii) Hopf unstable: Only one fixed point exists that is unstable to all perturbations. The long-term behavior of the system is uniform oscillations of active Cdc42p.

The stability of (i), (ii), (iii), (v), (vii) and (viii) were assessed by numerically determining the steady state and calculating the eigenvalues for the linearized reaction equations in 1D. The Turing instability in (iii) and (vi) was determined by linear stability analysis (Murray, 2003). The boundary of region (iv) was determined by numerical simulations. All three models show similar behaviors in planes of other parameter values.

3.5.2 Interaction between spatial range and duration of negative feedback

In model 2 and 3, relocation of the polarity cluster only occurred in the presence of noise. Intuitively, if the negative feedback strongly inhibits clustering in a local region and lasts for enough long time, then the new cluster would prefer a position away from the current polarity site as far as possible. That is, the spatial range of the negative feedback would alter the relocation property.

To test this, we modified model 2 by introducing intermediate reactions between GTP-Cdc42p-Bem1p complex and the GAPs (model 2b). GTP-Cdc42p-Bem1p complex leads to the membrane bind of a cytoplasmic species X, and then the membrane bound Xm activates cytoplasmic GAPs, increasing the hydrolysis rate of GTP-Cdc42p. The spatial distribution of effective GAPs in model 2b was steeper compared with that in model 2 (Fig 3.13A). Consistent with our hypothesis, given the more localized negative feedback, polarity cluster preferred a different position in the next round of polarization (Fig 3.13B). The spatial distribution works together with how fast the local negative

feedback disappears to control the relocation. For example, with fast deactivation of the active GAPs, polarization re-established at the center (Fig 3.13B) even though the GAP was more concentrated at the center (Fig 3.13A). The localized inhibition that lasts for enough long time makes relocation possible if the noise is too weak to shift polarization site. The local inhibition might come from a membrane bound effector of GTP-Cdc42p.

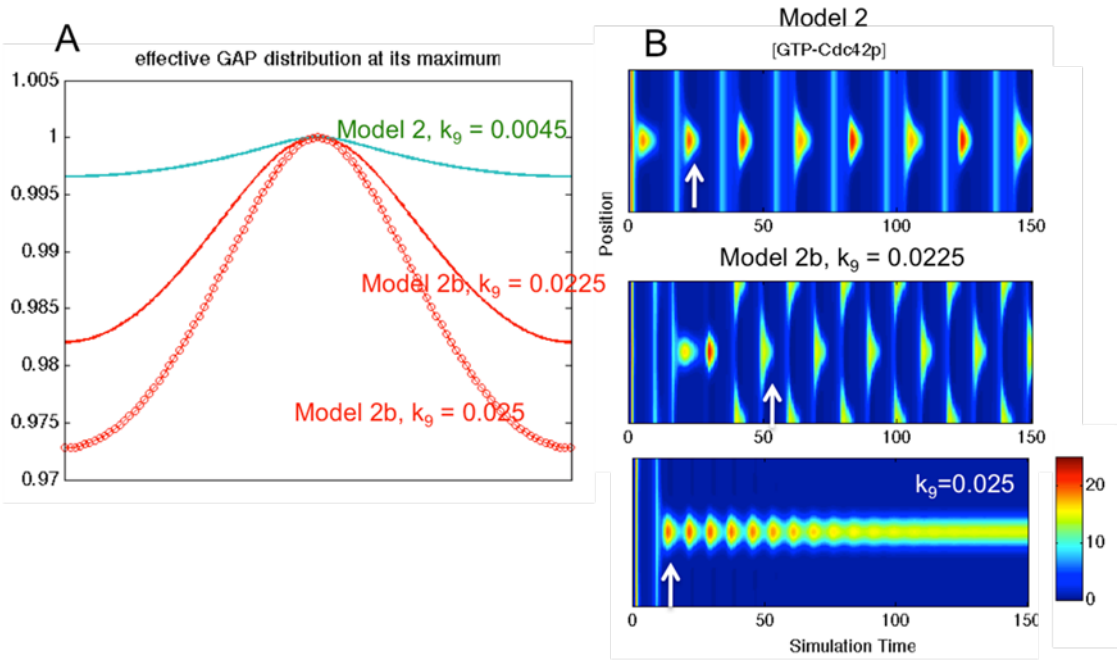

Figure 3.13 Relocation is regulated by the spatial range and duration of negative feedback

A) The spatial profile of effective GAPs when its concentration reaches maximum due to GTP-Cdc42p accumulation (pointed by the white arrows). All of them are normalized to their maximum value. Green line, red line and red open circles are corresponding to the top, middle and bottom kymographs on the right, respectively. B) The kymograph of GTP-Cdc42p for GAP profile on the left. Top: model 2; Middle: model 2b with intermediate reactions to keep GAP more concentrated at the polarity site; Bottom: model 2b, but the deactivation of GAP is fast.

Interestingly, the strong polarity coupled with slow recovery of negative feedback can induce global inhibition that temporally kills the polarization. For example, the alternating polarization and several rounds of uniform oscillation occurred in model 2 and 3(points 6 and 7, Fig. 3.12B). A spatially localized perturbation initiates formation of a

polarized distribution of GTP-Cdc42p. The polarized GTP-Cdc42p caused a strong induction of negative feedback, which then destabilized polarization. As GTP-Cdc42p levels fall, the negative feedback is reduced, but remains sufficient to repress polarization. Thus, GTP-Cdc42p increases uniformly and then oscillates. Since these rounds of uniform activation of Cdc42p could not trigger strong inhibition, the strength of negative feedback dropped below threshold during this phase, enabling the positive feedback to accumulate GTP-Cdc42 locally. As the polarization of GTP-Cdc42p induced the negative feedback again, another round of uniform oscillations started.

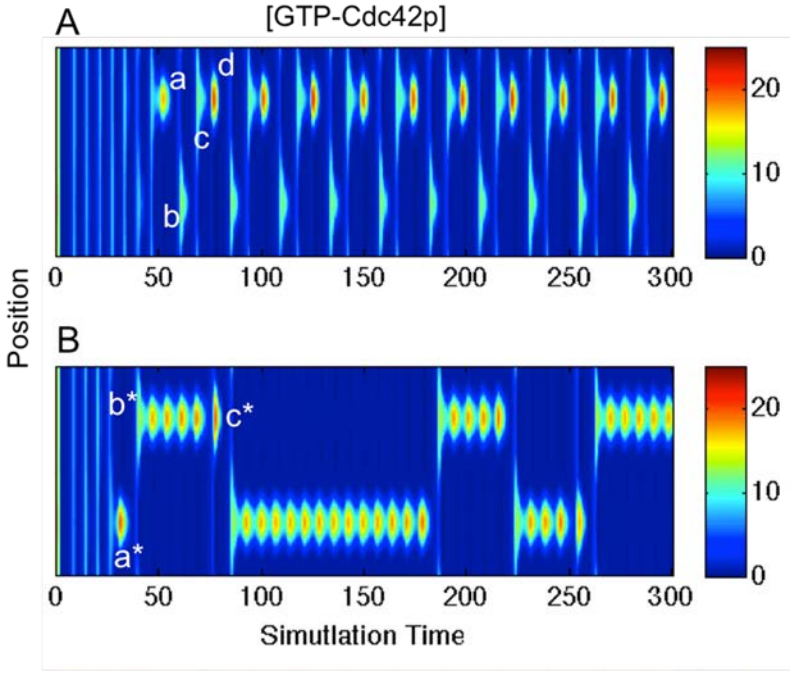

Figure 3.14 The strength of positive feedback and the duration of negative feedback control the period and relocation of clustering.
A) The kymograph of GTP-Cdc42p, model 2b with k_9=0.0175. B) The kymograph of GTP-Cdc42p of model 2b, k_9=0.02.

The strength of polarization and the duration of negative feedback work in concert to control the period and position of oscillatory clustering, creating delicate

spatiotemporal dynamics. For example, in model 2b (Fig 3.14A), the difference in the intensity of clusters a, b and c caused three types of re-clustering. Positive feedback accumulated an intermediate amount of GTP-Cdc42p in cluster a, which in turn created negative feedback of sufficient strength to relocate the next cluster. Due to this strong inhibition, cluster b did not accumulate as much GTP-Cdc42p as cluster a, and therefore the inhibition from cluster b was weaker than that in cluster a, but enough to shift polarization to the opposite position, forming cluster c. The inhibitory effect reduced to the minimum in the dampening phase of cluster c, giving cluster d the chance to form at the same site as cluster c and to accumulate the largest amount of GTP-Cdc42p. Then cluster d affected future clusters in a similar way as cluster a. By reducing the duration of the negative feedback through increasing the deactivation rate of GAPs (Fig 3.14B), the cluster b* could not inhibit polarization at the same site, forming a series clustering at the same position. The mismatched timing between the building up of positive feedback and the decay of negative feedback gradually accumulated more GTP-Cdc42p in new clusters, leading to the brightest spot (cluster c*) at the end of this series. Cluster c* reset the strong inhibition, and started a new round of brightening clusters with increasing intensity followed by a sudden relocation.

3.6 General remarks

3.6.1 Negative feedback during polarity establishment

Filming of symmetry-breaking polarization at high resolution under low-light imaging conditions revealed that clusters of polarity factors congregated rapidly (often within 45 s) and then unexpectedly dispersed, subsequently reforming and dispersing up

to three more times before stabilizing (Fig 3.2 and 3.3). Oscillatory clustering was not predicted by existing models of polarity establishment and suggests that positive-feedback-mediated initial polarization is rapidly antagonized by a negative feedback loop. Mathematical modeling suggested that adding a negative feedback loop to a previous model for polarity establishment could lead to oscillatory clustering, and different negative feedback mechanisms (acting either through a Cdc42p-directed GAP or GEF) produced qualitatively similar results (Fig 3.6). Noise-containing simulations exhibited rapid multi-cluster competition followed by oscillation, as well as relocation of clusters. Thus, in appropriate parameter regimes, models that incorporate negative feedback and noise in addition to the previously modeled positive feedback can reproduce all of the polarity dynamics that we observed in cells. The mechanism of negative feedback in cells remains to be determined.

Negative-feedback-containing models produced either sustained or intrinsically damped oscillations, depending on the concentrations of polarity factors (Fig 3.12). However, in cells the oscillatory clustering was always damped. Damping was correlated with the arrival of septins at the polarization site, and was delayed in the absence of F-actin (a condition that delays septin assembly) (Fig 3.5). Thus, it may be that the core polarity machinery has the capacity to produce sustained oscillatory clustering, and that downstream cytoskeletal factors act to dampen the oscillation.

It is unclear what advantage could stem from high-amplitude oscillations in polarity factor concentration. When cells were exposed to more stressful imaging conditions, they exhibited lower-amplitude oscillation, as did cells filmed without the photo-protective hydroxyurea pretreatment (Howell et al., 2009). Given the sensitivity of

the behavior to filming conditions and component concentrations, it seems unlikely that such oscillation is important in and of itself. Instead, oscillation may have arisen as a byproduct of homeostatic negative feedback. As discussed below, adding negative feedback to the polarity model improves its robustness. Interestingly, robustness could be further improved by lowering the rates at which a negative-feedback-modified GEF or GAP returned to its baseline state. Lowering those rates introduces a delay (as the modified GEF/GAP accumulates rapidly but takes time to return to its basal state), which, in turn, favors oscillatory behavior. Thus, oscillations might arise as a byproduct of a negative-feedback loop that is present to optimize robustness.

Oscillations in polarized growth (after polarity establishment) have been particularly well-studied in plants (Hepler et al., 2001), where the oscillatory growth of pollen tubes is thought to involve interlinked positive and negative feedback loops (Yan et al., 2009). It is unclear whether oscillation per se is advantageous, as pollen tubes switch from prolonged continuous growth to oscillatory growth without overt changes in overall elongation speed or morphology (Feijo et al., 2001). Thus, the use of negative feedback to promote homeostasis or robustness may lead in some cases to the appearance of unselected oscillations, which may or may not be beneficial in themselves (Cheong and Levchenko, 2010; Feijo et al., 2001).

3.6.2 Robustness of polarity establishment

Although capable of polarity establishment, a model that only contains positive feedback is fragile in that increasing concentrations of polarity factors quickly overwhelm the system, causing GTP-Cdc42p to spread all over the cortex. A benefit of

negative feedback is improved robustness to such changes: the negative feedback prevents runaway accumulation of GTP-Cdc42p, so the model retains the ability to polarize over a much wider range of polarity factor concentrations. Similar robustness predictions were obtained regardless of the modeled feedback mechanism or specific parameters (Figs 3.7 and S2). Thus, consistent with the well-known homeostatic influence of negative feedback in well-mixed systems (Brandman and Meyer, 2008), negative feedback confers improved robustness regardless of the precise feedback mechanism.

The modeling results prompted us to test whether yeast polarization is indeed robust to increased levels of polarity factors, and we found that cells polarized just as efficiently when Cdc42p or Cdc24p were overexpressed. The robustness we observed is consistent with older reports that Cdc42p overexpression is tolerated by yeast (Ziman and Johnson, 1994), but contrary to the conclusion from a recent study suggesting that Cdc42p overexpression blocked polarity establishment in cells lacking F-actin.The apparent difference between those results and ours may stem from the fact that we overproduced wild-type Cdc42p whereas they used a myc-GFP-Cdc42p construct that is nonfunctional and potentially toxic when overexpressed. In addition, they used the same probe to score polarization, potentially making it difficult to detect a polarized signal above the high unpolarized background in overexpressing cells. We conclude that the yeast polarity establishment circuit is robust to variation in polarity factor concentration, even in cells lacking F-actin, and that robustness is likely to be conferred by negative feedback.

3.6.3 Competition between polarity clusters

A long-standing question in the polarity field concerns why cells develop one and only one "front". We recently suggested that in yeast, positive feedback could give rise to more than one polarity cluster, but then the clusters would compete with each other so that a single winner would emerge (Howell et al., 2009). Alternatively, the small absolute numbers of a limiting polarity factor might make it unlikely that more than one cluster could develop (Altschuler et al., 2008). With previous filming protocols it was difficult to detect the multi-cluster intermediates predicted by the competition hypothesis (Howell et al., 2009), but with improved imaging we now document such intermediates in ~25% of cells breaking symmetry. Upon overexpression of Cdc24p or Cdc42p, the incidence of detectable multi-cluster intermediates increased to ~50%. These numbers represent a lower bound for the real incidence of such intermediates, as technical issues may prevent us from detecting small and/or short-lived clusters. Thus, multi-cluster intermediates are very frequent and competition between polarity clusters is critical to prevent the development of more than one front.

Multi-cluster intermediates were short-lived, resolving to a single cluster in 2 min (on average). Surprisingly, competition was similarly rapid even in cells overexpressing Cdc24p or Cdc42p, which is inconsistent with the prediction from the positive-feedback-only model that cells with more polarity factors should build clusters containing more polarity proteins. As such clusters take longer to dismantle during competition, it should take considerably longer to resolve the competition in favor of a single winner. Negative feedback can buffer the accumulation of polarity factors in clusters, so that overexpression need not significantly increase the amount of Cdc42p or other factors in

the cluster, explaining why competition did not take much longer in overexpressing cells than in controls. Thus, a second benefit of negative feedback in the polarity circuit is that when more than one cluster forms, competition between clusters is more rapid.

An unexpected prediction from mathematical modeling of polarity circuits with negative feedback was that at high Cdc42p and Bem1p complex concentration, competition should fail to resolve polarity clusters. Instead, two clusters would tend to equalize so that each contains the same amount of polarity proteins. Presumably, this would lead to the formation of two buds in yeast, perhaps explaining the observation of occasional two-budded cells in strains overexpressing Bem1p (Howell et al., 2009)or a Cdc24p-Cla4p fusion (Fig 3.11). However, such cells might also arise if competition were drastically slowed (Howell et al., 2009)

We speculate that the cluster equalization predicted by the model at high polarity factor levels may be relevant to a currently unexplained behavior called tip-splitting or apical branching that occurs in a variety of fungi (Harris, 2008; Riquelme and Bartnicki-Garcia, 2004) and is particularly well-studied in *Ashbya gossypii* (Knechtle et al., 2003). *A. gossypii* is an evolutionarily close relative of *S. cerevisiae* that uses related proteins to establish and maintain polarity, but grows as a multinucleate filamentous fungus (Dietrich et al., 2004). As the hypha grows, accumulating more polarity factors, tip growth accelerates until at some point the polarization cluster expands (Schmitz et al., 2006) and splits into two equal clusters, generating a Y-shaped branch in the hypha. At the time of tip splitting, there are two neighboring polarity clusters that clearly do not compete with each other. A polarity circuit with built-in negative feedback may explain

how these cells can sustain two equal clusters in close proximity, and why they do not do so until a large size has been reached.

In conclusion, the oscillatory polarization observed under improved filming conditions reveals that the yeast polarity establishment circuit contains negative feedback. Modeling suggests that negative feedback confers robustness as well as the capacity for rapid competition between polarity clusters. The presence of negative feedback also raises the possibility that in appropriate circumstances, the system could be tuned to produce several polarity axes, which may be required for generating the more complex morphologies observed in other eukaryotes.

CHAPTER 4.

Kinetics of ste5 membrane recruitment

4.1 Overview

When pheromone molecules bind to the G protein coupled receptors and activate G proteins, the information about the spatial distribution and concentration of pheromone molecules is transmitted to the downstream MAPK pathway and polarization pathway. The scaffold protein, Ste5, serves like a hub of input information. It interacts with active G proteins through its membrane recruitment and connects the MAPK pathway with polarization pathway through interaction with the PAK, Ste20, in the polarity spot (Fig. 1.2B).

Ste5 is recruited to membrane in a polarized way after pheromone treatment through binding with free Gβγ, and its spatial distribution follows the distribution of free Gβγ (Pryciak and Huntress, 1998). Moreover, the spatial localization of Ste5 affects the responses of the MAPK cascade to increasing levels of stimulus (Takahashi and Pryciak, 2008). The dose response curve of MAPK cascade is graded if Ste5 is recruited to membrane, but switch-like if Ste5 remains in cytoplasm (Takahashi and Pryciak, 2008).

Ste5 also couples the polarization pathway with the MAPK kinase activation cascade to initiate a pheromone response. Ste5 membrane recruitment by Gβγ facilitated the interaction between Ste20 and Ste5 membrane recruitment by Gβγ

facilitated the interaction between Ste20 and Ste11, amplified the Ste11 activation (Lamson et al., 2006). Besides, polarization of Cdc42 leads to asymmetry distribution of phosphatidylinositol 4,5-bisphosphate (PtdIns(4,5)P2), which in turn stabilizes Ste5 on the membrane (Garrenton et al., 2010).

Since Ste5 links information flow from both polarization pathway and MAPK cascade, it is interesting to understand how information from pheromone is encoded in the spatial and temporal dynamics of Ste5, and how Ste5 spatiotemporal dynamics affects the downstream signaling. These two questions motivated us to tracking the Ste5 membrane binding and dissociation in single cells with different spatial profiles of input pheromone.

4.2 Kinetics of Ste5 membrane recruitment

To obtain the kinetics of Ste5 membrane recruitment during elongation, we filmed cells expressing Ste5-$(GFP)_3$ in a uniform pheromone concentration of 75nM. Cells were synchronized at M phase with 15mg/ml Nocodazole before pheromone treatment to remove the variability due to cell cycle. By tracking single cells, the kinetics of Ste5 polarization and membrane recruitment were obtained (Fig. 4.1).

Without pheromone, Ste5-$(GFP)_3$ stayed in cytosol and was slightly concentrated in the nucleus (Fig. 4.1, top row). Unlike Bem1-GFP polarization in response to pheromone, there were more fluctuations in Ste5 polarization (Fig. 4.2A). Before visible polarization of Ste5, speckles of Ste5 were recruited to membrane, spreading along the cell perimeter (Fig 4.1, middle row). Stable polarization started about 10~15min after switching on pheromone, but disappeared occasionally and with large cell-to-cell

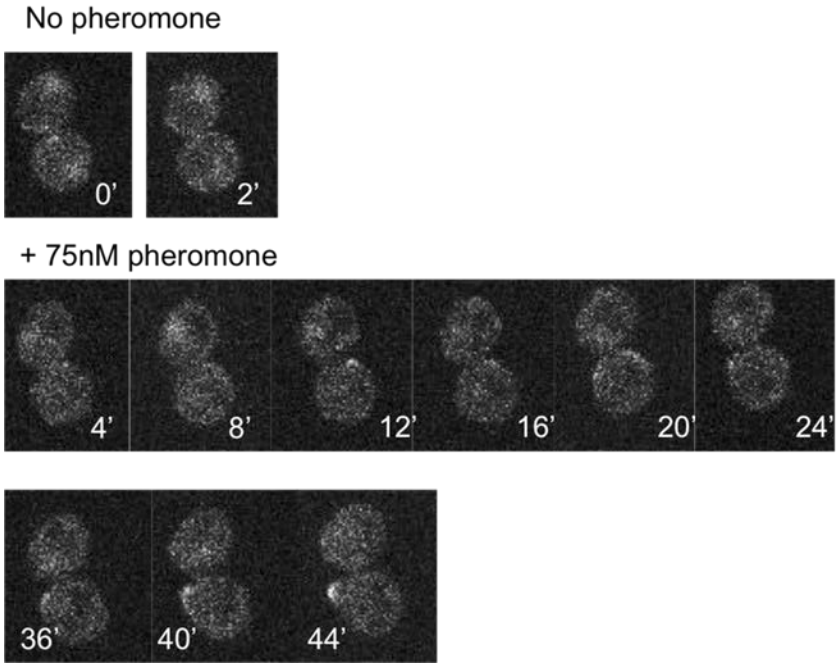

Figure. 4.1 Time lapse imaging of Ste5-$(GFP)_3$ in 75 nM uniform pheromone
Top row: Ste5-$(GFP)_3$ distribution at zero pheromone (imaging every 2min). Middle row: imaging Ste5-$(GFP)_3$ every 4 min immediately after adding pheromone. Bottom row: after 36 min in pheromone.

variability (Fig 4.1, middle row and Fig. 4.2A). To quantify the change in the intensity of Ste5 polarization, we calculated the ratio between mean Ste5 intensity in brightest region and in the other ("dark") area on membrane (Fig 4.2A and B). Averaging over 23 cells, Ste5 polarization occurred about 8 min after given pheromone (Fig. 4.2B). Different from Ste5 polarization in a small area on membrane, its membrane recruitment, measured as the ratio of mean Ste5-$(GFP)_3$ intensity on membrane to that in cytosol, rose immediately after pheromone treatment (Fig 4.2 C).

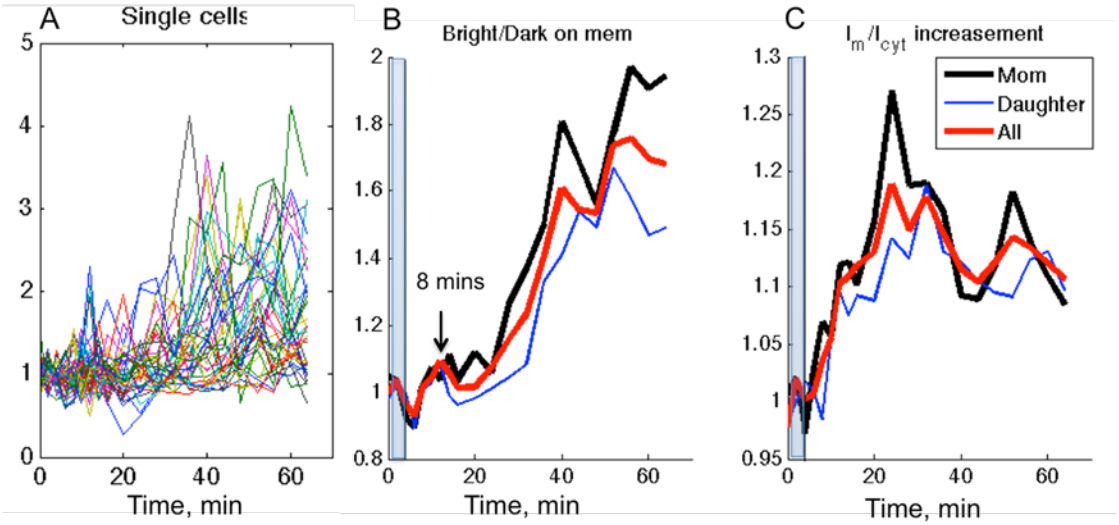

Figure. 4.2 Quantify the kinetics of Ste5 membrane recruitment

A) Single cell trajectories of the ratio between mean intensity of Ste5-$(GFP)_3$ in polarized clusters and that in non-polarized region on membrane. Each trajectory is normalized by the mean of this ratio in the cell before given pheromone. B) The mean of single cell trajectories in A). C) The ratio of mean Ste5-$(GFP)_3$ intensity on membrane intensity to that in cytosol. Pheromone was given after 4 min. The shaded region indicates the dynamics of Ste5-$(GFP)_3$ in the absence of pheromone, and images were taken every 4 min after given pheromone. The plots in B) and C) averaged 23 cells, grouped into mothers and daughters.

4.3 General remarks and future plans

The measured kinetics of Ste5 membrane binding was slower than expected. Although we do not have the time course of MAPK activation in synchronized cells, the phosphorylation of Fus3 and Kss1 rise up within 10 min of pheromone treatment in asynchronized cells (Hao et al., 2008). The phosphorylation rate is consistent with the change in the ratio of average Ste5 in membrane to cytosol, but earlier than the stable polarization of Ste5. This leads us to wonder how the activation of downstream kinases changes when Ste5 polarizes, since the polarization of Ste5 would concentrate its binding partners and amplify signaling through the kinase cascade.

Similar results were obtained by imaging cells every 2 min upon pheromone

treatment (polarization occurred after 11min of pheromone treatment.). However, we need to measure the photobleaching rate of the Ste5-$(GFP)_3$ and correct our quantification by the photobleaching rate.

Imaging Ste5 membrane binding and dissociation provides a straightforward way to see how stimulus is transmitted at the level of Ste5. To test the effect of absolute pheromone levels on Ste5 membrane recruitment, we will film Ste5-$(GFP)_3$ at 150nM uniform pheromone and compare the kinetics of Ste5 membrane binding with that in 75nM uniform pheromone. The dissociation kinetics will also be measured by switching uniform pheromone off. Aligning the on/off membrane kinetics of Ste5 with the activation/deactivation profile of kinases in the cascade and changes in transcription would provide clues about the regulation between layers in the MAPK signaling pathway (Yu et al., 2008).

Filming cells in pheromone gradients would also address how Ste5 dynamics encodes the spatial distribution of pheromone. By comparing dynamics of Ste5 in cells in the middle of 0~150nM (0~300nM) gradient with those in 75nM (150nM) uniform pheromone, we would know whether steeper pheromone gradients accelerate Ste5 polarization. Since Ste5 polarization requires Gβγ binding, we could infer the distribution of free Gβγ in different pheromone gradients, bypassing the difficulty of probing active G-proteins. Moreover, we could map the spatial dynamics of receptors (Ste2), Ste5 and polarity machinery (e.g. Bem1) to determine how spatial information is processed at different levels of signal transduction and to understand how cells sense the pheromone gradients.

CHAPTER 5.

Conclusions and future directions

Our initial goal was to quantitatively understand polarization and gradient sensing and thereby find crucial network motifs that regulate the spatial and temporal dynamics in these processes. Starting from this, we now understood one aspect of gradient tracking: why degrading pheromone from α cells improves the mating with α cells. By combining microfluidic experiments and computational simulation, our results showed that through secreting the protease Bar1, yeast cells actively modify the pheromone gradients around them, which enables them to avoid unproductive same-sex contact, to expand searching area, to amplify pheromone gradients and to reduce competition for a common mating partner. Multiple benefits come from a simple strategy: altering the spatial dynamics of input signal. Similar strategy might be applied in other systems. For instance, *Dictyostelium* cells secrete phosphodiesterase PdsA to degrade the cAMP for better sensing cAMP gradients (Garcia et al., 2009).

By considering the physical limit of gradient sensing, Endres and Wingreen analytically showed that secreting proteases such as Bar1 or Pds enables cells to measure gradients with higher accuracy (Endres and Wingreen, 2008). In the presence of proteases, a cell behaves as an absorbing sphere, which infers gradients from the absorbed surface particle density (e.g. density of pheromone molecules degraded

by Bar1) over time. The previously "observed" particles have already been degraded and would never be re-measured (Endres and Wingreen, 2008). In this way, the perfectly absorbing sphere has higher accuracy in gradient detection than a monitoring sphere (or a cell that does not secrete proteases), which infers gradient from positions of freely diffusing particles inside a cell and "observed" particles are likely to be re-measured.

However, how cells track the shallow gradients is still puzzling. First, whether the realistic gradients sensed by yeast cells are beyond the theoretical uncertainty of measured gradient is unknown. The detailed ligand-receptor binding and downstream signaling events, such as receptor dimerization, might further increase measurement uncertainty. Second, the duration of gradient sensing is long enough (on the timescale of hours) that yeast cells probably combine other processes, e.g. vesicle trafficking and receptor endocytosis, to overcome the low accuracy gradient detection.

One attractive mechanism to estimate external gradient is time averaging of liganded receptors and free Gβγ. When cells polarize in the range of pheromone gradients optimal for gradient sensing, the polarization occurs rapidly but wanders along the cell perimeter. The speed of patch moving is regulated by vesicles traveling along actin cables, because these vesicles dilute the concentration of polarity factors in the polar patch and shift the centroid of polar patch by inserting more membrane to the polarity site (Johnson et al., 2012; Layton et al., 2011). The high mobility enables the polar patch to interact with receptors and free Gβγ over the entire membrane. If one region on the cell membrane accumulates more liganded receptors and free Gβγ molecules, the polar patch would move slowly in that region due to the interaction between Gβγ and Cdc24. As the polarity patch would spend more time at the region with high levels of liganded receptors

and free Gβγ, the growth would be biased toward that region and align with the direction of external pheromone gradients.

Additionally, the spatial information about external gradients is likely to be processed at the level of G-protein coupled receptors and G-proteins, allowing the spatial information easier to be interpreted by polarity clusters. First, following ligand binding, receptors would be phosphorylated, endocytosed, and degraded (Hicke and Riezman, 1996; Hicke et al., 1998). The endocytosis of liganded receptor may improve gradient sensing by the "absorbing sphere" mechanism proposed by Endres et al (Endres and Wingreen, 2009a, b). However, when the endocytosis occurs after given pheromone, how fast the endocytosis is, and how pheromone level affects the endocytosis kinetics are remain to be determined to draw conclusions about the role of endocytosis in gradient sensing. Meanwhile, delivering newly synthesized receptors to membrane is probably biased toward the region with high concentrations of polarity factors, and thus reinforces the interaction between polarity patch, active receptors and free Gβγ. The cycling between receptor endocytosis and exocytosis over long time may integrate the abundance of external pheromone over time and amplify the concentration difference between the front and the back of a cell in a shallow gradient.

With high spatiotemporal resolution and mathematical modeling, we revealed an additional negative feedback imbedded in the polarity circuit. More than making initial polarity clusters oscillating, the negative feedback improved the robustness in spatial dynamics, in both polarity establishment and competition between multiple polarity clusters. Tuning the parameters controlling the strength and time delay of the negative feedback gave fine-tuned spatiotemporal dynamics of polarity factors. In those

kymographs describing how polarity patterns evolved, polarization also brought extra negative feedback to alter the frequency of temporal oscillation.

The properties of network motifs with different interaction topology have been intensively studied in temporal dynamics (Alon, 2006). The gain in robustness by negative feedback in both spatial and temporal dynamics raises the question: how different are the functions of a network motif in spatial dynamics compared with those in temporal dynamics? How would diffusion of components in a network motif affect the temporal behavior and alter characters of that motif? One similar example is that the perfect adaptation in temporal dynamics from an integral-feedback controller motif could also scale (adapt) morphogen gradients with the size of embryos (Ben-Zvi and Barkai, 2010). Although not all characterized network motifs can be adapted in spatial signaling with biological meanings, understanding the spatial dynamics of network motifs would extend our knowledge about the design principles of biological systems.

Another interesting modeling direction is to include the stochastic processes into spatial modeling and simulations. Fluctuation in protein numbers and slow diffusion may push individual reactions away from mean-field descriptions. For example, in section 3.5.1, only by including stochastic membrane binding and dissociation of Bem1, the uniform oscillation is changed to oscillatory clustering, relocation of clusters and rapid multi-cluster competition followed by oscillation. Then how would the noise from diffusion and other chemical reactions perturb the dynamics of polarity spot? Moreover, lots of biological processes, such as endocytosis and exocytosis, are discontinuous, adding extra noise to the system. With all these stochastic processes, how do cells buffer or make use of noise in spatial signaling? Spatial stochastic modeling and quantitative

live-cell imaging would help us to reveal mechanisms that regulate the spatiotemporal dynamics in a noisy environment.

APPENDIX I

I.1 Yeast strains

A list of strains used in these studies and their complete genotype is provided in **Table 1**.

Table 1. Strains used in Chapter 2

Strain	**Genotype**						
BY4741	*MAT***a**	*BAR1*	*LYS2*	*met15Δ$_0$*	*his3Δ1*	*leu2Δ$_0$*	*ura3Δ$_0$*
BY4742	*MAT*α	*BAR1*	*lys2Δ$_0$*	*MET15*	*his3Δ1*	*leu2Δ$_0$*	*ura3Δ$_0$*
[a]BY4742-2	*MAT*α	*bar1Δ::HisG -URA3-HisG*	*lys2Δ$_0$*	*MET15*	*his3Δ1*	*leu2Δ$_0$*	*ura3Δ$_0$*
[a]BY4741-15	*MAT***a**	*BAR1*	*LYS2*	*met15Δ$_0$*	*his3Δ1*	*leu2Δ$_0$*	*ura3Δ$_0$*
			GFP-BEM1::His3MX6				
[a]BY4741-30	*MAT***a**	*bar1Δ::HisG -URA3-HisG*	*LYS2*	*met15Δ$_0$*	*his3Δ1*	*leu2Δ$_0$*	*ura3Δ$_0$*
			GFP-BEM1::His3MX6				
[b]BYE007-1B	*MAT***a**	*BAR1*	*lys2Δ$_0$*	*MET15*	*his3Δ1*	*leu2Δ$_0$*	*ura3Δ$_0$*
[b]BYE007-1C	*MAT***a**	*BAR1*	*LYS2*	*met15Δ$_0$*	*his3Δ1*	*leu2Δ$_0$*	*ura3Δ$_0$*
[b]BYE007-2B	*MAT*α	*BAR1*	*LYS2*	*met15Δ$_0$*	*his3Δ1*	*leu2Δ$_0$*	*ura3Δ$_0$*
[b]BYE007-6C	*MAT***a**	*BAR1*	*lys2Δ$_0$*	*met15Δ$_0$*	*his3Δ1*	*leu2Δ$_0$*	*ura3Δ$_0$*
[b]BYE007-6A	*MAT*α	*bar1Δ::HisG -URA3-HisG*	*lys2Δ$_0$*	*MET15*	*his3Δ1*	*leu2Δ$_0$*	*ura3Δ$_0$*
[b]BYE007-2A	*MAT***a**	*bar1Δ::HisG -URA3-HisG*	*lys2Δ$_0$*	*MET15*	*his3Δ1*	*leu2Δ$_0$*	*ura3Δ$_0$*
[b]BYE007-3A	*MAT***a**	*bar1Δ::HisG -URA3-HisG*	*LYS2*	*met15Δ$_0$*	*his3Δ1*	*leu2Δ$_0$*	*ura3Δ$_0$*
[b]BYE007-4A	*MAT*α	*bar1Δ::HisG -URA3-HisG*	*LYS2*	*met15Δ$_0$*	*his3Δ1*	*leu2Δ$_0$*	*ura3Δ$_0$*
[b]BYE007-5B	*MAT***a**	*bar1Δ::HisG -URA3-HisG*	*lys2Δ$_0$*	*met15Δ$_0$*	*his3Δ1*	*leu2Δ$_0$*	*ura3Δ$_0$*
[b]BYE007-14D	*MAT*α	*bar1Δ::HisG -URA3-HisG*	*lys2Δ$_0$*	*MET15*	*his3Δ1*	*leu2Δ$_0$*	*ura3Δ$_0$*
KZ8-5C	*MAT***a**	*his4-38 ura1-1*					
KZ8-1D	*MAT*α	*His4-38 ura-1-1*					

[a]Strains are isogenic to BY4741 or BY4742.
[b]Strains are segregants from a cross between BY4741 and BY4742-2

Table 2. Mating mixtures.

Cross	Mating Partners (Decoy)	Cell type	*BAR1*	Selectable Marker Genotype
1	BYE007-1B x BYE007-1C	**a x a**	*BAR1* x *BAR1*	*lys2Δ$_0$/LYS2 MET15/ met15Δ$_0$*
2	BYE007-1B x BYE007-2B	**a x α**	*BAR1* x *BAR1*	*lys2Δ$_0$/LYS2 MET15/ met15Δ$_0$*
3	BYE007-2A x BYE007-3A	**a x a**	*bar1Δ* x *bar1Δ*	*lys2Δ$_0$/LYS2 MET15/ met15Δ$_0$*
4	BYE007-2A x BYE007-4A	**a x α**	*bar1Δ* x *bar1Δ*	*lys2Δ$_0$/LYS2 MET15/ met15Δ$_0$*
5	BYE007-1B x BYE007-6A	**a x α**	*BAR1* x *BAR1*	*lys2Δ$_0$/ lys2Δ$_0$ MET15/MET15*
6	BYE007-1C x BYE007-2B	**a x α**	*BAR1* x *BAR1*	*LYS2/LYS2 met15Δ$_0$/ met15Δ$_0$*
7	BYE007-2A x BYE007-14D	**a x α**	*bar1Δ* x *bar1Δ*	*lys2Δ$_0$/ lys2Δ$_0$ MET15/MET15*
8	BYE007-3A x BYE007-4A	**a x α**	*bar1Δ* x *bar1Δ*	*LYS2/LYS2 met15Δ$_0$/ met15Δ$_0$*
9	BYE007-1B x BYE007-1C	**a x a**	*BAR1* x *BAR1*	*lys2Δ$_0$/LYS2 MET15/ met15Δ$_0$*
	BYE007-5B	**a**	*bar1Δ*	*lys2Δ$_0$ met15Δ$_0$*)
10	BYE007-1B x BYE007-2B	**a x α**	*BAR1* x *BAR1*	*lys2Δ$_0$/LYS2 MET15/ met15Δ$_0$*
	BYE007-5B	**a**	*bar1Δ*	*lys2Δ$_0$ met15Δ$_0$*)
11	BYE007-2A x BYE007-3A	**a x a**	*bar1Δ* x *bar1Δ*	*lys2Δ$_0$/LYS2 MET15/ met15Δ$_0$*
	BYE007-6C	**a**	*BAR1*	*lys2Δ$_0$ met15Δ$_0$*)
12	BYE007-2A x BYE007-4A	**a x α**	*bar1Δ* x *bar1Δ*	*lys2Δ$_0$/LYS2 MET15/ met15Δ$_0$*
	BYE007-6C	**a**	*BAR1*	*lys2Δ$_0$ met15Δ$_0$*)

I.1.2 Chemotropic growth assays

The microfluidic device used for chemotropic assays and preparation of cells for imaging were described previously (Hao et al., 2008). The pheromone concentration ranged from 0 to 100 nM in the cell chamber for DIC and fluorescence imaging of *BAR1* cells (BY4741-15; *BEM1-GFP::His3MX6*) and 0 – 20 nM for *bar1Δ* cells (BY4741-30;

bar1Δ::HisG-URA3-HisG BEM1-GFP::His3MX6). To quantify self-avoidance for these two strains, the angle between two adjacent *MAT***a** cells was measured every 50 minutes from the time that cells started to elongate during chemotropic growth. This angle is defined as the angle between the two lines from the growth tip to the contact point of the two cells. The alignment between the direction of growth and the gradient was quantified by the angle between vectors indicating the growth direction and the direction of gradient at 350 minutes. Microscopy was performed with a Nikon Ti-E inverted microscope using a Photometrics CoolSNAP HQ2 Monochrome camera. Acquisition was performed with Metamorph (Molecular Devices; http://www.photomet.com). Image processing and analysis was done using MATLAB (Mathworks, Natick, MA) and ImageJ (http://rsbweb.nih.gov/ij/).

I.3 Quantitative mating assays

BAR1 and *bar1Δ* strains with nonrevertible and complementing nutritional markers were derived from BY4741and BY4742 (**Table 1**) and assessed for opposite cell-type (*MAT***a** x *MATα*) and same cell-type (*MAT***a** x *MAT***a**) mating efficiency in the absence or presence of exogenous pheromone using a modification of the procedure described by Sprague (Sprague, 1991). **Table 2** lists the different mating mixtures that were assessed in these experiments. Cells for making these mating mixtures were grown in liquid YPD medium to the early-log phase (5×10^6 to 1.5×10^7 cells per ml).

In experiments to assess the effects of mating pheromone on mating efficiencies, mixtures were made with 1×10^6 cells of each mating partner in suspensions (200 μl) containing 0, 0.75, 1.5, 3, or 6 μM of exogenous mating pheromone (α-factor). Each

suspension was pipetted onto a 25-mm filter (0.45-μm pore size; Millipore Corp., Bedford, Mass.) on the surface of a separate YPD plate with the corresponding concentration of mating pheromone.

In experiments to assess the effects of global Bar1, *MAT***a** *BAR1* or *bar1Δ* "decoy cells" lacking markers for selecting mating products with the tester partners were included to equalize the amount of Bar1 protease present in mating mixtures and ensure the total number of mating partners remained constant. *MAT***a** x *MAT***a** *BAR1* or *bar1Δ* mating mixtures were made with 2.5 x 10^5 cells of each tester partner and 5 x 10^5 cells of the *MAT***a** *bar1Δ* or *BAR1* decoy strain, respectively. Similarly, *MAT***a** x *MATα BAR1* or *bar1Δ* mating mixtures were made with 2.5 x 10^5 cells of each tester partner and 2.5 x 10^5 cells of the *MAT***a** *bar1Δ* or *BAR1* decoy strain. (Note, *MATα BAR1* cells do not produce or secrete Bar1.) After 5h (30°C), the cells were collected and diluted for plating on selective medium (synthetic dextrose supplemented with histidine, leucine, and uracil) to determine diploids/ml and on nonselective medium (synthetic complete dextrose) to determine total cells/ml (diploids and haploids). Reported mating efficiencies in the experiments without decoy cells are the ratio of diploids to total cells normalized to that for the reference *MAT***a** x *MATα BAR1* mixture without pheromone (**Table 2,** cross 2). For the experiments with decoy cells, mating efficiencies are the ratio of diploids to total cells normalized to the *MAT***a** x *MATα BAR1* mixture containing *bar1Δ* decoy cells. (**Table 2,** cross 10). Three independent assays were done for each mating mixture at the specified pheromone doses.

The auxotrophic markers in these strains are coding sequence deletions that are nonrevertible. Therefore, only fusion products with complementing nutritional markers

(*LYS2/lys2Δ*$_0$ *met15Δ*$_0$*/MET15*) grow on selective medium. To confirm this assertion, two plating controls were included in parallel with the quantitative mating assays. First, 2 x 10^6 cells of the *MAT***a** haploid strains used for mating mixtures 1 and 3 (**Table 2**) were incubated separately on YPD filters and plated on selective medium at the same dilution as for the *MAT***a** x *MAT***a** mating mixtures. Second, crosses between opposite cell-type partners with noncomplementing selectable markers (**Table 2**, Crosses 5-8) were made in the absence of exogenous pheromone, incubated on YPD filters, and plated on selective medium at the same dilution as for the *MAT***a** x *MAT*α mating mixtures. No colonies were observed on any of these control plates.

I.4 Cell-type verification

The cell-type of rare diploids from *MAT***a** x *MAT***a** mating mixtures was tested to discern whether they are products of same or opposite cell-type mating. (The latter could result if information at *MAT* switched from *MAT***a** to *MAT*α in rare cells in the population.) *MAT***a**/*MAT***a** diploid cells mate efficiently with *MAT*α but not *MAT***a** haploids to form viable triploid fusion products. By contrast, *MAT***a**/*MAT*α diploid cells mate with neither. We performed a qualitative mating assay with tester strains KZ8-5C (*MAT***a**) and KZ8-1D (*MAT*α) to test isolated colonies from the selective plates to distinguish between *MAT***a**/*MAT***a** and *MAT***a**/α fusion products (Sprague, 1991). Isolates from selective plates corresponding to *MAT***a** x *MAT***a** mating mixtures made without or with the specified amounts of exogenous pheromone were tested for mating ability (200 *BAR1* and 200 *bar1Δ* isolates from two independent experiments). 40 isolates from the *BAR1 MAT***a** x *MAT*α mating mixture without exogenous pheromone were included for

reference. All 400 diploids that were tested from the *MAT***a** x *MAT***a** mixtures mated with the *MAT*α tester but not the *MAT***a** tester strain consistent with assignment of the *MAT***a** cell-type to these fusion products. As expected, none of the 40 *MAT***a**/*MAT*α diploids mated with either tester strain. Additionally, 12 isolates each from selective plates of the *MAT***a** x *MAT***a** and *MAT***a** x *MAT*α mixtures without exogenous pheromone were tested for sporulation. No spore asci were observed for products from the same sex mating mixtures, whereas all of those from the opposite mating type mixtures produced spore asci.

APPENDIX II

II.1. Modeling oscillatory polarization with negative feedback

II.1.1 Positive feedback only

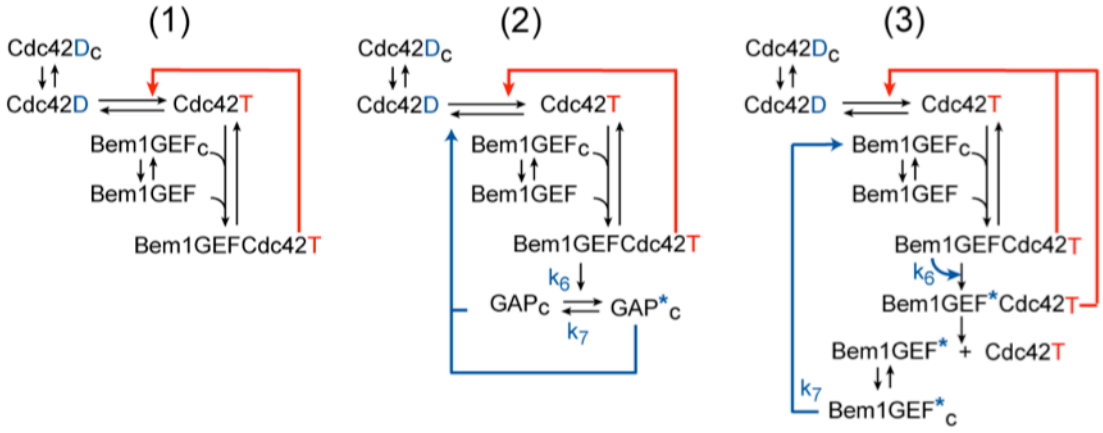

Figure S1. Models with and without negative feedback
Model (1) has positive feedback only, model (2) has a negative feedback loop via activation of a cytoplasmic GAP, and model (3) has negative feedback via disruption of the Bem1p complex. The reaction schemes correspond to the cartoons diagrammed in Fig. 3.6A. See text for details.

This model is similar to the one developed by Goryachev (Goryachev and Pokhilko, 2008; Howell et al., 2009) with the simplifying assumption that the role of the GDI, which binds GDP-Cdc42p and allows it to exchange between membrane and cytoplasm (Johnson et al., 2009), can be incorporated in the rate constants for GDP-Cdc42p exchange between membrane and cytoplasm (Fig. S3). Other model assumptions include:

(i) GDP-Cdc42p can exchange between the plasma membrane and cytoplasm. The membrane-bound and cytoplasmic forms are labeled as Cdc42D and $Cdc42I_c$, respectively. GTP-Cdc42p (Cdc42T) is always associated with the plasma membrane.

(ii) The Bem1p complex can exchange between cytoplasm (indicated as $Bem1GEF_c$) and membrane (indicated as $Bem1GEF_m$). Either form can bind to GTP-Cdc42p on the membrane, generating a complex indicated as Bem1GEFCdc42T.

(iii) The GEF activity of the Bem1p complex increases 2-fold when it binds GTP-Cdc42p (Howell et al., 2009).

(iv) GAP activity is spatially uniform and is incorporated in the first-order hydrolysis rate constant k_{2r}.

(v) The GEF and GAP are not saturated by substrate (GDP-Cdc42p or GTP-Cdc42p respectively).

(vi) The cell dimensions, total Cdc42p, and total Bem1p complex are all constant. The ratio of membrane volume to cytoplasmic volume is indicated by η.

(vii) All membrane-bound species have the same diffusion coefficient, D_m, and all cytosolic species the same diffusion coefficient, D_c, with $D_c >> D_m$.

Model parameter values are listed in the Table below. This model is described by the following reaction-diffusion equations:

$$\frac{\partial Cdc42I_c}{\partial t} = D_c \nabla^2 Cdc42I_c + \eta(-k_1 Cdc42I_c + k_{1r} Cdc42D)$$

$$\frac{\partial Cdc42D}{\partial t} = D_m \nabla^2 Cdc42D + k_1 Cdc42I_c - k_{1r} Cdc42D$$
$$-Cdc42D(k_2 Bem1GEF_m + k_{2p} Bem1GEFCdc42T) + k_{2r} Cdc42T$$

$$\frac{\partial Cdc42T}{\partial t} = D_m \nabla^2 Cdc42T + Cdc42D(k_2 Bem1GEF_m + k_{2p} Bem1GEFCdc42T)$$
$$-k_{2r} Cdc42T - (k_4 Bem1GEF_c + k_5 Bem1GEF_m) Cdc42T$$
$$+k_{5r} Bem1GEFCdc42T$$

$$\frac{\partial Bem1GEFCdc42T}{\partial t} = D_m \nabla^2 Bem1GEFCdc42T + (k_4 Bem1GEF_c + k_5 Bem1GEF_m) Cdc42T - k_{5r} Bem1GEFCdc42T$$

$$\frac{\partial Bem1GEF_c}{\partial t} = D_c \nabla^2 Bem1GEF_c + \eta(-k_3 Bem1GEF_c + k_{3r} Bem1GEF_m - k_4 Bem1GEF_c \cdot Cdc42T)$$

$$\frac{\partial Bem1GEF_m}{\partial t} = D_m \nabla^2 Bem1GEF_m + k_3 Bem1GEF_c - k_{3r} Bem1GEF_m - k_5 Bem1GEF_m \cdot Cdc42T + k_{5r} Bem1GEFCdc42T$$

II.1.2 Negative feedback via GAP activation

We assume that GTP-Cdc42p activates a cytoplasmic GAP, perhaps by phosphorylation of the GAP by the PAK Cla4p (Cla4p is a Cdc42p effector and part of the Bem1p complex) (Fig S3). The total GAP concentration is assumed to be 1 μM. The two states of the GAP are denoted as GAP_c (basal GAP activity) and GAP^*_c (high GAP activity). Active GAP is γ-fold more active than basal GAP. We imagine that a PAK bound to one molecule of GTP-Cdc42p would phosphorylate a GAP molecule transiently bound to a neighboring molecule of GTP-Cdc42p, so the GAP activation rate would be proportional to the product Bem1GEFCdc42T x Cdc42T x GAP_c. GAP inactivation is assumed to occur in the cytoplasm at a constant rate k_7. Model parameter values are listed in the Table below. This model is described by the following equations:

$$\frac{\partial Cdc42I_c}{\partial t} = D_c \nabla^2 Cdc42I_c + \eta(-k_1 Cdc42I_c + k_{1r} Cdc42D)$$

$$\frac{\partial Cdc42D}{\partial t} = D_m \nabla^2 Cdc42D + k_1 Cdc42I_c - k_{1r} Cdc42D$$
$$-Cdc42D(k_2 Bem1GEF_m + k_{2p} Bem1GEFCdc42T)$$
$$+k_{2r}(GAP_c + \gamma GAP_c^*)Cdc42T$$

$$\frac{\partial Cdc42T}{\partial t} = D_m \nabla^2 Cdc42T + Cdc42D(k_2 Bem1GEF_m + k_{2p} Bem1GEFCdc42T)$$
$$-k_{2r}(GAP_c + \gamma GAP_c^*)Cdc42T$$
$$-(k_4 Bem1GEF_c + k_5 Bem1GEF_m)Cdc42T + (k_{4r} + k_{5r})Bem1GEFCdc42T$$

$$\frac{\partial Bem1GEFCdc42T}{\partial t} = D_m \nabla^2 Bem1GEFCdc42T + (k_4 Bem1GEF_c + k_5 Bem1GEF_m)Cdc42T$$
$$-(k_{4r} + k_{5r})Bem1GEFCdc42T$$

$$\frac{\partial Bem1GEF_c}{\partial t} = D_c \nabla^2 Bem1GEF_c + \eta(-k_3 Bem1GEF_c + k_{3r} Bem1GEF_m$$
$$-k_4 Bem1GEF_c \cdot Cdc42T + k_{4r} Bem1GEFCdc42T)$$

$$\frac{\partial Bem1GEF_m}{\partial t} = D_m \nabla^2 Bem1GEF_m + k_3 Bem1GEF_c - k_{3r} Bem1GEF_m$$
$$-k_5 Bem1GEF_m \cdot Cdc42T + k_{5r} Bem1GEFCdc42T$$

$$\frac{\partial GAP_c}{\partial t} = D_c \nabla^2 GAP_c - \eta \cdot k_6 Bem1GEFCdc42T \cdot Cdc42T \cdot GAP_c + k_7 GAP_c^*$$

$$\frac{\partial GAP_c^*}{\partial t} = D_c \nabla^2 GAP_c^* + \eta \cdot k_6 Bem1GEFCdc42T \cdot Cdc42T \cdot GAP_c - k_7 GAP_c^*$$

II.1.3 Negative feedback via disruption of the Bem1p complex:

We assume that GTP-Cdc42p initiates a feedback loop that leads to the modification of the Bem1GEFCdc42T complex. Upon dissociation this yields Cdc42T and a modified Bem1GEF* that cannot rebind Cdc42T until its modification has been reversed by a spatially uniform cytoplasmic process characterized by the first-order rate

constant k_7 (Fig. S3). One possible mechanism for this negative feedback loop would be that the PAK Cla4p in one Bem1GEFCdc42T phosphorylates Bem1p complex components in a neighboring Bem1GEFCdc42T, changing their affinity for each other or for GTP-Cdc42p. In this scenario, the rate at which Bem1GEFCdc42T is modified is proportional to the square of the Bem1GEFCdc42T concentration. To keep additional assumptions to a minimum, we assumed that although the modified Bem1p complex cannot re-associate with GTP-Cdc42p, it retains basal GEF activity and transitions between the membrane and cytoplasm at the same rates as the unmodified complex. Model parameter values are listed in the Table below. This model is described by the following equations:

$$\frac{\partial Cdc42I_c}{\partial t} = D_c \nabla^2 Cdc42I_c + \eta(-k_1 Cdc42I_c + k_{1r} Cdc42D)$$

$$\begin{aligned}\frac{\partial Cdc42D}{\partial t} = {} & D_m \nabla^2 Cdc42D + k_1 Cdc42I_c - k_{1r} Cdc42D \\ & - Cdc42D(k_2(Bem1GEF_m + Bem1GEF_m^*) \\ & + k_{2p}(Bem1GEFCdc42T + Bem1GEF^*Cdc42T)) + k_{2r} Cdc42T\end{aligned}$$

$$\begin{aligned}\frac{\partial Cdc42T}{\partial t} = {} & D_m \nabla^2 Cdc42T + Cdc42D(k_2(Bem1GEF_m + Bem1GEF_m^*) \\ & + k_{2p}(Bem1GEFCdc42T + Bem1GEF^*Cdc42T)) - k_{2r} Cdc42T \\ & - (k_4 Bem1GEF_c + k_5 Bem1GEF_m) Cdc42T \\ & + k_{5r} Bem1GEFCdc42T + k_{5r} Bem1GEF^*Cdc42T\end{aligned}$$

$$\begin{aligned}\frac{\partial Bem1GEFCdc42T}{\partial t} = {} & D_m \nabla^2 Bem1GEFCdc42T \\ & + (k_4 Bem1GEF_c + k_5 Bem1GEF_m) Cdc42T \\ & - k_{5r} Bem1GEFCdc42T - k_6 Bem1GEFCdc42T^2\end{aligned}$$

$$\frac{\partial Bem1GEF^{*}Cdc42T}{\partial t} = D_m \nabla^2 Bem1GEF^{*}Cdc42T + k_6 Bem1GEFCdc42T^2 - k_{5r} Bem1GEF^{*}Cdc42T$$

$$\frac{\partial Bem1GEF_c}{\partial t} = D_c \nabla^2 Bem1GEF_c + \eta(-k_3 Bem1GEF_c + k_{3r} Bem1GEF_m - k_4 Bem1GEF_c \cdot Cdc42T) + k_7 Bem1GEF_c^{*}$$

$$\frac{\partial Bem1GEF_m}{\partial t} = D_m \nabla^2 Bem1GEF_m + k_3 Bem1GEF_c - k_{3r} Bem1GEF_m - k_5 Bem1GEF_m \cdot Cdc42T + k_{5r} Bem1GEFCdc42T$$

$$\frac{\partial Bem1GEF_m^{*}}{\partial t} = D_m \nabla^2 Bem1GEF_m^{*} + k_{5r} Bem1GEF^{*}Cdc42T - k_{3r} Bem1GEF_m^{*} + k_3 Bem1GEF_c^{*}$$

$$\frac{\partial Bem1GEF_c^{*}}{\partial t} = D_c \nabla^2 Bem1GEF_c^{*} + \eta(k_{3r} Bem1GEF_m^{*} - k_3 Bem1GEF_c^{*}) - k_7 Bem1GEF_c^{*}$$

II.1.4 Simulation with noise

In the main text, all of the simulations were deterministic, but given the cell-to-cell variability of polarity dynamics observed experimentally, we expect that stochastic noise has significant influence on the dynamics. As a first step to see how minimal amount of noise would affect the deterministic model, we added low-amplitude white noise to the Bem1p complex concentration at the membrane and in the cytoplasm (to preserve mass) and kept other species unaffected by noise. Another reason for choosing these two species is that cytoplasmic Bem1p complex is the least abundant species; fluctuations arising from stochastic variations in Bem1p complex behavior might be relatively large. We replaced the deterministic equations for $Bem1GEF_c$ and $Bem1GEF_m$

with:

$$\frac{\partial Bem1GEF_c}{\partial t} = D_c \nabla^2 Bem1GEF_c + \eta(-k_3 Bem1GEF_c + k_{3r} Bem1GEF_m - k_4 Bem1GEF_c \cdot Cdc42T) + k_7 Bem1GEF_c^* + \eta\sqrt{s}\xi(t)$$

$$\frac{\partial Bem1GEF_m}{\partial t} = D_m \nabla^2 Bem1GEF_m + k_3 Bem1GEF_c - k_{3r} Bem1GEF_m - k_5 Bem1GEF_m \cdot Cdc42T + k_{5r} Bem1GEFCdc42T - \sqrt{s}\xi(t)$$

where ξ(t) is temporally uncorrelated, statistically independent Gaussian white noise, and the strength of this noise is set by the constant s=0.0001.

In the presence of the simple noise term, the model predicts sustained oscillatory clustering as well as repeated competing and relocating with proper parameters. It seems likely that septins or other extrinsic non-modeled factors would stabilize the clusters in cells.

II.1.5 Parameter Values

Model parameter values for all models are listed in the Table below. Here we provide a brief description of how the model 1 parameter values were estimated.

The GDI-related rate constants (simplified to k1 and k1r in this work) were estimated based on real-time FRET measurements reporting interaction kinetics of recombinant human Cdc42p and GDI with insect cell membranes in vitro (Johnson et al., 2009).

The GEF- and GAP-regulated rate constants for GDP/GTP exchange and GTP hydrolysis by Cdc42p (k2, k2p, and k2r) were estimated based on in vitro rates of GDP

release and GTP hydrolysis by recombinant yeast Cdc42p upon incubation with crude yeast lysates from synchronized cells (Howell et al., 2009).

Because we do not have specific data on the weak interaction of Bem1p complexes with the membrane, the relevant rate constants (k3 and k3r) were estimated based on similar PX-domain/membrane interactions in the literature (Goryachev and Pokhilko, 2008)

The binding/dissociation of the Bem1p complex to/from GTP-Cdc42p is a simplification of a more complex situation in which reversible binding reactions occur between GTP-Cdc42p and PAK, between PAK and Bem1p, and between Bem1p and Cdc24p. Because the SH3-mediated PAK-Bem1p interaction is likely to be the most labile of these, the relevant rate constants (k4, k5, and k5r) are estimated based on other SH3 interactions in the literature (Howell et al., 2009).

The membrane diffusion constant was estimated based on FRAP analysis of GFP-tagged prenylated reporters in latrunculin-treated cells (to eliminate endocytosis) (Marco et al., 2007).

Although the general ballpark values of these parameters are as realistic as we are able to estimate, the modeling results in this paper should be treated as qualitative rather than quantitative. Because the mechanism of negative feedback is unknown, the negative feedback parameters (k6 and k7) are purely speculative.

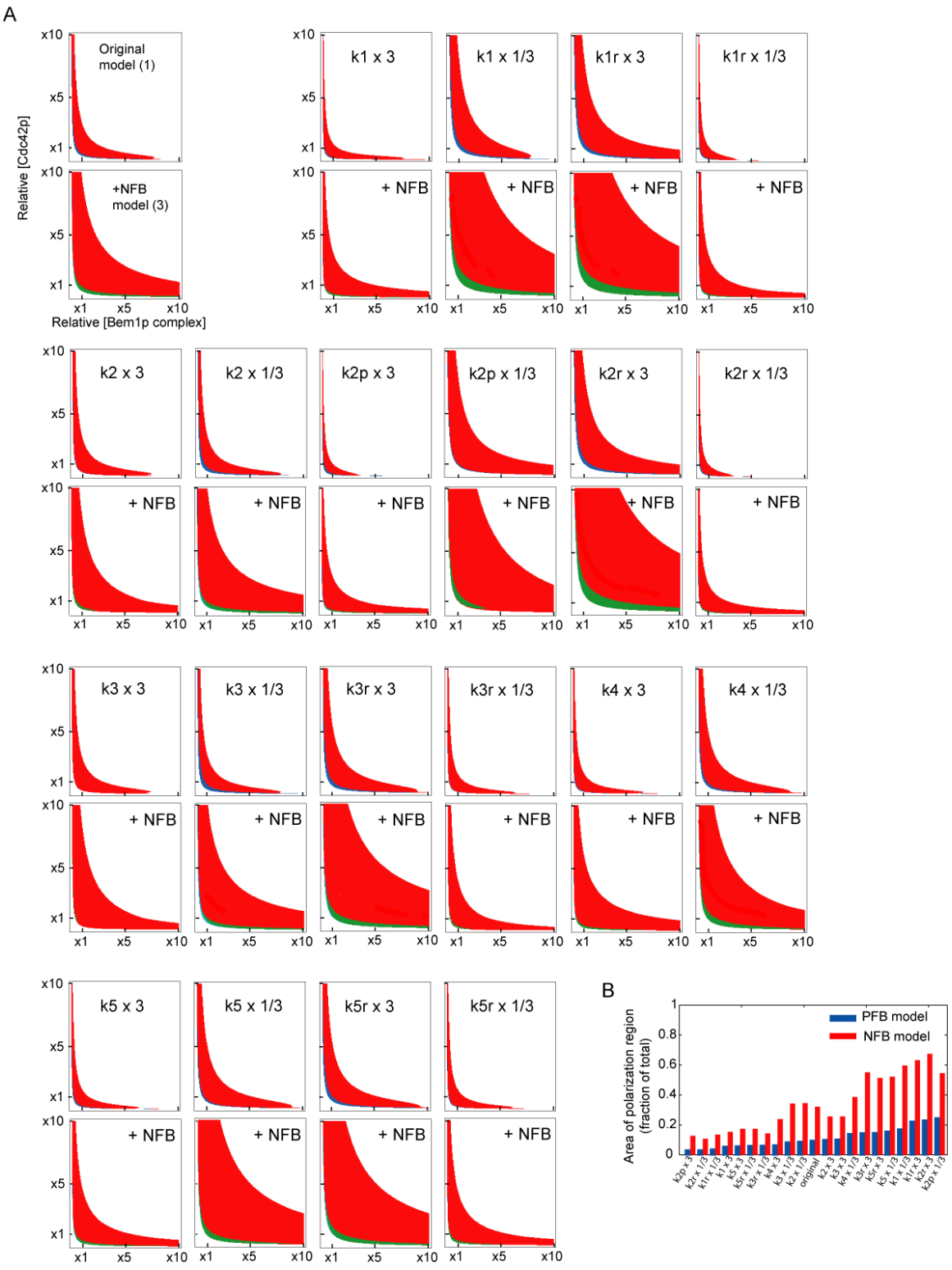

Figure S2. The effect of negative feedback on robustness does not depend on specific rate parameters

A) Bifurcation diagrams of model (1) (positive feedback only) and model (3) (with negative feedback via the Bem1p complex) are displayed as pairs (model 1 above, model 3 below) for various values of the rate constants. Each parameter was increased or decreased 3-fold from its original value, and the Turing-unstable region (red) was determined by linear stability analysis. B) Summary indicating that negative feedback increases the polarization region in all cases. The area of the polarization region (red) as a fraction of the total area in relative Cdc42p and Bem1p complex space is plotted as a measure of the model's robustness to varying levels of polarity factors. Blue and red bars report model (1) and (3) respectively. Paired bars use the same parameter set, and pairs are ordered by increasing robustness of model 1.

Table 3. Parameter Values

	Model (1)	Model (2)	Model (3)	Reference (Model 1)
k_1	0.9 s^{-1}	1 s^{-1}	0.9 s^{-1}	This work
k_{1r}	0.15 s^{-1}	0.125 s^{-1}	0.15 s^{-1}	This work
k_2	0.16 $\mu M^{-1}s^{-1}$	0.2 $\mu M^{-1}s^{-1}$	0.16 $\mu M^{-1}s^{-1}$	(Howell et al., 2009)
k_{2p}	0.35 $\mu M^{-1}s^{-1}$	0.6 $\mu M^{-1}s^{-1}$	0.35 $\mu M^{-1}s^{-1}$	(Howell et al., 2009)
k_{2r}	0.32 s^{-1}	0.3 s^{-1}	0.32 s^{-1}	(Howell et al., 2009)
k_3	10 s^{-1}	10 s^{-1}	10 s^{-1}	(Goryachev and Pokhilko, 2008)
k_{3r}	10 s^{-1}	10 s^{-1}	10 s^{-1}	(Goryachev and Pokhilko, 2008)
k_4	10 $\mu M^{-1}s^{-1}$	7.5 $\mu M^{-1}s^{-1}$	10 $\mu M^{-1}s^{-1}$	(Goryachev and Pokhilko, 2008)
k_{4r}	-	2.5 s^{-1}	-	This work
k_5	10 $\mu M^{-1}s^{-1}$	10 $\mu M^{-1}s^{-1}$	10 $\mu M^{-1}s^{-1}$	(Goryachev and Pokhilko, 2008)
k_{5r}	10 s^{-1}	10 s^{-1}	10 s^{-1}	(Howell et al., 2009)
k_6	-	0.2 $\mu M^{-2}s^{-1}$	0.05 $\mu M^{-1}s^{-1}$	This work
k_7	-	0.00475 s^{-1}	0.0022 s^{-1}	This work
γ	-	10	-	This work
η	0.01	0.01	0.01	(Goryachev and Pokhilko, 2008)
D_c	10 $\mu m^2 s^{-1}$	10 $\mu m^2 s^{-1}$	10 $\mu m^2 s^{-1}$	(Goryachev and Pokhilko, 2008)
D_m	0.036 $\mu m^2 s^{-1}$	0.036 $\mu m^2 s^{-1}$	0.036 $\mu m^2 s^{-1}$	(Marco et al., 2007)
Total Cdc42p	5 μM	5 μM	5 μM	(Goryachev and Pokhilko, 2008)
Total Bem1p complex	0.017 μM	0.017 μM	0.017 μM	(Goryachev and Pokhilko, 2008)
Total GAP	-	1 μM	-	This work

II.2. Competition and equalization of two polarity foci

We used model (1) (positive feedback only) and model (3) (with negative feedback) to examine how negative feedback affects competition between polarized foci. Simulations were done on a 1D line ($L=5\pi$ μm) with periodic boundary conditions, representing a cell perimeter.

To simulate competition between two unequal GTP-Cdc42p foci, we evolved a symmetric two-peak solution for the points in parameter space shown in Fig. 6. This was done by transiently including a spatial dependence of the rate constant k_3 for Bem1 binding to the membrane. Specifically, we took $k_3(\theta)$ to consist of two identical Gaussian distributions centered at $\pi/2$ and $3\pi/2$. After the spatial dependence of k_3 was removed and the two peaks had reached steady state, we adjusted the profile of GTP-Cdc42p from a 50:50 ratio between the peaks to various other ratios (55:45, 60:40, 70:30, 80:20 or 90:10) keeping total Cdc42p constant. The shared points (white circles in Fig. 6) are limited to low Bem1p complex concentrations because model (1) could not sustain a two-peak distribution with larger amounts of Bem1p complex: once the spatial dependence of k_3 was withdrawn, the peaks flattened out to a homogeneous distribution that was unstable to spatial perturbation.

The competition simulations for each point started with the two-peak profiles adjusted as described above. We defined the duration of competition as the time taken to reach a state in which the peak GTP-Cdc42p concentration in the larger focus was 10-fold that of the smaller focus.

Whereas all points tested for model (1) (positive feedback only) displayed

competition, in model (3) (with negative feedback) there was a transition from competition (point #1, Fig. S3) to conditional equalization (point #2, Fig. S3) as the total amounts of Cdc42p and the Bem1p complex were increased. By conditional equalization we mean that the two peaks became equal in size if the initial difference was less than a certain threshold. As the total Cdc42p and Bem1p complex amounts were increased further, two different peaks would equalize regardless of their relative size (Fig. 3.10E; point #3, Fig. S3). These three behaviors are depicted as blue (competition), green (equalization), and blue-green (conditional equalization) regions in Fig. S3, as determined by sampling 53 randomly distributed points.

To examine how this behavior impacts a biologically realistic situation, we asked how many peaks would form if simulations were initiated with a variety of initial conditions. We show three representative points in Fig. S3C. In the competition region, only one peak formed no matter what initial conditions were used (point #1, Fig. S3C). In the conditional equalization region, different initial conditions led to either one or two peaks (point #2, Fig. S3C). In the equalization region, two peaks of GTP-Cdc42p were established independent of the initial conditions (point #3, Fig. S3C).

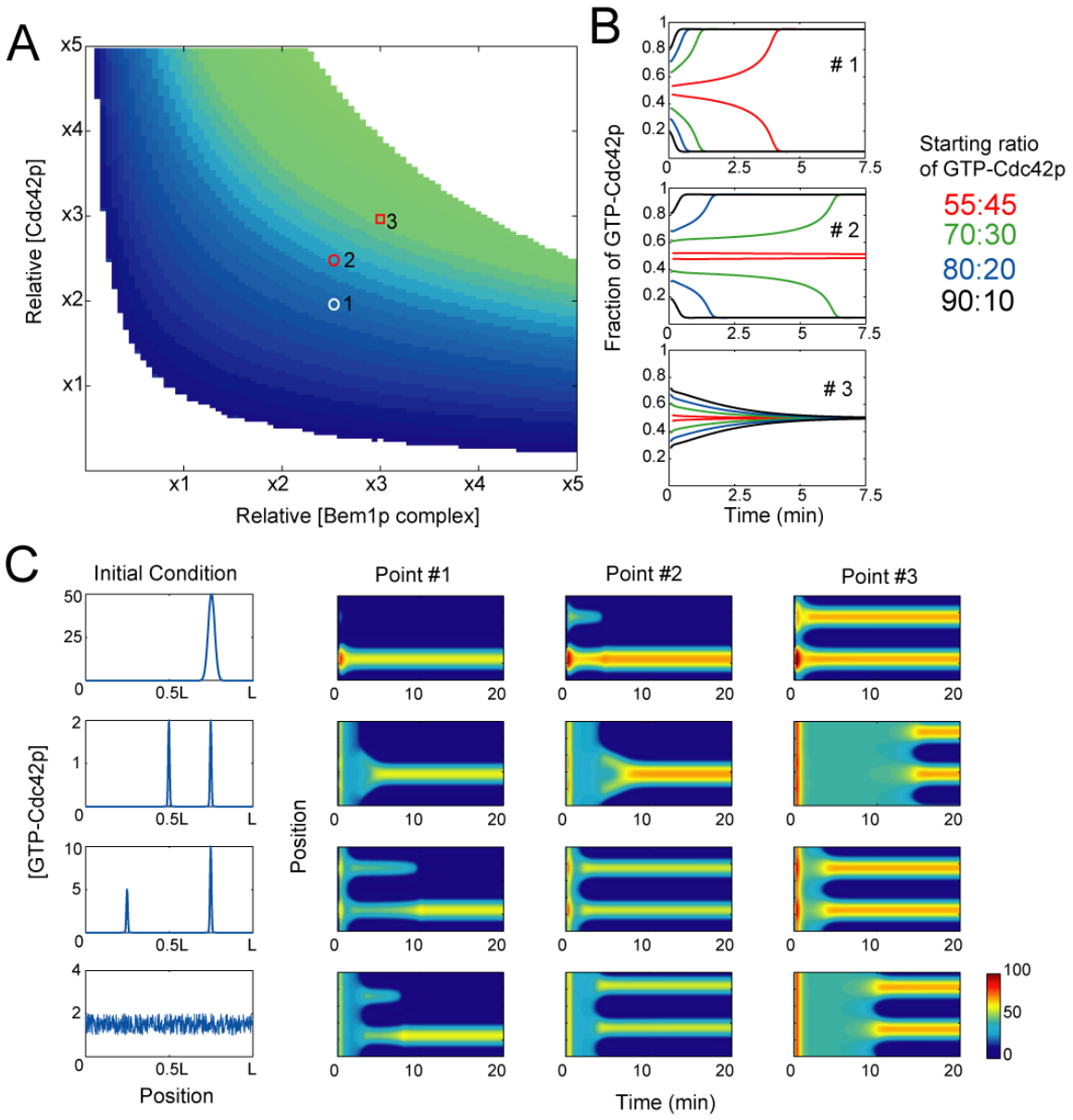

Figure S3. Competition and equalization between clusters in Model (3)

A) Three regions with different types of competition behavior in [Cdc42]-[Bem1-complex] bifurcation diagram of Model (3). Blue region (competition): two unequal peaks compete and the larger one wins. Green region (equalization): two unequal peaks equalize and then coexist. Blue-green region (conditional equalization): competition or equalization, depending on the starting difference between the two peaks (see B). White region: no polarization occurs. The numbered symbols indicate positions simulated in B.

B) Simulated competition and equalization. Simulations were initiated with two peaks at opposite ends of the cell perimeter, containing the indicated color-coded ratios of GTP-Cdc42p. The fraction of GTP-Cdc42p in each peak is plotted as a function of time. Top: at point #1 (white circle), the two peaks always compete. Middle: at point #2 (red circle), two similar-sized peaks

equalize (e.g. ratio 55:45) but very unequal peaks compete (e.g. ratio 70:30). Bottom: at point #3 (red square), two peaks always equalize.

C) Simulated behavior with different initial conditions. Simulations were initiated with the initial perturbations in GTP-Cdc42p shown at left, at the points in the bifurcation diagram (#1-3) indicated in A. Top: a single initial spike leads to development of one peak at points #1 and #2, but two peaks at point #3. Second row: two nearby spikes merge to form a single peak at points #1 and #2, but two peaks at point #3. Third row: two unequal spikes compete at point #1 but equalize at points #2 and 3. Bottom: a noisy initial input develops to a single peak at point #1 but two equal peaks at points #2 and 3. Thus, in the competition region all simulations develop a single peak and in the equalization region all simulations develop two peaks, independent of initial conditions. In between, the number of peaks depends on initial condition (point #2).

REFERENCES

Adams, A.E.M., Johnson, D.I., Longnecker, R.M., Sloat, B.F., and Pringle, J.R. (1990). Cdc42 and Cdc43, 2 Additional Genes Involved in Budding and the Establishment of Cell Polarity in the Yeast Saccharomyces-Cerevisiae. Journal of Cell Biology *111*, 131-142.

Alby, K., Schaefer, D., and Bennett, R.J. (2009). Homothallic and heterothallic mating in the opportunistic pathogen Candida albicans. Nature *460*, 890-893.

Alon, U. (2006). An Introduction to Systems Biology: Design Principles of Biological Circuits (Chapman & Hall/CRC).

Altschuler, S.J., Angenent, S.B., Wang, Y., and Wu, L.F. (2008). On the spontaneous emergence of cell polarity. Nature *454*, 886-889.

Andrews, S.S., Addy, N.J., Brent, R., and Arkin, A.P. (2010). Detailed simulations of cell biology with Smoldyn 2.1. PLoS Comput Biol *6*, e1000705.

Ayscough, K.R., Stryker, J., Pokala, N., Sanders, M., Crews, P., and Drubin, D.G. (1997). High rates of actin filament turnover in budding yeast and roles for actin in establishment and maintenance of cell polarity revealed using the actin inhibitor latrunculin-A. J Cell Biol *137*, 399-416.

Barkai, N., Rose, M.D., and Wingreen, N.S. (1998). Protease helps yeast find mating partners. Nature *396*, 422-423.

Behar, M., Hao, N., Dohlman, H.G., and Elston, T.C. (2007). Mathematical and computational analysis of adaptation via feedback inhibition in signal transduction pathways. Biophys J *93*, 806-821.

Ben-Zvi, D., and Barkai, N. (2010). Scaling of morphogen gradients by an expansion-repression integral feedback control. Proc Natl Acad Sci U S A *107*, 6924-6929.

Bender, A. (1993). Genetic evidence for the roles of the bud-site-selection genes BUD5 and BUD2 in control of the Rsr1p (Bud1p) GTPase in yeast. Proc Natl Acad Sci U S A *90*, 9926-9929.

Bender, A., and Pringle, J.R. (1989a). Multicopy suppression of the cdc24 budding defect in yeast by CDC42 and three newly identified genes including the ras-related gene RSR1. Proc Natl Acad Sci U S A *86*, 9976-9980.

Bender, A., and Pringle, J.R. (1989b). Multicopy suppression of the cdc24 budding defect in yeast by CDC42 and three newly identified genes including the ras-related gene RSR1. Proc. Natl. Acad. Sci. U.S.A. *86*, 9976-9980.

Bender, A., and Pringle, J.R. (1991). Use of a screen for synthetic lethal and multicopy suppressee mutants to identify two new genes involved in morphogenesis in

Saccharomyces cerevisiae. Mol Cell Biol *11*, 1295-1305.

Bender, A., and Sprague, G.F., Jr. (1989). Pheromones and pheromone receptors are the primary determinants of mating specificity in the yeast Saccharomyces cerevisiae. Genetics *121*, 463-476.

Bi, E., Chiavetta, J.B., Chen, H., Chen, G.C., Chan, C.S., and Pringle, J.R. (2000). Identification of novel, evolutionarily conserved Cdc42p-interacting proteins and of redundant pathways linking Cdc24p and Cdc42p to actin polarization in yeast. Molecular biology of the cell *11*, 773-793.

Bose, I., Irazoqui, J.E., Moskow, J.J., Bardes, E.S., Zyla, T.R., and Lew, D.J. (2001). Assembly of scaffold-mediated complexes containing Cdc42p, the exchange factor Cdc24p, and the effector Cla4p required for cell cycle-regulated phosphorylation of Cdc24p. The Journal of biological chemistry *276*, 7176-7186.

Brandman, O., and Meyer, T. (2008). Feedback loops shape cellular signals in space and time. Science (New York, N.Y *322*, 390-395.

Butty, A.C., Pryciak, P.M., Huang, L.S., Herskowitz, I., and Peter, M. (1998). The role of Far1p in linking the heterotrimeric G protein to polarity establishment proteins during yeast mating. Science *282*, 1511-1516.

Chan, R.K., and Otte, C.A. (1982). Physiological characterization of Saccharomyces cerevisiae mutants supersensitive to G1 arrest by a factor and alpha factor pheromones. Mol Cell Biol *2*, 21-29.

Chant, J., and Herskowitz, I. (1991a). Genetic control of bud site selection in yeast by a set of gene products that constitute a morphogenetic pathway. Cell *65*, 1203-1212.

Chant, J., and Herskowitz, I. (1991b). Genetic control of bud site selection in yeast by a set of gene products that constitute a morphogenetic pathway. Cell *65*, 1203-1212.

Chant, J., and Pringle, J.R. (1995). Patterns of bud-site selection in the yeast Saccharomyces cerevisiae. J Cell Biol *129*, 751-765.

Cheong, R., and Levchenko, A. (2010). Oscillatory signaling processes: the how, the why and the where. Curr Opin Genet Dev *20*, 665-669.

Ciejek, E., and Thorner, J. (1979). Recovery of S. cerevisiae a cells from G1 arrest by alpha factor pheromone requires endopeptidase action. Cell *18*, 623-635.

Cook, J.G., Bardwell, L., Kron, S.J., and Thorner, J. (1996). Two novel targets of the MAP kinase Kss1 are negative regulators of invasive growth in the yeast Saccharomyces cerevisiae. Genes Dev *10*, 2831-2848.

Cross, M.C., and Hohenberg, P.C. (1993). Interaction of Turing and Hopf Bifurcations in Chemical-Systems. Reviews of Modern Physics *65*, 851-1112.

De Wit, A., Lima, D., Dewel, G., and Borckmans, P. (1996). Spatiotemporal dynamics near a codimension-two point. Phys Rev E Stat Phys Plasmas Fluids Relat Interdiscip Topics *54*, 261-271.

Dertinger, S.K.W., Chiu, D.T., Jeon, N.L., and Whitesides, G.M. (2001). Generation of gradients having complex shapes using microfluidic networks. Analytical chemistry *73*, 1240-1246.

Dietrich, F.S., Voegeli, S., Brachat, S., Lerch, A., Gates, K., Steiner, S., Mohr, C., Pohlmann, R., Luedi, P., Choi, S., *et al.* (2004). The Ashbya gossypii genome as a tool for mapping the ancient Saccharomyces cerevisiae genome. Science (New York, N.Y *304*, 304-307.

Dohlman, H.G., and Thorner, J.W. (2001). Regulation of G protein-initiated signal transduction in yeast: paradigms and principles. Annual review of biochemistry *70*, 703-754.

Dorer, R., Pryciak, P.M., and Hartwell, L.H. (1995). Saccharomyces cerevisiae cells execute a default pathway to select a mate in the absence of pheromone gradients. J Cell Biol *131*, 845-861.

Drogen, F., O'Rourke, S.M., Stucke, V.M., Jaquenoud, M., Neiman, A.M., and Peter, M. (2000). Phosphorylation of the MEKK Ste11p by the PAK-like kinase Ste20p is required for MAP kinase signaling in vivo. Curr Biol *10*, 630-639.

Elion, E.A., Satterberg, B., and Kranz, J.E. (1993). FUS3 phosphorylates multiple components of the mating signal transduction cascade: evidence for STE12 and FAR1. Mol Biol Cell *4*, 495-510.

Endres, R.G., and Wingreen, N.S. (2008). Accuracy of direct gradient sensing by single cells. Proc Natl Acad Sci U S A *105*, 15749-15754.

Endres, R.G., and Wingreen, N.S. (2009a). Accuracy of direct gradient sensing by cell-surface receptors. Prog Biophys Mol Biol *100*, 33-39.

Endres, R.G., and Wingreen, N.S. (2009b). Maximum likelihood and the single receptor. Phys Rev Lett *103*, 158101.

Erdman, S., and Snyder, M. (2001). A filamentous growth response mediated by the yeast mating pathway. Genetics *159*, 919-928.

Errede, B., Gartner, A., Zhou, Z., Nasmyth, K., and Ammerer, G. (1993). MAP kinase-related FUS3 from S. cerevisiae is activated by STE7 in vitro. Nature *362*, 261-264.

Evangelista, M., Pruyne, D., Amberg, D.C., Boone, C., and Bretscher, A. (2002). Formins direct Arp2/3-independent actin filament assembly to polarize cell growth in yeast. Nat Cell Biol *4*, 32-41.

Feijo, J.A., Sainhas, J., Holdaway-Clarke, T., Cordeiro, M.S., Kunkel, J.G., and Hepler, P.K. (2001). Cellular oscillations and the regulation of growth: the pollen tube paradigm. Bioessays *23*, 86-94.

Garcia, G.L., Rericha, E.C., Heger, C.D., Goldsmith, P.K., and Parent, C.A. (2009). The group migration of Dictyostelium cells is regulated by extracellular chemoattractant degradation. Mol Biol Cell *20*, 3295-3304.

Garrenton, L.S., Stefan, C.J., McMurray, M.A., Emr, S.D., and Thorner, J. (2010). Pheromone-induced anisotropy in yeast plasma membrane phosphatidylinositol-4,5-bisphosphate distribution is required for MAPK signaling. Proc Natl Acad Sci U S A *107*, 11805-11810.

Gartner, A., Nasmyth, K., and Ammerer, G. (1992). Signal transduction in Saccharomyces cerevisiae requires tyrosine and threonine phosphorylation of FUS3 and KSS1. Genes Dev *6*, 1280-1292.

Gierer, A., and Meinhardt, H. (1972). A theory of biological pattern formation. Kybernetik *12*, 30-39.

Gladfelter, A.S., Pringle, J.R., and Lew, D.J. (2001). The septin cortex at the yeast mother-bud neck. Current opinion in microbiology *4*, 681-689.

Good, M., Tang, G., Singleton, J., Remenyi, A., and Lim, W.A. (2009). The Ste5 scaffold directs mating signaling by catalytically unlocking the Fus3 MAP kinase for activation. Cell *136*, 1085-1097.

Goryachev, A.B., and Pokhilko, A.V. (2008). Dynamics of Cdc42 network embodies a Turing-type mechanism of yeast cell polarity. FEBS Lett *582*, 1437-1443.

Gulli, M.P., Jaquenoud, M., Shimada, Y., Niederhauser, G., Wiget, P., and Peter, M. (2000). Phosphorylation of the Cdc42 exchange factor Cdc24 by the PAK-like kinase Cla4 may regulate polarized growth in yeast. Mol. Cell *6*, 1155-1167.

Hao, N., Nayak, S., Behar, M., Shanks, R.H., Nagiec, M.J., Errede, B., Hasty, J., Elston, T.C., and Dohlman, H.G. (2008). Regulation of cell signaling dynamics by the protein kinase-scaffold Ste5. Mol Cell *30*, 649-656.

Harkins, H.A., Page, N., Schenkman, L.R., De Virgilio, C., Shaw, S., Bussey, H., and Pringle, J.R. (2001). Bud8p and Bud9p, proteins that may mark the sites for bipolar budding in yeast. Mol Biol Cell *12*, 2497-2518.

Harris, S.D. (2008). Branching of fungal hyphae: regulation, mechanisms and comparison with other branching systems. Mycologia *100*, 823-832.

Hecht, I., Kessler, D.A., and Levine, H. (2010). Transient Localized Patterns in Noise-Driven Reaction-Diffusion Systems. Physical Review Letters *104*, -.

Hepler, P.K., Vidali, L., and Cheung, A.Y. (2001). Polarized cell growth in higher plants. Annu Rev Cell Dev Biol *17*, 159-187.

Hicke, L., and Riezman, H. (1996). Ubiquitination of a yeast plasma membrane receptor signals its ligand-stimulated endocytosis. Cell *84*, 277-287.

Hicke, L., Zanolari, B., and Riezman, H. (1998). Cytoplasmic tail phosphorylation of the alpha-factor receptor is required for its ubiquitination and internalization. J Cell Biol *141*, 349-358.

Hicks, J.B., and Herskowitz, I. (1976). Evidence for a new diffusible element of mating pheromones in yeast. Nature *260*, 246-248.

Howell, A.S., Jin, M., Wu, C.F., Zyla, T.R., Elston, T.C., and Lew, D.J. (2012). Negative feedback enhances robustness in the yeast polarity establishment circuit. Cell *accepted*.

Howell, A.S., Savage, N.S., Johnson, S.A., Bose, I., Wagner, A.W., Zyla, T.R., Nijhout, H.F., Reed, M.C., Goryachev, A.B., and Lew, D.J. (2009). Singularity in polarization: rewiring yeast cells to make two buds. Cell *139*, 731-743.

Iglesias, P.A., and Devreotes, P.N. (2008). Navigating through models of chemotaxis. Curr Opin Cell Biol *20*, 35-40.

Irazoqui, J.E., Gladfelter, A.S., and Lew, D.J. (2003). Scaffold-mediated symmetry breaking by Cdc42p. Nat Cell Biol *5*, 1062-1070.

Irazoqui, J.E., Howell, A.S., Theesfeld, C.L., and Lew, D.J. (2005). Opposing roles for actin in Cdc42p polarization. Molecular biology of the cell *16*, 1296-1304.

Irazoqui, J.E., and Lew, D.J. (2004). Polarity establishment in yeast. J Cell Sci *117*, 2169-2171.

Ito, T., Matsui, Y., Ago, T., Ota, K., and Sumimoto, H. (2001). Novel modular domain PB1 recognizes PC motif to mediate functional protein-protein interactions. Embo J *20*, 3938-3946.

Jackson, C.L., and Hartwell, L.H. (1990). Courtship in S. cerevisiae: both cell types choose mating partners by responding to the strongest pheromone signal. Cell *63*, 1039-1051.

Janetopoulos, C., Ma, L., Devreotes, P.N., and Iglesias, P.A. (2004). Chemoattractant-induced phosphatidylinositol 3,4,5-trisphosphate accumulation is spatially amplified and adapts, independent of the actin cytoskeleton. Proc Natl Acad Sci U S A *101*, 8951-8956.

Jenness, D.D., Burkholder, A.C., and Hartwell, L.H. (1986). Binding of alpha-factor pheromone to Saccharomyces cerevisiae a cells: dissociation constant and number of binding sites. Mol Cell Biol *6*, 318-320.

Jeon, N.L., Dertinger, S.K.W., Chiu, D.T., Choi, I.S., Stroock, A.D., and Whitesides, G.M. (2000). Generation of solution and surface gradients using microfluidic systems. Langmuir *16*, 8311-8316.

Jilkine, A., and Edelstein-Keshet, L. (2011). A comparison of mathematical models for polarization of single eukaryotic cells in response to guided cues. PLoS Comput Biol *7*, e1001121.

Johnson, J.L., Erickson, J.W., and Cerione, R.A. (2009). New insights into how the Rho guanine nucleotide dissociation inhibitor regulates the interaction of Cdc42 with membranes. J Biol Chem *284*, 23860-23871.

Johnson, J.M., Jin, M., and Lew, D.J. (2011). Symmetry breaking and the establishment of cell polarity in budding yeast. Current opinion in genetics & development *21*, 740-746.

Johnson, J.M., Savage, N.S., Jin, M., Zyla, T.R., Elston, T.C., and Lew, D.J. (2012). Tracking shallow chemical gradient by actin-driven wandering of the polarity site. submitted.

Kaksonen, M., Sun, Y., and Drubin, D.G. (2003). A pathway for association of receptors, adaptors, and actin during endocytic internalization. Cell *115*, 475-487.

Kang, P.J., Angerman, E., Nakashima, K., Pringle, J.R., and Park, H.O. (2004). Interactions among Rax1p, Rax2p, Bud8p, and Bud9p in marking cortical sites for bipolar bud-site selection in yeast. Mol Biol Cell *15*, 5145-5157.

Kang, P.J., Sanson, A., Lee, B., and Park, H.O. (2001). A GDP/GTP exchange factor involved in linking a spatial landmark to cell polarity. Science *292*, 1376-1378.

Kim, H.B., Haarer, B.K., and Pringle, J.R. (1991). Cellular morphogenesis in the Saccharomyces cerevisiae cell cycle: localization of the CDC3 gene product and the timing of events at the budding site. J Cell Biol *112*, 535-544.

Knaus, M., Pelli-Gulli, M.P., van Drogen, F., Springer, S., Jaquenoud, M., and Peter, M. (2007). Phosphorylation of Bem2p and Bem3p may contribute to local activation of Cdc42p at bud emergence. Embo J *26*, 4501-4513.

Knechtle, P., Dietrich, F., and Philippsen, P. (2003). Maximal polar growth potential depends on the polarisome component AgSpa2 in the filamentous fungus Ashbya gossypii. Molecular biology of the cell *14*, 4140-4154.

Koch, G., Tanaka, K., Masuda, T., Yamochi, W., Nonaka, H., and Takai, Y. (1997). Association of the Rho family small GTP-binding proteins with Rho GDP dissociation inhibitor (Rho GDI) in Saccharomyces cerevisiae. Oncogene *15*, 417-422.

Kozubowski, L., Saito, K., Johnson, J.M., Howell, A.S., Zyla, T.R., and Lew, D.J. (2008). Symmetry-breaking polarization driven by a Cdc42p GEF-PAK complex. Curr Biol *18*, 1719-1726.

Kronstad, J.W., Holly, J.A., and MacKay, V.L. (1987). A yeast operator overlaps an upstream activation site. Cell *50*, 369-377.

Kutscher, B., Devreotes, P., and Iglesias, P.A. (2004). Local excitation, global inhibition mechanism for gradient sensing: an interactive applet. Science's STKE : signal transduction knowledge environment *2004*, pl3.

Lamson, R.E., Takahashi, S., Winters, M.J., and Pryciak, P.M. (2006). Dual role for membrane localization in yeast MAP kinase cascade activation and its contribution to signaling fidelity. Curr Biol *16*, 618-623.

Layton, A.T., Savage, N.S., Howell, A.S., Carroll, S.Y., Drubin, D.G., and Lew, D.J. (2011). Modeling vesicle traffic reveals unexpected consequences for Cdc42p-mediated polarity establishment. Curr Biol *21*, 184-194.

Levchenko, A., and Iglesias, P.A. (2002). Models of eukaryotic gradient sensing: application to chemotaxis of amoebae and neutrophils. Biophys J *82*, 50-63.

Levine, H., Kessler, D.A., and Rappel, W.J. (2006). Directional sensing in eukaryotic chemotaxis: a balanced inactivation model. Proc Natl Acad Sci U S A *103*, 9761-9766.

Ma, W., Trusina, A., El-Samad, H., Lim, W.A., and Tang, C. (2009). Defining network topologies that can achieve biochemical adaptation. Cell *138*, 760-773.

Madden, K., and Snyder, M. (1992). Specification of sites for polarized growth in Saccharomyces cerevisiae and the influence of external factors on site selection. Mol Biol Cell *3*, 1025-1035.

Marco, E., Wedlich-Soldner, R., Li, R., Altschuler, S.J., and Wu, L.F. (2007). Endocytosis optimizes the dynamic localization of membrane proteins that regulate cortical polarity. Cell *129*, 411-422.

Masuda, T., Tanaka, K., Nonaka, H., Yamochi, W., Maeda, A., and Takai, Y. (1994). Molecular cloning and characterization of yeast rho GDP dissociation inhibitor. J Biol Chem *269*, 19713-19718.

Meinhardt, H. (1999). Orientation of chemotactic cells and growth cones: models and mechanisms. J Cell Sci *112 (Pt 17)*, 2867-2874.

Meinhardt, H., and Gierer, A. (1974). Applications of a theory of biological pattern formation based on lateral inhibition. J Cell Sci *15*, 321-346.

Moseley, J.B., and Goode, B.L. (2006). The yeast actin cytoskeleton: From cellular function to biochemical mechanism. Microbiol Mol Biol R *70*, 605-+.

Murray, J.D. (2003). Mathematical Biology II: Spatial Models and Biomedical Applications. (Springer).

Neiman, A.M., and Herskowitz, I. (1994). Reconstitution of a yeast protein kinase cascade in vitro: activation of the yeast MEK homologue STE7 by STE11. Proc Natl Acad Sci U S A *91*, 3398-3402.

Nern, A., and Arkowitz, R.A. (1999). A Cdc24p-Far1p-Gbetagamma protein complex required for yeast orientation during mating. J Cell Biol *144*, 1187-1202.

Novak, B., and Tyson, J.J. (2008). Design principles of biochemical oscillators. Nat Rev Mol Cell Biol *9*, 981-991.

Otsuji, M., Ishihara, S., Co, C., Kaibuchi, K., Mochizuki, A., and Kuroda, S. (2007). A mass conserved reaction-diffusion system captures properties of cell polarity. PLoS Comput Biol *3*, e108.

Otsuji, M., Terashima, Y., Ishihara, S., Kuroda, S., and Matsushima, K. (2010). A conceptual molecular network for chemotactic behaviors characterized by feedback of molecules cycling between the membrane and the cytosol. Science signaling *3*, ra89.

Ozbudak, E.M., Becskei, A., and van Oudenaarden, A. (2005). A system of counteracting feedback loops regulates Cdc42p activity during spontaneous cell polarization. Developmental cell *9*, 565-571.

Paliwal, S., Iglesias, P.A., Campbell, K., Hilioti, Z., Groisman, A., and Levchenko, A. (2007). MAPK-mediated bimodal gene expression and adaptive gradient sensing in yeast. Nature *446*, 46-51.

Park, H.O., and Bi, E. (2007). Central roles of small GTPases in the development of cell polarity in yeast and beyond. Microbiol Mol Biol Rev *71*, 48-96.

Park, H.O., Bi, E., Pringle, J.R., and Herskowitz, I. (1997). Two active states of the Ras-related Bud1/Rsr1 protein bind to different effectors to determine yeast cell polarity. Proc Natl Acad Sci U S A *94*, 4463-4468.

Park, H.O., Chant, J., and Herskowitz, I. (1993). BUD2 encodes a GTPase-activating protein for Bud1/Rsr1 necessary for proper bud-site selection in yeast. Nature *365*, 269-274.

Pruyne, D., and Bretscher, A. (2000a). Polarization of cell growth in yeast. I. Establishment and maintenance of polarity states. J Cell Sci *113 (Pt 3)*, 365-375.

Pruyne, D., and Bretscher, A. (2000b). Polarization of cell growth in yeast. J Cell Sci *113 (Pt 4)*, 571-585.

Pryciak, P.M., and Huntress, F.A. (1998). Membrane recruitment of the kinase cascade scaffold protein Ste5 by the Gbetagamma complex underlies activation of the yeast pheromone response pathway. Genes Dev *12*, 2684-2697.

Riquelme, M., and Bartnicki-Garcia, S. (2004). Key differences between lateral and

apical branching in hyphae of Neurospora crassa. Fungal Genet Biol *41*, 842-851.

Roemer, T., Madden, K., Chang, J.T., and Snyder, M. (1996). Selection of axial growth sites in yeast requires Axl2p, a novel plasma membrane glycoprotein. Gene Dev *10*, 777-793.

Rovinsky, A., and Menzinger, M. (1992). Interaction of Turing and Hopf bifurcations in chemical systems. Phys Rev A *46*, 6315-6322.

Schmitz, H.P., Kaufmann, A., Kohli, M., Laissue, P.P., and Philippsen, P. (2006). From function to shape: a novel role of a formin in morphogenesis of the fungus Ashbya gossypii. Molecular biology of the cell *17*, 130-145.

Segal, M., and Bloom, K. (2001). Control of spindle polarity and orientation in Saccharomyces cerevisiae. Trends Cell Biol *11*, 160-166.

Segall, J.E. (1993). Polarization of yeast cells in spatial gradients of alpha mating factor. Proc Natl Acad Sci U S A *90*, 8332-8336.

Shimada, Y., Gulli, M.P., and Peter, M. (2000). Nuclear sequestration of the exchange factor Cdc24 by Far1 regulates cell polarity during yeast mating. Nat Cell Biol *2*, 117-124.

Sloat, B.F., Adams, A., and Pringle, J.R. (1981). Roles of the Cdc24 Gene-Product in Cellular Morphogenesis during the Saccharomyces-Cerevisiae Cell-Cycle. Journal of Cell Biology *89*, 395-405.

Sprague, G.F., Jr. (1991). Assay of yeast mating reaction. Methods Enzymol *194*, 77-93.

Takahashi, S., and Pryciak, P.M. (2008). Membrane localization of scaffold proteins promotes graded signaling in the yeast MAP kinase cascade. Curr Biol *18*, 1184-1191.

Takeda, K., Shao, D., Adler, M., Charest, P.G., Loomis, W.F., Levine, H., Groisman, A., Rappel, W.J., and Firtel, R.A. (2012). Incoherent feedforward control governs adaptation of activated ras in a eukaryotic chemotaxis pathway. Science signaling *5*, ra2.

Tong, Z., Gao, X.D., Howell, A.S., Bose, I., Lew, D.J., and Bi, E. (2007). Adjacent positioning of cellular structures enabled by a Cdc42 GTPase-activating protein-mediated zone of inhibition. The Journal of cell biology *179*, 1375-1384.

Turing, A.M. (1952). The chemical basis of morphogenesis. Philosophical Transactions of the Royal Society of London. B *237*, 37-72.

Valdez-Taubas, J., and Pelham, H.R. (2003). Slow diffusion of proteins in the yeast plasma membrane allows polarity to be maintained by endocytic cycling. Curr Biol *13*, 1636-1640.

Van Haastert, P.J., and Devreotes, P.N. (2004). Chemotaxis: signalling the way forward.

Nat Rev Mol Cell Biol *5*, 626-634.

Whiteway, M., Hougan, L., and Thomas, D.Y. (1988). Expression of MF alpha 1 in MATa cells supersensitive to alpha-factor leads to self-arrest. Mol Gen Genet *214*, 85-88.

Winters, M.J., and Pryciak, P.M. (2005). Interaction with the SH3 domain protein Bem1 regulates signaling by the Saccharomyces cerevisiae p21-activated kinase Ste20. Mol Cell Biol *25*, 2177-2190.

Xiong, Y.A., Huang, C.H., Iglesias, P.A., and Devreotes, P.N. (2010). Cells navigate with a local-excitation, global-inhibition-biased excitable network. Proceedings of the National Academy of Sciences of the United States of America *107*, 17079-17086.

Yamamoto, T., Mochida, J., Kadota, J., Takeda, M., Bi, E., and Tanaka, K. (2010). Initial polarized bud growth by endocytic recycling in the absence of actin cable-dependent vesicle transport in yeast. Mol Biol Cell *21*, 1237-1252.

Yan, A., Xu, G., and Yang, Z.B. (2009). Calcium participates in feedback regulation of the oscillating ROP1 Rho GTPase in pollen tubes. Proceedings of the National Academy of Sciences of the United States of America *106*, 22002-22007.

Yu, R.C., Pesce, C.G., Colman-Lerner, A., Lok, L., Pincus, D., Serra, E., Holl, M., Benjamin, K., Gordon, A., and Brent, R. (2008). Negative feedback that improves information transmission in yeast signalling. Nature *456*, 755-761.

Zheng, Y., Cerione, R., and Bender, A. (1994). Control of the Yeast Bud-Site Assembly Gtpase Cdc42 - Catalysis of Guanine-Nucleotide Exchange by Cdc24 and Stimulation of Gtpase Activity by Bem3. Journal of Biological Chemistry *269*, 2369-2372.

Ziman, M., and Johnson, D.I. (1994). Genetic evidence for a functional interaction between *Saccharomyces cerevisiae CDC24* and *CDC42*. Yeast (Chichester, England) *10*, 463-474.